Biomolecular Imaging Mass spectrometry

Mapping molecular distributions in cells and tissue sections

Biomolecular Imaging Mass spectrometry

Mapping molecular distributions in cells and tissue sections

In kaart brengen van biomoleculaire verdelingen in cellen en weefsel secties.

(met een samenvatting in het Nederlands)

Proefschrift

ter verkrijging van de graad van doctor aan de Universiteit Utrecht
op gezag van de rector magnificus, prof. dr. W. H. Gispen, ingevolge het besluit
van het college voor promoties in het openbaar te verdedigen
op donderdag 15 maart 2007 des middags te 2.30 uur

door

Adrianus Frederik Maarten Altelaar
geboren op 21 maart 1976, te Alkmaar

Promotor: Prof. dr. R.M.A. Heeren

Co-promotor: Dr. S.R. Piersma (VUMC)

Contents

Introduction

Imaging mass spectrometry (IMS) allows the investigation of both identity and localization of the molecular content directly from tissue sections, single cells and many other surfaces. In order to retrieve the molecular ion signals of especially the larger molecules (>1000 Da) present in the sample, specific sample preparation steps are required directed at optimal signal intensity and minimal redistribution or modification of sample analytes. To further develop the application of IMS, different approaches to IMS will be described in this thesis and the specific sample preparation requirements will be discussed.

1.1 General Introduction

The genetic difference between humans and its closest relative the chimpanzee is expected to be 1-2% in nucleotide sequence.[1,2] Still, this difference results in specific human characteristics as well as specific diseases like Alzheimer's disease, which is essentially unknown in non-human species.[1] On the other hand, the comparison of the DNA sequence of the human chromosome 21 with its homologue in the chimpanzee (chromosome 22) showed amino acid differences in 83% of the encoded proteins. In 20% of the cases the changes were severe enough to affect the structure of the formed proteins.[1,2] Sequencing the human genome[3,4] (the total chromosomal (hereditary) content) was believed to lead to a further understanding of human biology and disease and provide new avenues for drug discovery. However, as it turned out, merely having complete sequences of genomes is not sufficient to elucidate biological function. It are the products of the genome, the proteins, which are involved in almost all biological processes and are considered the functionally most important biological molecules.[5,6] The total of proteins the genome produces, through biological transcription and translation, is called the proteome.[7]

Making the step from the analysis of the genome to the analysis of the proteome is not just a matter of numerical complexity. Genetic information cannot predict a protein's localization, posttranslational modification, expression level or association with proteins or other molecules.[8-10] Furthermore, the number of protein coding genes is far less than the number of actual proteins, resulting from alternative splicing and posttranslational modifications.[6,11-13] A significant further level of complexity is introduced by the precisely controlled temporal and spatial organization of these proteins.[14] A variety of approaches have been developed by which proteins may be directly analyzed on a proteome-wide scale. However, these methods do not address the important question of what location in the cell proteins are directed to and where they are active. To understand cellular function, all the molecules playing an active role need to be known at each point in time and location in the cell.[15] Protein localization is a strong indicator of gene function and the subcellular localization of a protein can often reveal its mechanism of action and interaction partners.[16]

Furthermore, several diseases are associated with altered localization of proteins.[17-19] Thus, protein localization is linked to cellular function, and introduces an analytical challenge for proteomics. Today fluorescence microscopy is mostly used for cellular localization analysis. The use of multiple fluorescent labels makes it possible to study the spatial behavior of several selected molecules in parallel in one experiment with high spatial resolution ($\sim$1 μm).[20-22] Huh et al.[23] have shown that a proteome-wide localization study using green fluorescent protein (GFP) fusion proteins in yeast is possible. However, similar studies in mammalian systems face numerous challenges as fusion proteins are usually overexpressed, and tagging itself is difficult and can lead to artifacts.[15] Furthermore, the limited number of molecules that can be examined in one experiment, its inability of detecting unknown molecules and the difficulty in detecting posttranslational modifications further limits the technique.[18] Chemical specificity is crucial in biological studies since the function of many biomolecules involves significant processing and posttranslational modifications. Chemical imaging mass spectrometry, which provides both the chemical information (molecular mass) and the spatial organization of surface components, is revolutionizing the field of biological surface analysis.[9,24,25] The attraction of imaging mass spectrometry is the ability to map the distributions of multiple (unknown) analytes in parallel, without using a label, from native samples (such as tissue sections).[26]

1.2 The Brain

The (human) brain is often stated to be the most extraordinary and complex system in the universe. The brain allows us to think, move, feel, see, hear, taste, and smell. It controls our body, receives information, analyzes information, and stores information (memories). Last but not least the brain gives rise to intelligence, creativity, emotion and consciousness. The human

produce electrical signals (actions potentials) resulting in release of chemical messengers at their synapses into the synaptic space. The chemical messengers are a relatively broad group of molecules, ranging from small neurotransmitters (like acetylcholine and serotonin), steroids, retinoids, fatty acid derivatives, nucleotides, single amino acids and dissolved gasses (e.g. nitric oxide) to (neuro)peptides and small proteins. The chemical messengers are normally present at very low concentrations (typically $\leq 10^{-8}$ M) in the plasma or in the small regions between cells or tissue (interstitial tissue). These low concentrations of messengers are specifically bound by transmembrane protein receptors with very high affinity, present on the cell surface of the target tissue. Binding of the (first) messenger activates the receptor, which generates a cascade of intracellular signals (secondary messengers) that alter target proteins downstream the intracellular signaling pathway and change the behavior of the cell. Steroid hormones are very hydrophobic and diffuse through the cell membrane to bind to intracellular receptors directly.

A second type of specialized signaling cells are endocrine cells. These cells control the behavior of an organism as a whole by secreting relatively large amounts of signal molecules into the blood stream. The bloodstream than carries these signal molecules (hormones) to the target cells distributed throughout the organism.

In this thesis both neurological and neuroendocrine signaling systems are subject of research. The central nervous system (CNS) of the fresh water snail *Lymnaea stagnalis* and mammalian nervous and neuroendocrine systems using a rat model system are studied. Invertebrate brains are very different from mammalian brains but still some of the basic demands are the same. Invertebrate species are particularly advantageous to study neurological pathways in relation to behavioral changes because of the simplicity of their nervous system and behaviors.[29] A possible drawback of using invertebrates is the lack of sequence information of their genomes. However, in the case of the pond snail *Lymnaea stagnalis*, a wealth of information is accessible about neuropeptide processing and distributions in nervous tissue.[30-38] Given the availability of both spatial as well as molecular information for *Lymnaea* neuropeptides, this mollusc represents an excellent model tissue for the development of high-resolution peptide imaging MS methodology. In the

mammalian nervous tissue the interest is primarily in the hypothalamic are of the brain. The hypothalamus is a region of the brain that controls an immense number of bodily functions. It is located in the middle of the base of the brain under the thalamus and links the nervous system to the endocrine system via the pituitary gland (Figure 1), which is a small organ at the base of the brain. The pituitary is part of the endocrine signaling system and secretes hormones into the circulatory system. The action of the pituitary is regulated by signals coming from the hypothalamus.

The hypothalamus encapsulates the ventral portion of the third ventricle (Figure 1). This area of the brain is unique in the sense that the so-called blood brain barrier (BBB) is not present.[39] The central action of peptide hormones on the brain is normally hindered because of limited access due to this BBB. However, some specific areas, called the circumventricular organs are unique areas of the brain that are outside the BBB. These barrier-deficient areas are recognized as important sites for communicating with the cerebrospinal fluid and stimulation of neuronal pathways within the brain.[39,40] The hypothalamus contains a number of different nuclei, among which the suprachiasmatic (the clock of the brain), sexually dimorphic, supraoptic, paraventricular and arcuate nucleus. These various nuclei are involved in a wide range of functions in the developing, adult and aging organism. They are responsible for a large number of symptoms in neuroendocrine, neurological and psychiatric diseases, of which only a part has been revealed so far. The hypothalamus control's body temperature, hunger, thirst, heartbeat, blood pressure and circadian cycles and is responsible, in a large part, for homeostasis (internal stability). Through specific neurons, which are linked to the limbic system, which is primarily involved in the control of emotions and sexual activity, the hypothalamus plays an important role in behavioral symptoms like fight or fleeing, feeding and reproductive behavior. Alterations in the hypothalamic structures and functions have been associated with diseases like anorexia nervosa, bulimia, depression, Cushing's disease, diabetes and obesity as well as in disturbance in sleep and temperature regulation. Several neurodegenerative diseases affect the hypothalamus, causing some of the specific symptoms of those diseases, e.g. in Alzheimer's, Parkinson's and Huntington's disease and multiple scleroses.[40-42]
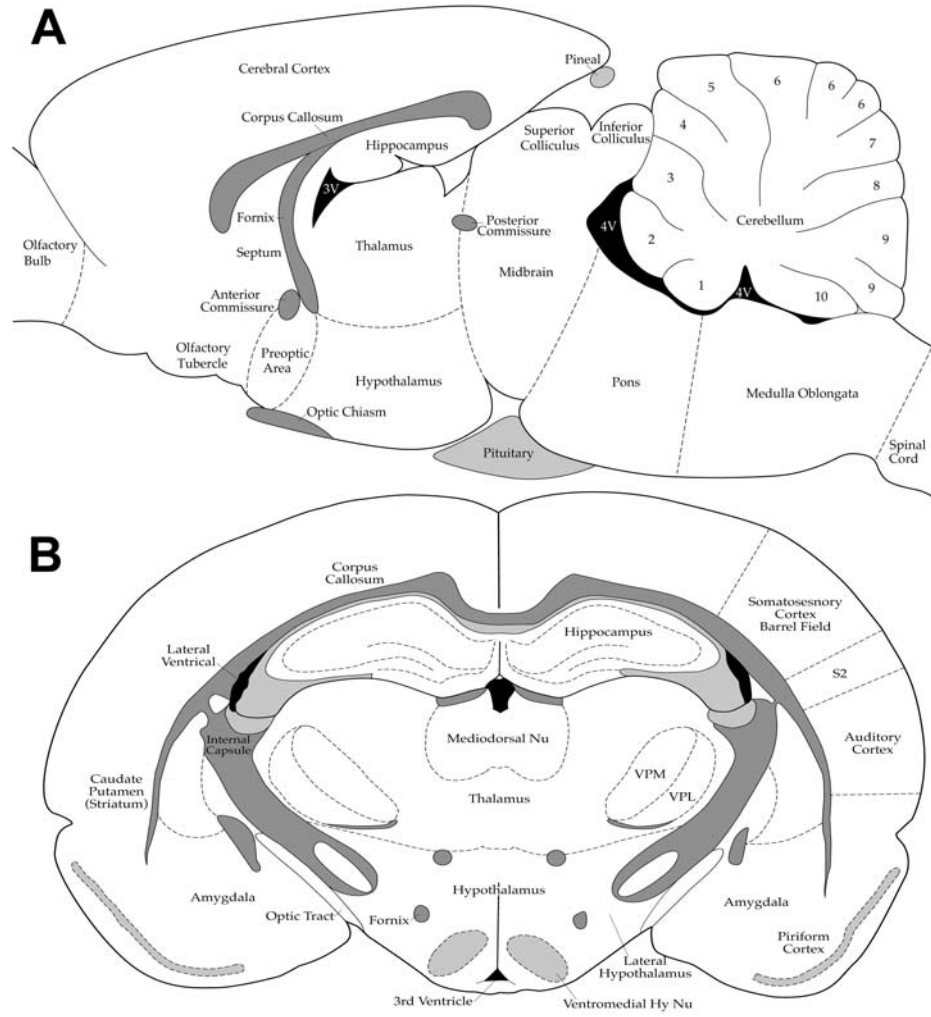
Figure 1. A) Sagittal diagram and B) coronal diagram of a rat brain. The sagittal diagram shows a section of the brain through the front, mid and hindbrain. The coronal diagram shows a frontal image at the thalamus, hypothalamus region in the midbrain showing the different nuclei present. Images were taken from the rat brain encyclopedia.[43]

Our specific interest in the hypothalamus stems from the neurological pathways involved in feeding behavior. Malfunctioning of these pathways is suggested to have a direct relation with obesity, anorexia nervosa and bulimia. It has been a widely held opinion that obesity arises from a lack of self-control, while in fact obesity is a complex disorder of appetite regulation and energy metabolism controlled by specific biological factors. Genes that predispose to obesity in humans and animals have already been identified and indicate the importance of genetic factors in the development of the disease. The incidence of obesity is rising and there are now as many obese people in the world as there are people suffering from hunger. Obesity has replaced under-nutrition and infectious disease as the most significant contributor to ill health.[44,45] It is hoped that understanding the molecular mechanisms that regulate appetite could ultimately lead to the development of novel therapeutic agents, which suppress food intake. In this context, peptides derived from the pro-opiomelanocortin (POMC) precursor protein are particularly interesting since they play a key role in the central control of feeding behavior.[45-47]

1.3 Pro-opiomelanocortin

Neuropeptides form the largest and most complex group of signaling molecules. They distinguish themselves from inactive products of the metabolism or processing of proteins (i.e. peptides) because they act as genuine first messengers. Neuropeptides pass on their message by interacting with G protein coupled receptors (the largest family of signal transduction molecules known).[48,49] In endocrine and neuronal cells neuropeptides of less than ~50 amino acids are produced from larger, inactive precursors. Many of these precursor proteins have complex structures consisting of multiple repeating units of identical or unrelated neuropeptides flanked by pairs of basic amino acids or, less frequently, single basic residues. Proteolytic cleavage at specific basic amino acid sites results in excision of the neuropeptide, which may than undergo additional biochemical modifications such as acetylation, amidation, sulfation, etc. to generate a biological active hormone.[50,51]
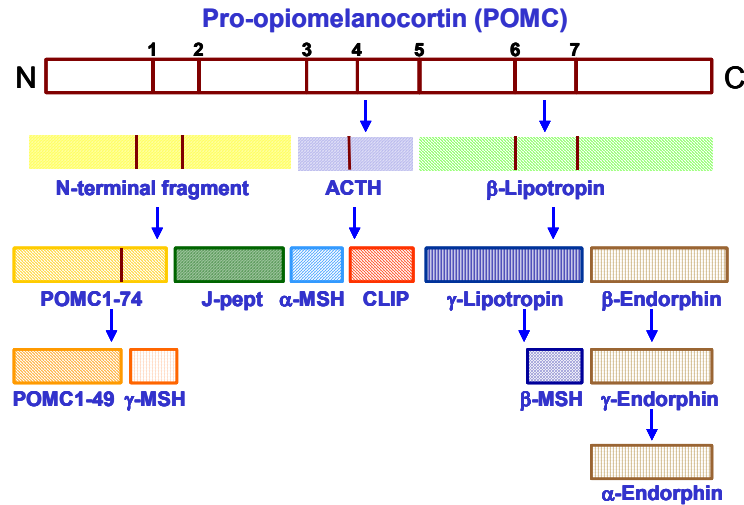
Figure 2. Schematic overview of the processing of the POMC precursor protein

The primary protein product of the POMC gene is a ~32 kDa precursor that can undergo differential processing, dependent upon the location of synthesis and the stimulus leading to their production (Figure 2). The processing of POMC involves glycosylations, acetylations, and extensive proteolytic cleavage at basic sites in the protein sequences. The proteases that recognize these cleavage sites are tissue-specific. The POMC precursor is cleaved by the prohormone convertase (PC) 1 to generate ACTH, β-lipotrophin (β-LPH) and the N-terminal fragment. The N-terminal fragment is further cleaved by PC1 to generate POMC1-74 and the joining peptide (JP). PC2 cleaves ACTH to generate ACTH1–17 and corticotrophin-like intermediate peptide (CLIP). PC2 also cleaves β-LPH to generate γ-LPH and β-endorphin. In humans, γ-LPH is cleaved by PC2 to generate β-MSH. Rats, however, do not have the paired lysine cleavage site required for the formation of β-MSH. POMC1-74 is cleaved to generate γ-MSH. In humans, PC2 is not expressed in the pituitary gland. Therefore, in contrast to the hypothalamus, the main human pituitary-derived products of POMC processing are POMC-1-74, ACTH and β-LPH. In addition to the prohormone convertases and their endogenous inhibitors, other enzymes play a key role in

generating mature POMC-derived peptides. For instance, the generation of α-MSH from POMC in the hypothalamus requires a complex pathway of posttranslational modifications involving numerous enzymes. The generation of mature α-MSH from ACTH is catalysed by carboxypeptidase E (CPE), peptidyl α-amidating mono-oxygenase (PAM) and n-acetyltransferase. First, carboxy-terminal basic amino acids are trimmed from ACTH by CPE. The peptide is subsequently amidated by PAM to generate desacetyl α-MSH. This is converted to mature α-MSH by n-acetyltransferase.

1.4 Neuropeptides involved in food regulation

The regulation of food intake and body weight is a very complicated interplay between a 'bewildering' number of endogenous molecules. The complexity of the food regulation process is caused by the fact that through evolution different behaviors (like hunting for food and decision making) and thus different brain areas are involved.[52] The basic principle of food regulation is that there are two competing pathways, which stimulate either an increase or decrease in food intake. These pathways are influenced by inhibitory signals generated in proportion to fat stores in the body and signals generated during eating (called satiety factors). To date two protein hormones are known to regulate these pathways namely leptin and insulin. These hormones circulate in the blood proportional to body fat content and energy balance. Administration of either of the two peptide-hormones leads to reduced food intake while a deficiency of either hormone does the opposite. The main players in these pathways are neuropeptide Y (NPY) the POMC precursor protein and the Agouti related protein (AGRP) (Figure 3), all expressed in the arcuate nucleus. NPY stimulates food intake and decreases energy consumption. Secretion of the NPY peptide in the hypothalamus is increased during body fat depletion and/or reduction of leptin/insulin signaling to the brain. Conversely, the POMC product α-MSH is related to suppression of food intake. POMC products exert their effects by binding to melanocortin receptors, from which MC3 and MC4 have been shown to suppress food intake. Finally, AGRP is an antagonist of the melanocortin

17
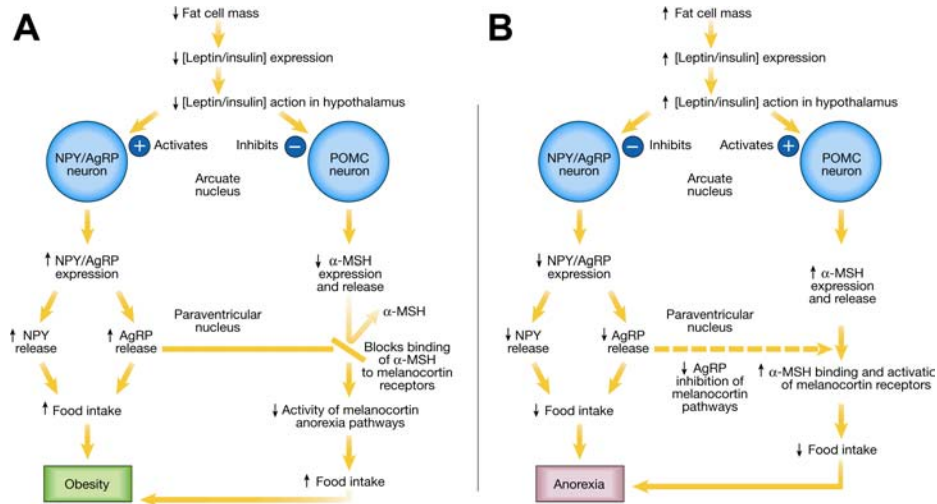
Figure 3. Role of the arcuate nucleus neurons in food intake regulation. A) Increase in food intake by decrease in body fat and/or leptin/insulin expression. B) Decrease in food intake by increase in body fat and/or leptin/insulin expression. Taken from reference 53.

receptors resulting in suppression of the POMC effects and thus leading to increased food intake.[47,53-55] Figure 3 shows the hypothalamic neurological pathways responsible for the regulation of food intake. It also shows the effect of increased expression of components in one of the two pathways. Figure 3A shows that when the total amount of body fat and/or the leptin/insulin expression in the hypothalamus is low the NPY/AGRP pathway is activated resulting in an increase in food intake. When this situation exists for a prolonged period it might result in obesity. Conversely, in Figure 3B, increased body fat and/or expression of leptin/insulin results in the activation of the POMC pathway and suppression of food intake, which in time can lead to anorexia.[53]

To complicate the regulation of food intake even more, processing of the POMC precursor protein also results in the appetite stimulating peptide β-endorphin.[52] So, full processing of the POMC precursor will result in storage of β-endorphin and α-MSH in the same synaptic vesicles and the release of α-MSH will always be accompanied by the release of β-endorphin at the same anatomical site. In

order to regulate the activity of these counteracting peptides, posttranslational acetylation plays a crucial role.[56] Inhibition of food intake in food-deprived rats has been shown after administration of the N-acetylated form of α-MSH, while the desacetylated form showed no effect. Conversely, N-acetylation of β-endorphin eliminated all effects on food intake following injection into the third ventricle, which were shown with injection of non-acetylated β-endorphin.[56] The N-acetylation of products formed by the processing of POMC markedly altered their biological properties, which is crucial in the regulation of food intake.

1.5 Imaging Mass Spectrometry

As mentioned before chemical messengers and especially neuropeptides (which are often more potent than other neurotransmitters) are synthesized and active at very low concentrations (μM, pM). These low concentrations and the chemical diversity of the transmitters make detection a challenge. The processing of specific neuropeptides from a common precursor can differ between cells and at varying points in a cell's development. Furthermore, posttranslational modifications will alter the structure and often the activity of a neuropeptide. To be able to detect all these different classes of molecules at these low concentrations, mass spectrometry has become the method of choice. In standard proteomic studies a large population of cells is harvested, a homogeneous mixture produced, and the mixture analyzed for the molecules of interest. Although this method is effective for characterizing compounds found in large populations of cells, it becomes problematic when only a few cells in an otherwise homogeneous sample demonstrate drastic differences, which is often the case in medical disorders.[57] Single cell and direct tissue analysis using imaging mass spectrometry (IMS) are possible ways to overcome these limitations. IMS has recently been recognized as a proteomic tool for in situ spatial analysis of (diseased) tissue.[9,24] IMS enables the investigation of the effect of disease, drug treatment, environment etc. in tissue or cells without removing the molecules of interest from their natural habitat. IMS of large intact biomolecular species became feasible after the invention of the soft ionization

technique matrix assisted laser desorption/ionization (MALDI).[58] In 1993/1994 the first reports appeared on direct MALDI analysis of neuropeptides from single *Lymnaea stagnalis* neuronal cells,[34,35] followed by neurons from the marine mollusc *Aplysia californicu*.[59] The first peptide analysis directly from tissue was performed by Caprioli et al.[60] in 1997. Since then IMS has proven to be a powerful extension of existing proteomic techniques. Sweedler and co-workers continued the work on profiling of peptides in single cells and organelles.[31,61,62] In tissue, the localization of amyloid β peptides in relation to Alzheimer's disease,[63,64] the decrease of a neuronal calmodulin-binding protein (PEP-19) in relation to Parkinson's disease[65] and the accumulation of transthyretin Ser28-Gln146 in the cortex of affected kidneys after drug administration[66] has been shown using MALDI-IMS. Distinct different protein profiles have been obtained between tumor and non-tumor tissue within one tissue section.[67] Another very interesting application in IMS is the tracking of administered drugs. Using IMS it is possible to follow not only the parent molecule but also possible metabolites formed after administration.[63,68]

1.6 Scope of this thesis

This thesis describes different methods developed to study biological systems, as described above, using imaging mass spectrometry. The chapters describe different approaches to studying molecular distributions in different biological systems. Success in the IMS experiments described in this thesis turned out to be dependent on the interplay between instrument development and fine tuning, sample preparation and data handling.

In **chapter 2** the techniques used will be explained together with the IMS instrumentation and different approaches to sample preparation. **Chapter 3** is a protocol; providing guidelines towards a successful IMS experiment. **Chapter 4** describes results on gold-enhanced biomolecular imaging. The use of a thin layer of gold in both SIMS and matrix-assisted laser desorption/ionization (MALDI) MS results in increased signal intensity in the analysis of cells and tissue. **Chapter 5** shows the capabilities of matrix-enhanced secondary ion

mass spectrometry (SIMS) in analysis of neuropeptides in direct tissue imaging of *Lymnaea stagnalis* nervous tissue. Furthermore, it illustrates the difficulties encountered in direct tissue imaging with respect to the tissue microenvironment and its effect on the MS desorption/ionization process. **Chapter 6** describes the MALDI-IMS analysis of pituitary gland tissue sections from three different organisms.

Imaging Mass Spectrometry;
Ionization and Instrumentation

The success in imaging mass spectrometry experiments depends on several factors from sample collection and preparation to desorption/ionization and detection. After these experimental factors the data handling is of crucial importance to retrieve the useful data from the large IMS datasets. In this chapter the different ionization techniques used in IMS (i.e. SIMS and MALDI) are discussed, explaining the theory behind the techniques and showing several IMS applications of both techniques. Furthermore the instrumentation used in the IMS experiments is described as well as different sample preparation techniques aimed at the localization of biomolecular species (ranging from lipids till peptides) directly in tissue sections and on cellular surfaces.

2.1 Secondary Ion Mass Spectrometry

In secondary ion mass spectrometry (SIMS) the sample surface is bombarded with a high-energy primary ion beam, either single- or polyatomic, between 5 and 25 kiloelectronvolts (keV). Typical primary ions used in SIMS include Ga^+, Cs^+, In^+, C_{60}^+ and Au_n with Ga^+ being able to provide the smallest probe size (less than 10 nm). The rastering of the primary ion beam over the sample surface results in desorption (or sputtering) of both neutral and charged species, consisting of atoms, clusters of atoms and molecular fragments. The charged species (secondary ions) are extracted into the mass spectrometer for mass analysis.

The sputtering process in SIMS is best described by a collision cascade. When a high-energy primary ion collides on a solid surface, it starts a 'billiard-ball-type' collisional process called a cascade. The projectile dissipates its energy to the atoms in the solid by collisions and if these are energetic enough they collide with other atoms etc. Eventually some atoms in the cascade acquire enough outward-directed momentum, leading to desorption of these atoms. Bombardment of complex organic surface layers with high-energy ions will induce damage over a certain depth in the sample, caused by the slowing down of the primary ion and the recoil atoms in the surrounding matter (the size of the collision cascade). The extent of the damage depends on the nature, mass and energy of the primary ions. Scanning tunneling microscope measurements on a silica surface showed for example that bombarded with a single 3 keV Ar^+ ion results in a damaged area in the order of 25 nm^2.[69-71]

The result of the induced damage is that the molecular structure of the constituents in this area (the damage cross section) does no longer correspond to that of before the impact. The energy lost by a particle when it is brought to a standstill in the sample is 5-25 keV, and even a minor fraction of this energy is more than enough to break any chemical bond. To prevent analysis of damaged areas and retain the original molecular information, it is essential that no primary ion strikes the damaged region a second time.[71] For this reason the total ion dose must be kept under a so called static limit, in which less than 1%

of the top surface atoms and molecules have interacted with the primary ion beam.

This static limit divides SIMS into two regimes, namely dynamic SIMS, for elemental analysis, and static SIMS, for organic or molecular analysis. The difference between the two regimes is the density of the primary ions reaching the sample surface. In dynamic SIMS a primary ion dose of approximately 10^{16} ions per cm^{-2} is used, which results in the sample surface being eroded in time and most molecular species being completely destroyed. In static SIMS an ion dose $<10^{13}$ ions per cm^{-2} is used with which only the top layer of the sample is damaged.[72-74] Consequently, the lower primary ion dose in static SIMS results in a higher ionization yield of intact, low molecular weight, species as well as their fragments. The main field of application for dynamic SIMS is material science (e.g. detection of pollutants in semiconductor fabrication) but the technique has also been used in the analysis of organic elements (Na, K, Ca, Cr, etc.) in cells,[75-78] chromosomes,[79] hair[80] and plant tissue.[81,82] Static SIMS has been used in a wide variety of molecular imaging studies such as a number of pharmaceutical compounds in tissue and tissue-like matrices,[73] ferruginol, a diterpene phenol, in *Cryptomeria japonica* heartwood,[83] vitamins in single cells[84] and tissue[85] and the phosphatidylcholine headgroup, sterols, fatty acids and lipids in freeze fractured single cells,[86] Langmuir-Blodgett films,[87] picoliter vials,[88] tissue[89,90] and cells.[91-93]

2.2 Enhancing molecular ion yield in SIMS

The sputtering process in SIMS using high-energy primary ions results in fragmentation of almost all of the labile components on the surface. Increasing sensitivity for these labile intact molecular ions has been a major research topic in organic SIMS for more than ten years. Several strategies have been developed to minimize the internal energy deposition during desorption and ionization in SIMS. One approach is the use of polyatomic primary ion sources like C_{60}^+, SF_6^-, Au_n and Bi_n^{m+}, resulting in an increase in secondary ion yield.[94,95] Here, a beam of energetic ions (up to several thousand electron volts) is

directed at the surface. This cluster ion is believed to dissociate at the moment of impact on the surface, which results in the redistribution of the initial kinetic energy over the atoms present in the cluster.[95,96] As can be seen from Figure 1, the collision cascade in the case of a single projectile is mostly directed downwards and most of the energy is deposited beneath the surface (first two monolayers), resulting in very little material being removed. In the case of a 15 keV C_{60}^+ polyatomic primary ion source the energy deposition on the surface changes from a single 15 keV impact to 60 individual 250 eV impacts, each creating its own collision cascade. In this way, the energy deposition is much softer, which results in the deposited energy staying closer to the surface and leading to more efficient desorption.[95,97] Furthermore, for large molecules, carbon atoms in more than one part of the molecule must be hit in order to initiate the collective motion of the entire molecule as it lifts off of the surface.[98] This phenomenon is more likely to happen when there are multiple collision cascades that can lead to collisions with different parts of the molecule. Since with the polyatomic primary ion sources several collision cascades are initiated simultaneously, there is a higher probability of producing two adjacent collision
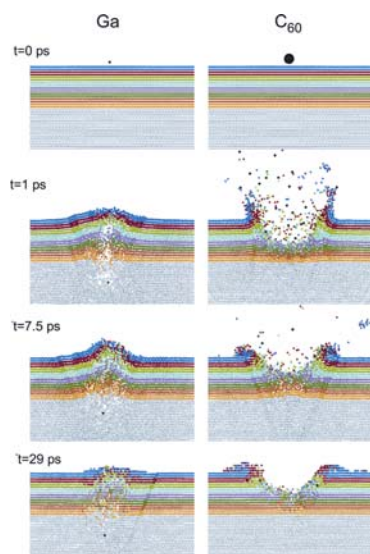
Figure 1. Cross-sectional view of the temporal evolution of a typical collision event leading to ejection of atoms due to 15 keV Ga^+ and C_{60}^+ bombardment of a silver metal surface at normal incidence. The atoms are colored by original layers in the substrate. The projectile atoms are black. (Taken from ref. 97)

cascades that can hit different carbon atoms in the same molecule. In addition, damage accumulation following continued bombardment is much less when using polyatomic primary ion sources as compared to mono-atomic ion sources, due to the efficient removal of the top layers, offering the possibility of measuring well beyond the static SIMS limit.[97,99,100] However, up till now no protein or peptide signals have been obtained directly from biological surfaces using cluster primary ion sources and the technique is biased to lipids, fatty acids and steroids. This phenomenon can be caused by several factors like difference in abundance, internal energy deposition or ionization conditions between peptides and proteins on the one hand and lipids and steroids on the other. The lipids observed in most types of SIMS analyzes are major constituents of the cellular membrane and thus are abundantly present in biological samples. Differences in energy deposition can be caused by the microenvironment of a tissue or cell in which the species are situated, which is very different for a lipid molecule (closely packed in a membrane) than for a peptide or protein. Last, the difference in ionization conditions is caused by the fact that several lipid species are present in the sample as charged species and thus do not need to undergo additional ionization mechanisms.

A different approach to enhance the ionization/desorption yield of intact molecular species in SIMS is by surface modifications. Techniques like fast atom bombardment (FAB) and MALDI are capable of producing ions at significant higher masses than SIMS. The presence of a matrix results in minimizing of the internal energy deposition and thus prevents extensive fragmentation. Furthermore, in the MALDI plume fragmentation is reduced by collisional cooling of the analyte with the matrix molecules.[101] Odom et al.[102] showed that MALDI sample preparation protocols could be used in SIMS, to enhance the desorption/ionization yield of large biomolecules (e.g. peptides, proteins and nucleotides). This technique is named matrix-enhanced (ME) SIMS. In ME-SIMS standard MALDI matrixes are used, with 2,5-dihydroxy-benzoic acid (DHB) giving signal intensity enhancement over the widest range of analytes.[102] Another strategy is metallization of the sample by sputter coating of ~1 nm of, in most cases, silver or gold. Gold is preferred over silver because of its single isotope compared to the almost 50:50 distribution of the two silver isotopes (^{107}Ag and ^{109}Ag), which complicate the mass spectrum. This technique, named

Metal-Assisted (MetA) SIMS, has been demonstrated to increase secondary ion yields in SIMS,[103-106] not only for the cationized species but also for the observed fragments and protonated species.[106,107] The exact mechanism leading to the enhanced sputter yields of organic species after metallization is still under debate. Molecular dynamics simulations have shown that gold enhances desorption/ionization by cooperative elevation of analyte molecules and metal atoms with similar momentum.[108] Since it is known from literature that deposition of a thin gold layer result in the formation of gold nanoislands,[105] one likely explanation for the increased secondary ion yield is migration of mobile analytes onto these gold nanoislands.[106,109] This would create an environment similar to that of a molecular layer adsorbed on a metal substrate where the increased stopping power of the metal increases secondary ion yields.

2.3 Matrix-assisted laser desorption/ionization

Increased signal intensity in laser desorption experiments by 'matrix assistance' was described for the first time by the group of Hillenkamp[110] in 1985. Here a mixture of the amino acids alanine (Ala) and tryptophan (Trp) was measured at a laser wavelength of 266 nm. It was observed that a tenth of the irradiance was needed to obtain the Ala signal in the presence of Trp at similar signal intensity as when measured alone. Here the Trp was used as absorbing matrix, assisting in the molecular ion formation of the nonabsorbent Ala. Only a few years later the potential of MALDI-MS was shown by the same group, who obtained spectra of proteins up to bovine albumin (67000 Da), using nicotinic acid as matrix.[58] Furthermore, in the same year Tanaka et al.[111] showed protein and polymer signals up to m/z 100000 using a metal powder as matrix. Nowadays, MALDI-MS is a well-established technique for the fast determination of the exact molecular mass of macromolecular species, like peptides, proteins, oligonucleotides and carbohydrates, from biological samples. In conventional MALDI-MS, the sample is first mixed in solution with a large excess of a suitable matrix, which is typically a low-molecular-mass organic molecule with absorbance at the desired laser wavelength, and introduced on a target into the

mass spectrometer. The sample-matrix mixture is irradiated typically with a nitrogen laser operating at 337 nm or a frequency tripled Nd:YAG laser at 355 nm.[101] The exact mechanism leading to the desorption/ionization process in MALDI is still under investigation after 20 years. Each pulse from the laser results in a collective upward motion of analyte and matrix molecules, the so-called MALDI plume. Recent molecular simulation studies have shown that at MALDI threshold laser fluence, the physics involved in this process does not only contribute individual desorbed molecules but extends to large molecular clusters being ejected, as depicted in Figure 2.[112] This collective ejection process is referred to as ablation.
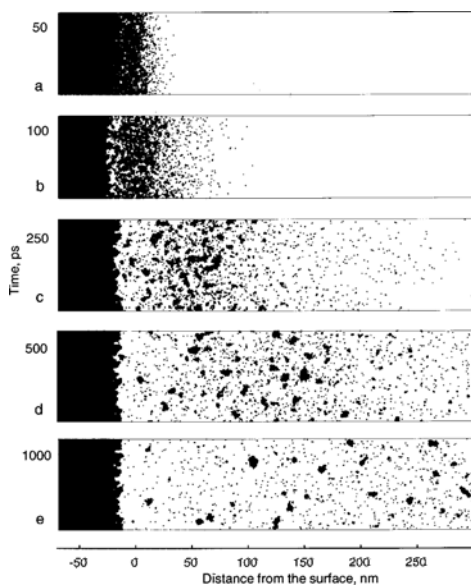
Figure 2. Time development of the MALDI plume in a 2D simulation. The total fluence is approximately twice the threshold fluence for ablation. Taken from reference 112

For the ionization of the MALDI analytes two main models have been postulated. One model assumes ionization of the analyte molecules to take place by secondary ion-molecule reactions in the MALDI plume,[101,113] while in the other model the typical MALDI analytes are already in a precharged state when

incorporated in the matrix crystals and the 'lucky survivors' make it to the detector.[114,115] In the latter case charged clusters are formed after laser ablation with a deficit or excess of ions and ionization is accomplished via charge separation and absorption of high-energy photons (photoionization). The final singly charged ions are formed by desolvation of matrix and/or residual solvent. The formed clusters after laser ablation are now also recognized in the first model, but still ionization is believed to take place by secondary reactions in the plume.[116]

Experimental settings affecting the MALDI process, besides the laser wavelength, are laser fluence and irradiated area. In fact these two parameters are interlinked since the laser threshold fluence for MALDI scales with the size of the laser beam used. An increase in laser fluence of one order of magnitude was needed to reach the MALDI threshold when going from a laser spotsize of ~200 μm to ~10 μm.[117] This phenomenon results in decreased sensitivity for high mass molecules when decreased laser spot sizes are used in MALDI due to increased fragmentation.[118,119]

In MALDI-MS, the matrix solution is prepared by choosing a solvent in which the matrix material is easily dissolved, such as 30-50% acetonitrile in 0.1% aqueous trifluoracetic acid. The analyte is typically dissolved in an aqueous solution. These two solutions can be applied onto the MALDI target consecutively or they are mixed first and the mixture is applied onto the target where it is allowed to dry. In both cases, the sample and the matrix must be dissolvable under the same conditions otherwise one of the components could precipitate. As the solvent slowly evaporates, matrix crystals are formed with the analyte, e.g. proteins or peptides, incorporated in these crystals. In the MALDI-MS analyses of protein and peptide samples, common matrix materials are cinnamic acid derivatives (e.g. sinapic acid (SA) and 4-hydroxy-α-cyanocinnamic acid (HCCA)) and 2,5-dihydroxybenzoic acid (DHB), which are shown in Figure 3.

The proper choice of the matrix is crucial in obtaining good MALDI-MS spectra. Incorporation of the analyte molecule into the formed matrix crystals is a prerequisite for successful MALDI analysis. The role of the matrix crystal is the isolation of individual analyte molecules (disentangling long chains and braking protein-protein interactions), exclusion of excess salt from the matrix crystals and mediation of the incident laser energy by absorption.[114] However, recent

Figure 3. Structures and names of commonly used MALDI matrixes.

2,5-Dihydroxybenzoicacid   4-Hydroxy-α-cyanocinnamic

Sinapic acid
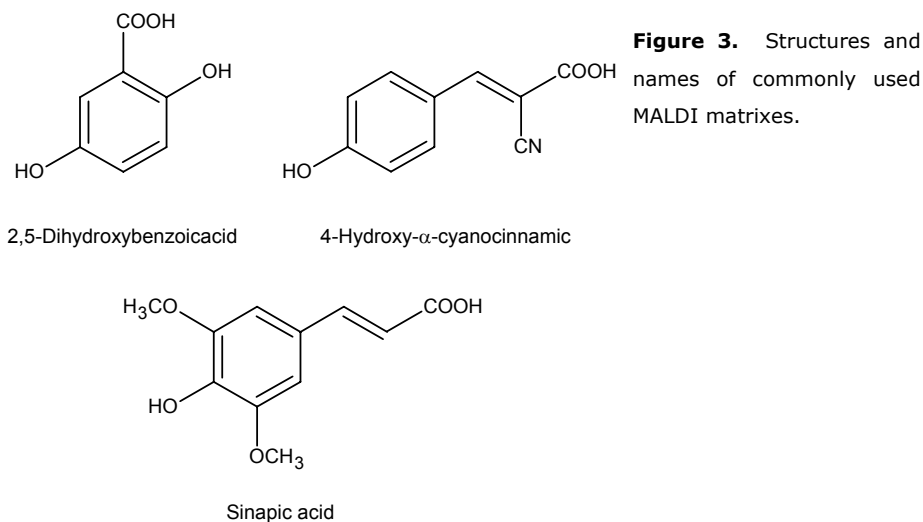
approaches in solvent free MALDI sample preparation have relit the discussion on the need for analyte incorporation.[120-122] In solvent free MALDI the contact between analyte and grounded matrix with the smallest remaining crystallinity but sufficient absorption at the chosen laser wavelength is sufficient to obtain protein signals.[122] However, the dry matrix applications have shown to give somewhat compromised spectra compared to the wet MALDI sample preparation and the desorption process was shown to be significantly harder.[121]

When using the right matrix and laser threshold conditions in MALDI, almost no prompt fragmentation during desorption of the analyte molecules occurs. The fragments observed in MALDI are mostly generated during extraction, ion transport and/or ToF analysis (by metastable decay) and collisions with background gas. However, choosing the right matrix conditions can minimize these formed MALDI fragments. For example, the matrix HCCA gives the highest sensitivity for MALDI peptide analysis combined with fast time-of-flight (ToF) detection (microseconds) but results in increased fragmentation when used in the slower trapping detection systems like ion trap instruments (milliseconds).[3] The reason for this is that HCCA is a 'hotter' matrix than DHB, which means that

the amount of energy passed on to the analyte molecules during desorption and ionization is higher. One explanation is simply the temperature at which the matrixes sublimate and hence desorb the analytes.[101] So if the analyte molecules have to be stable for milliseconds instead of microseconds the colder matrix DHB is preferred over HCCA.

The poor understanding of ion generation in MALDI is a big drawback and results in several unresolved issues when measuring multicomponent mixtures. In typical MALDI spectra most of the observed species are singly charged which makes these spectra easy to interpret. However, mixtures of multiple components, for example peptides, can experience preferential desorption and/or ionization.[3,123-125] Factors influencing the likelihood of ionization of specific peptides are charged side chains, presence of aromatic amino acids, peptide hydrophobicity, size and the ability to form a stable secondary structure.[125] Furthermore there is the so-called suppression effect, where dominant peptides in the desorption/ionization process suppress ionization of other peptides present in the mixture.[3,124,125] A well-known example of this phenomenon can be seen in MALDI analysis of tryptic peptides of any given protein. The sequence coverage of the peptides making up the backbone of the protein using MALDI is typically 40-60%. The rest of the peptides are not observed due to the different reasons explained above. Still for these types of studies the sequence coverage is high enough for protein identification. Problems occur when all species present in the mixture need to be detected, like in combinatorial chemistry or imaging MS, or when quantitation is an issue.

2.4 Instrumentation

All the IMS experiments described in this thesis are performed on two Physical Electronics TRIFT-II (triple ion focusing time-of-flight) mass spectrometers. All the SIMS experiments are performed on a TRIFT equipped with an ^{115}In$^+$ liquid metal ion gun and the MALDI experiments on an extensively modified version of the same instrument equipped with a MALDI ionization source, a phosphor screen/CCD camera optical detection combination and an Acqiris digitizer. The

SIMS, ME-SIMS and MetA-SIMS experiments were performed using a liquid metal ion gun (LMIG) ion column operated with an indium ($^{115}In^+$) primary ion source. The beam energy can be varied from 5-25 keV, providing an ion current ranging from 20 pA to 20 nA. The primary ion beam can be optimized for high mass resolution or high spatial resolution using an electrodynamic pulse buncher. For high mass resolution the primary ion bundles are compressed into 1 ps pulses while for high spatial resolution an unbunched pulse of 30 ns is used, which enables a tighter focus of the beam, down to 250 nm (at 25 KeV). Typical instrument settings in the described experiments were chosen in such a way that all the analyses were conducted in the static SIMS regime. At a primary ion energy of 15 keV the primary ion beam current is 450 pA, the primary pulse length 30 ns and the spot diameter 500 nm. For each chemical image, the primary beam is rastered over the sample area at a maximum repetition rate of 8 kHz (depending on the mass range used), analyzing a new area with every pulse. A dual micro channel plate (DMCP) detector records the arrival time of the secondary ions which are then correlated with the (x,y) position of the ion beam. The MALDI experiments described in this thesis are conducted with either a 337 nm, 3 ns pulse duration N_2 laser (VSL-337ND-S, Laser Science, Newton, USA) or a wedge, diode pumped solid-state Nd-YAG laser source, at 355 nm, 2 ns pulse duration (BrightSolutions, Italy). The light is coupled into a 200 μm diameter, 6 meter long optical fiber to homogenize the intensity distribution across the laser spot, to obtain an approximate top-hat distribution. The top-hat distribution is needed in the stigmatic imaging experiments to homogenously illuminate the surface and obtain true details from within the laserspot. The exit of the fiber is one-to-one imaged onto the sample, through a home-built laser-inlet system with a maneuverable (x-y-z) last focusing lens placed inside the vacuum at a distance of 35 mm from the sample.[126,127]

The TRIFT mass spectrometer is designed as a stigmatic ion microscope, which transports a magnified ion image from the sample to the detector (Figure 4A) while providing energy focusing for the flight time (Figure 4B).[128] Ions emitted from the surface are extracted and focused by an immersion lens, and then accelerated to a nominal kinetic energy of 3 keV into a field free drift region. The stigmatic imaging system consists of three 90º quasi-hemispherical electrostatic
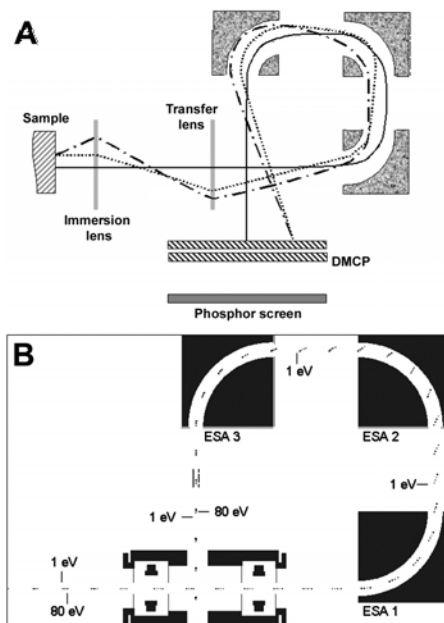
Figure 4. Schematic representation of the TRIFT ion microscope.

analyzers (ESAs), which form part of the ion optics. The ESAs correct for differences in the initial kinetic energies of the secondary ions resulting in time focusing of the ions, which provides higher mass resolution. Ions leaving the sample surface have different initial kinetic energy and angular distributions, caused by the sputtering/desorption and ionization process. The ESAs compensate for these differences by stronger deflection of ions of lower energy and weaker deflection for higher energy ions, resulting in longer flight paths for the faster ions (Figure 4B). A pulsing system controls a low energy electron gun to compensate possible charge build up during positive or negative secondary ion analysis of insulators. Mass spectra are recorded by measuring the time difference between pulsing of the ionization source and the arrival of ions on a fast micro channel plate detector at the end of the spectrometer by means of a multi stop time-to-digital converter (TDC) of 138 ps time resolution.

The TRIFT can operate in both the microprobe and the microscope mode. For this latter purpose it contains stigmatic ion optics. A magnified image of the analysis area is projected onto a DMCP via an immersion lens, one of two transfer lenses and the energy focusing electrostatic analyzer section. For the MALDI microscope mode experiments the ion detector consists of a DMCP, an Acqiris DP214 PCI-digitizer card, a phosphor screen and a CCD camera. An ion that leaves the sample at a particular location arrives at its conjugate image point on the DMCP, where the 8-bit PCI-digitizer card records the ion signal. As a result of the incident ion, the electron multiplying channel plates generates a packet of $\sim10^8$ electrons on the backside of the plates. The electron pulse is accelerated onto the phosphor screen, stimulating light emission that is detected by the CCD camera. Thus, the phosphor screen/CCD camera provides a real time stigmatic image of the analysis area. Triggers for the CCD camera and PCI-digitizer card are provided by a photodiode, which picks up the scattered light from the laser source. The duration of analysis part of one cycle of a microscope mode experiment is dependent on the selected mass range and takes maximally 900 µs. Within this time a series of ion images, separated in time arrives at the phosphor screen. The speed of operation of the CCD camera (exposure time ≥ 1 ms) currently limits microscope mode imaging to one image per laser shot, the subsequent images arriving at the detector cannot be recorded separately. So-called post-ESA blanking plates allow the selection of a particular mass window for mass resolved ion imaging. When a voltage is applied to these plates secondary ions are deflected from their flight paths and will not reach the detector. A selected mass window is gated by switching the potential of the blanking plates off and back on at definite times after the firing of the laser pulse. This delay is generated using a Stanford delay generator box.[126-130]

2.5 Sample preparation

Sample preparation is of crucial importance in IMS. The sample conditions have to be matched with the biological questions under study, resulting in optimal sensitivity for the molecules of interest with minimal intervention on their

structure or spatial orientation. Biological systems can be studied either as single cells or in tissue sections both requiring specific sample preparation steps. The specific sample preparation requirements before IMS analysis are discussed in chapter 3 and in the chapters describing the application. Here a general outline will be given.

Tissues are complicated three-dimensional structures, composed of a large number of different interacting cell populations. When looking at the differences between healthy and diseased or (drug) treated and untreated tissues, discrimination between cell populations will be crucial. However, the cells of interest may lie within or very close to unaffected areas. To be able to distinguish between different cell populations within a tissue section, a high spatial resolution imaging technique is required. Since the obtainable spatial resolution in any IMS experiment is a convolution between the instrumental spatial resolution and the sample preparation steps, stringent conditions on the sample preparation are required. Culturing cell populations has been used to overcome this problem. However, working with single cells is very delicate, putting even more limitations on the possible sample preparation steps. Moreover, the molecular content of a single cell is very low and since cultured cells are separated from their native tissue elements that regulate gene expression, extracellular heterogeneity, cell-cell communication, etc., these cells might not accurately represent the original cell population.

The first step in an IMS experiment is preserving the condition of the macromolecules to be analyzed. Flash freezing, cryosectioning, and optimal processing of the transferred tissue are required. Conventional fixation, embedding and sectioning are often not compatible with IMS experiments. Embedding is possible in some cases (small organs like *Lymnaea* CNS or pituitary glands (~3-5 mm)) when a non-polymeric embedding material, like gelatin, is used. Polymeric embedding materials like Tissue-Tek smear over the tissue surface during sectioning and result in dominant polymer signals in the IMS analysis. For non-imbedded organs the mounting on the holder for sectioning is done using a small amount of Tissue-Tek as glue but contamination of the region of interest must be prevented. Fixation of the tissue makes it virtually impossible to desorb the molecular content in the IMS analysis.

In SIMS analysis the preparation of tissue samples is relatively straightforward. Since SIMS can analyze almost any kind of solid surface, the tissue sections are brought to room temperature and analyzed. Analysis of cell cultures is more complicated since the cells are grown in growth medium, buffer and serum. The large amount of salt, amino acids and serum molecules will dominate the mass spectrum. For this reason the cell samples have to be washed prior to analysis. Washing cell cultures with demineralized water results in hypotonic shock and disruption of the cell surface within one minute. To prevent disruption of the cell a first wash step is preformed in isotonic sugar solution. Then in a second step the access of sugar is washed away by a quick rinse in demineralized water follow by immediate drying under vacuum.

An extra level of complexity is added when the described MetA- and ME-SIMS analysis are performed. Especially in ME-SIMS controlling the size of the matrix crystals and prevention of redistribution of the analytes is a key issue. In order to meet these criteria we developed an electrospray deposition (ESD) method, described in more detail in chapter 5. Using ESD results in the deposition of micron-sized matrix crystals in top of the sample.

In MALDI the different approaches to sample preparation are much more elaborate. In order to have good crystallization of the matrix on top of the tissue section a washing step is required to wash away the excess salt. This washing is typically done using a 70% ethanol solution, although chloroform, hexane and xylene have also been used.[131] The choice of matrix is dependent on the molecules of interest and instrument used. Besides the typical matrixes used in MS an alternative approach in IMS is the use of ionic matrixes. The use of aniline in combination with HCCA in IMS of rat brain tissue has shown to increase signal intensity, sensitivity, image quality and reproducibility.[132] In most cases the matrix is dissolved in a 50% solution of either acetonitrile or ethanol containing 0.1% trifluoracetic acid (TFA). This matrix is than deposited by air driven spray or as small droplets. Several reports have appeared about the deposition of seeding crystals before matrix deposition.[65-67] Seeding crystals are preformed matrix crystals, which are grinded into a fine powder. This powder is deposited on the sample surfaces in order to assist in the formation of matrix crystals after deposition of the matrix solution. For spraying of the matrix solution an air driven TLC sprayer can be used. However, in order to increase

the reproducibility between different samples an automated spray robot has been developed (described in more detail in chapter 7). Matrix can be added in droplets by piezodispensing[133,134] or acoustic deposition.[135] Using these techniques the matrix is added in reproducible quantities but the size of the droplets (~250 µm) determines the obtainable spatial resolution.

Imaging Mass Spectrometry at Cellular Length Scale Spatial Resolution[*]

3

Imaging mass spectrometry (IMS) allows the direct investigation of both the identity and spatial distribution of the entire molecular content directly in tissue sections, single cells and many other biological surfaces. We describe here the steps required to retrieve the molecular information from tissue sections using matrix-enhanced (ME) and metal-assisted (MetA) secondary ion mass spectrometry (SIMS) as well as matrix-assisted laser desorption/ionization (MALDI) IMS. These techniques require specific sample preparation steps directed at optimal signal intensity with minimal redistribution or modification of the sample analytes. After careful sample preparation, different IMS methods offer a unique discovery tool in, for example, the investigation of (1) drug transport and uptake, (2) biological processing steps and (3) biomarker distributions. In order to extract the relevant information from the huge datasets produced by IMS, new bioinformatics approaches have been developed. The duration of the protocol is highly dependent on sample size and technique used, but on average takes ~5h.

3.1 Introduction

Sequencing the human genome[3,4] was believed to lead to a further understanding of biological processes in diseased and healthy organisms. However, it has become apparent that understanding biological mechanisms cannot be achieved by merely having complete sequences of genomes. The cellular proteome is highly dynamic and genetic information alone cannot predict the function of a given protein.[8-10] Furthermore, the number of protein coding genes is far less than the number of actual proteins, resulting from alternative splicing and posttranslational modifications.[6,11-13] Several diseases are associated with altered (or miss) functioning of proteins caused by altered localization,[17-19] posttranslational modifications,[136-139] or expression levels.[18,140] Numerous different proteomic approaches are being employed to elucidate elements of this missing information in many different biological processes. Ultimately methods to study changes in the cellular proteome should interfere as little as possible with the natural behavior of the molecules of interest. Imaging mass spectrometry (IMS) has recently been recognized as a proteomic tool for in situ spatial analysis of molecules in (diseased) tissue.[9,24] IMS enables the direct investigation of, for example, the effect of a disease or drug treatment on the tissue microenvironment.

Imaging mass spectrometry

Matrix-assisted laser desorption/ionization (MALDI) MS has shown to be able to depict the localization of biomolecular components like proteins and peptides directly from tissue.[25,65,141-144] The spatial resolution in conventional microprobe IMS has been limited by the laser spot size and sample preparation issues. In microprobe experiments the tissue surface is scanned in an array of predefined points and at every point a mass spectrum is acquired. The corresponding molecular image is reconstructed after the analysis. The predefined points correspond to the pixels in the resulting image and their size, assumed square, is dependent on the size of the laser spot. The spatial resolution of MALDI imaging has been increased by developing optical lenses, able to focus the laser to submicron dimensions.[145] However, decreasing the laser spot size decreases the efficiency in MALDI for macromolecules. This is caused by the increased

laser fluence needed to reach the MALDI threshold when using smaller laser spots,[118,119] resulting in increased fragmentation of the macromolecules. This implies there will always be a trade off between signal intensity and spatial resolution in microprobe IMS. Another novel approach to increase spatial resolution in MALDI-IMS is oversampling with complete sample ablation, developed by Jurchen et al.[146] Here the MALDI matrix is ablated completely after which the sample stage is moved with increments smaller than the size of the laser beam. Although the resulting images show features smaller than 40 μm in size without the need to focus the laser beam, the study of large areas will be extremely time consuming.

Despite the limitation in obtainable spatial resolution, microprobe MALDI-IMS has proven to be a powerful extension of existing proteomic techniques. Sweedler and co-workers showed already in 2000 the ability of MALDI-MS to profile peptides in single cells and organelles.[31,62] In tissue, the localization of amyloid β peptides in relation to Alzheimer's disease,[63,64] the decrease of a neuronal calmodulin-binding protein (PEP-19) in relation to Parkinson's disease[65] and the accumulation of transthyretin Ser28-Gln146 in the cortex of affected kidneys after drug administration[66] has been shown using MALDI-IMS. Distinctly different protein profiles have been obtained when comparing tumor and non-tumor tissue within one tissue section.[67] Another very interesting application in IMS is the tracking of administered drugs. Using IMS it is possible to follow not only the parent molecule but also possible metabolites formed after administration.[63]

Mass microscope

A new approach to IMS decouples the obtainable spatial resolution from the dimensions of the footprint of the ionization beam, by using a stigmatic mass spectrometric microscope (Figure 1).[127] Here the desorbed ions retain their original spatial distribution from the tissue surface during their time-of-flight (ToF) separation and are imaged by a two-dimensional position sensitive detector. This approach allows for a high versatility in choosing the ionization method without influencing the obtainable spatial resolution. Using the mass microscope in combination with MALDI the spatial resolution depends solely on the quality of the ion optics and the detector resolution; spatial detail can be obtained from within the laser spot. Here the spatial resolution obtained in
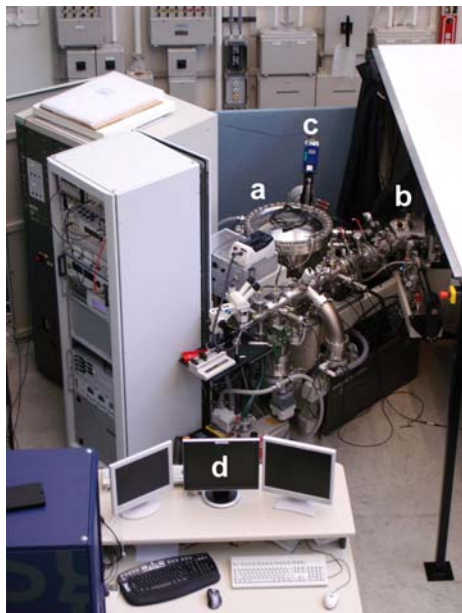
Figure 1. BioTrift Mass Microscope, with a) the triple ion focusing (TRIFT) time-of-flight, b) the MALDI laser source, c) the CCD camera and d) instrument control and data acquisition.

MALDI-IMS is comparable to that obtained in ME- and MetA-SIMS imaging experiments. Using relatively large laser spots (150×200 μm), which is favorable for MALDI efficiency, delivers an image quality of 500 nm pixel size and 4 μm resolving power both in IR and UV MALDI-MS.[127,147]

In our mass microscopy approach the 150×200 μm homogeneous laser pulse irradiates the sample surface. The desorbed ions pass an immersion lens/transfer lens combination followed by a high-speed blanker and are detected at a micro-channel-plate (MCP)/position sensitive detector (Figure 2A). In this manner a mass-to-charge separated series of molecular images is generated, allowing simultaneous recording of a microscope and microprobe dataset in a single experiment.

The position sensitive detector consists of a CCD camera phosphor screen assembly, where snapshots of the ions reaching the detector are taken. These snapshots are used to construct larger area stigmatic ion images. In order to construct a whole tissue image several linescans are taken over the entire tissue
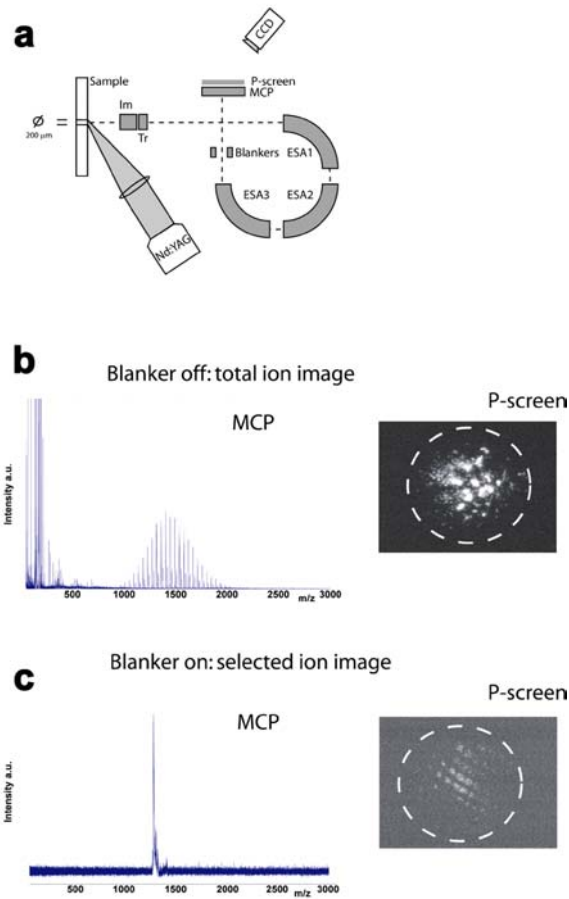
Figure 2. Instrumentation of the stigmatic mass microscope and a comparison with microprobe IMS. (A) Schematic representation of the Physical Electronics Trift II mass spectrometer (B) TIC and (C) SIC stigmatic ion imaging.

section, by moving the sample stage at a constant speed (typically 100 μm/s) using a continuously firing laser. At the end of a single linescan the sample stage is moved upwards by 60-80% of the laser spotsize and another linescan is taken, until the entire tissue section is measured (described in protocol). With in-house developed software all the single stigmatic ion images are stitched together to form a linescan image. These individual linescan images are then combined to form the total image of the entire tissue section. The overlap of the

consecutive laser shots is calculated and the intensity data of the overlapping areas is averaged in the images. The resulting image reveals a high-resolution picture of the sampled surface. Since the speed of the CCD camera is insufficient to record the high spatial resolution images for each analyte distribution reaching the detector within one cycle of the experiment, the stigmatic imaging experiment can be conducted in two modes. First, all the ions are allowed to pass through to the detector, to record stigmatic total-ion-count (TIC) images (Figure 2B) and second, the TRIFT high-speed blankers are used to record stigmatic selected-ion-count (SIC) images (Figure 2C). In the second case the high-speed blankers are used to remove all ions except the ones passing through a ~3 μs time window, which is set manually. In the mass spectrum a single isolated peak can be seen at the selected m/z position. Since only this single species reaches the position sensitive detector, high spatial resolution mass resolved images can be created.

The spatial resolution obtained with the mass microscope is unprecedented and extends IMS capabilities, complementary to existing fluorescence-based techniques. Still fluorescence-based techniques achieve superior resolution and allow the experiments to be carried out *in vivo*. The great benefit of IMS is that the biomolecular content of the sample is measured based on an intrinsic property, molecular mass, thus avoiding the need for a fluorescence label. Avoiding the need for labeling allows the technique to resolve in principal all surface molecules that ionize and omits possible interference of the label with the natural behavior/function of the analyte molecule. Simultaneous determination of protein localization, possible posttranslational modifications and expression levels can be achieved in a single experiment. The possibility to search for 'unknowns' qualifies IMS as a discovery tool and comparisons can be made between healthy and diseased tissue without prior prejudice.

Secondary ion mass spectrometry

In SIMS[69] the sample surface is bombarded with a high-energy primary ion beam between 5 and 25 kiloelectronvolts (keV). Typical primary ions used in SIMS include Ga^+, Cs^+ and In^+, with Ga^+ being able to provide the smallest probe size (less than 10 nm). Although SIMS does not routinely yield intact protein and peptide signals directly from tissue sections, it does have several advantages compared to MALDI. The most important advantage of SIMS over

MALDI is the chemical imaging capabilities routinely delivering submicron spatial resolution.[73] Furthermore, the SIMS technique is very sensitive and remarkably versatile since it can analyse almost any kind of solid surface.[104] The bombardment of these solid surfaces with high-energy primary ions will induce damage over a certain depth in the sample, resulting in changes in the molecular structure of the constituents in this area. To prevent imaging of the induced damage, SIMS imaging experiments are conducted using either a dynamic or a static regime. In the dynamic regime the entire sample surface is eroded in time and the complete top monolayer is removed. Dynamic SIMS is primarily used in quantitative elemental imaging[75,78,79] (not the topic of this protocol). In the static SIMS regime a much lower primary ion dose is used compared to dynamic SIMS resulting in less than 1% of the top surface atoms and molecules to interact with the primary ion beam and no primary ion strikes again the damaged region. Consequently, in static SIMS significantly less fragmentation of the molecular content occurs, which allows the technique to be used in imaging of small organic components.[74,86,148] In order to enhance the ionization yield for large intact molecular ions by SIMS, different kinds of surface modifications (MALDI matrices,[26,102,149-151] silver[152] and gold[103,105,106,153,154]) as well as the use of polyatomic primary ion beams[99,155-159] have been suggested. Although these methods have shown to be able to desorb and ionize peptide and proteins from model samples, in direct tissue analysis they are highly biased to lipids and steroids. One explanation for this phenomenon is the surface sensitivity of the technique. Since with SIMS only the top few monolayers are sampled, the technique favors the ionization of compounds with surface propensity like cholesterol and lipids, which are highly abundant in tissue sections.

In this protocol surface modifications in SIMS, such as metal-assisted (MetA) and matrix-enhanced (ME) SIMS are described for the ionization of intact biomolecular ions, increasing the applicability of SIMS to genuine biological problems. In MetA-SIMS a very thin layer (~1 nm) of a metal (e.g. gold) is deposited on the sample surface to assist in the desorption/ionization process.[103,104,153] One crucial factor in this method seems the migration of the analytes on the gold surface. In a recent study we have shown that SIMS signals for both cholesterol and the lipid phosphatidylcholine (PC) increased when these

species were deposited on a thin layer of gold. Increased signals for cholesterol were exclusively obtained when the layer of gold was deposited on top of the cholesterol and PC sample.[141] The same effect was observed in direct MetA-SIMS tissue analysis[141] as well as in a MetA-SIMS study of dyes by Adriaensen et al.[106]

Using ME-SIMS we have demonstrated the possibility of obtaining peptide signals, from a nervous tissue extract from the pond snail *Lymnaea stagnalis*, identical to those obtained with MALDI-MS, up to m/z 2590.[149] The analysis readily identified 5 known peptides with ME-SIMS using 2,5-dihydroxybenzoic acid as matrix. In ME-SIMS one is not dependent on the migration of the analyte molecules onto the matrix-covered surface, like in MetA-SIMS. The matrix is deposited in a wet environment and the analyte molecules are extracted from the tissue surface. Still the biases for species with surface propensity remains since during drying these species are pushed to the outside of the forming matrix crystals. Furthermore, sample preparation (described in the protocol) is more stringent since the size of the matrix crystals determines the obtainable spatial resolution.

A very recent innovation in MS, not discussed in the protocol, is desorption electrospray ionization (DESI), first described in 2004 by Takats et al.[160] Here charged droplets and ions of solvent are electrosprayed onto the surface to be analyzed. The impact of the charged particles on the surface produces gaseous ions of surface components. The resulting mass spectra are similar to normal ESI mass spectra in that they show mainly singly or multiply charged molecular ions of the analytes. The unique property of the technique is that the mass spectra can be obtained under ambient conditions, which allows the technique to analyze samples in their native environment.[161] The range of samples analyzed with the technique is already extensive, even though it is only two years old, and consists of pharmaceuticals,[162,163] explosives,[164] dyes,[165,166] and many other analytes, as well as biological samples like urine, serum and blood.[160,161,167] The DESI technique has also been used in tissue imaging[168] and could possibly move the field of IMS from *in vitro* to *in vivo* systems, imaging live systems (such as cell cultures or animal skin) with mass spectrometry. A possible obstacle in conventional microprobe imaging analysis is the spatial resolution since the DESI ionization beam is in the order of 0.5 to 1 mm.

Data analysis

In typical IMS analysis, processing the acquired data is more time consuming than the actual measurement itself. Data analysis can get very complicated because of the large amount of data produced. As a result powerful processing and displaying tools as well as automated data mining techniques are required.[169] One of the tools available for microprobe IMS datasets is BioMap[63,64] (Rausch, M. & Stoeckli, M. (http://www.maldi-msi.org/software/biomap.htm), which supports many more imaging modalities, such as optical and positron-emission-tomography (PET). It provides a common visualization and storage platform, which allows functionalities such as overlying of two individual datasets or displaying of regions of interest (ROIs).

Multivariate statistical methods, and especially principal component analysis (PCA), are established ways to efficiently extract information from large multidimensional datasets.[170] Combined with different preprocessing and visualization methods, they form a powerful analytical tool for the analysis of hyperspectral datasets, like the ones obtained in IMS. Using these techniques, chemically relevant spectral features can be extracted from large datasets.

Interpretation of MALDI-IMS data should be done very carefully since mixtures of multiple components, for example peptides, can experience preferential desorption and/or ionization.[123-125,171] Factors influencing the likelihood of ionization of specific peptides are charged side chains, presence of aromatic amino acids, peptide hydrophobicity, size and the ability to form a stable secondary structure.[125] Furthermore there is the so-called ion suppression effect, where dominant peptides in the desorption/ionization process suppress ionization of other peptides present at the surface.[124,125,171]

Sample preparation

Sample preparation in IMS is directed at observing the analytes of interest within the very complex environment of the tissue section. Choosing the appropriate matrix can enhance the sensitivity towards specific molecular moieties.[172] In general, in MALDI-TOF experiments, α-cyano-4-hydroxycinnamic acid (HCCA) gives the highest sensitivity in peptide analysis and sinapinic acid (SA) in protein analysis while 2,5-dihydroxybenzoic acid (DHB) gives good signal intensity in both mass ranges in a single experiment. Typically the matrices are dissolved in 50:50 water:acetonitrile or water:ethanol solutions with 0.1%

trifluoracetic acid (TFA). The percentage of organic solvent can be varied depending on the hydrophobicity of the analytes of interest. Increase of protein signals from cell lysate or tissue sections by the addition of amphiphilic detergents to the matrix solution or by the use of ionic matrices have been reported[132,173] (not the topic of this protocol).

Matrix deposition is probably the most difficult part in the sample preparation procedure. Homogeneous matrix crystals have to be formed on the tissue surface with, depending on technique used, a confined size and without redistribution of the analyte molecules. In microprobe MALDI IMS, the restrains on the matrix crystal size are less stringent since the laser spot sizes used are in the range of 100 to 200 μm. For these experiments, techniques like the acoustic matrix deposition method developed by Aerni et al.[135] can suffice. Here the sample is held facing down towards the matrix solution and droplets are ejected towards the sample by focused acoustic waves. On seeded tissue sections, the formed matrix spots are 200 to 300 μm in size. Successful protein imaging at low resolution could be achieved using this technique.[65,135]

For high resolution IMS however, the size of the matrix crystals is a key factor. In order to make optimal use of the spatial detail observed with the mass microscope the crystal sizes should be equal to or smaller than the size of a single pixel. In practice however, the goal is to achieve sufficient protein or peptide signals from matrix crystals smaller than the size of the tissue features of interest. Furthermore, the matrix application method should be robust and reproducible. These requirements can be met if the matrix arrives at the tissue surface in very small droplets before all solvent has evaporated. Matrix solutions can be sprayed into small droplets using pneumatic nebulisation (airbrush)[141,172] or electrospray nebulisation,[149,174] (Figure 3) the latter method giving smaller and more mono-disperse droplets. Automation of the pneumatic nebulisation is being developed for reproducibility and high-throughput analysis in our laboratory.

To optimize matrix crystallization a washing step has to be performed. The solvent composition can be chosen in such a way to optimize for the experiment at hand. In most cases the main concern is to wash away as much salt as possible to optimize matrix crystallization. Recent studies have shown that matrix crystallization and analyte incorporation is hampered by the presence of
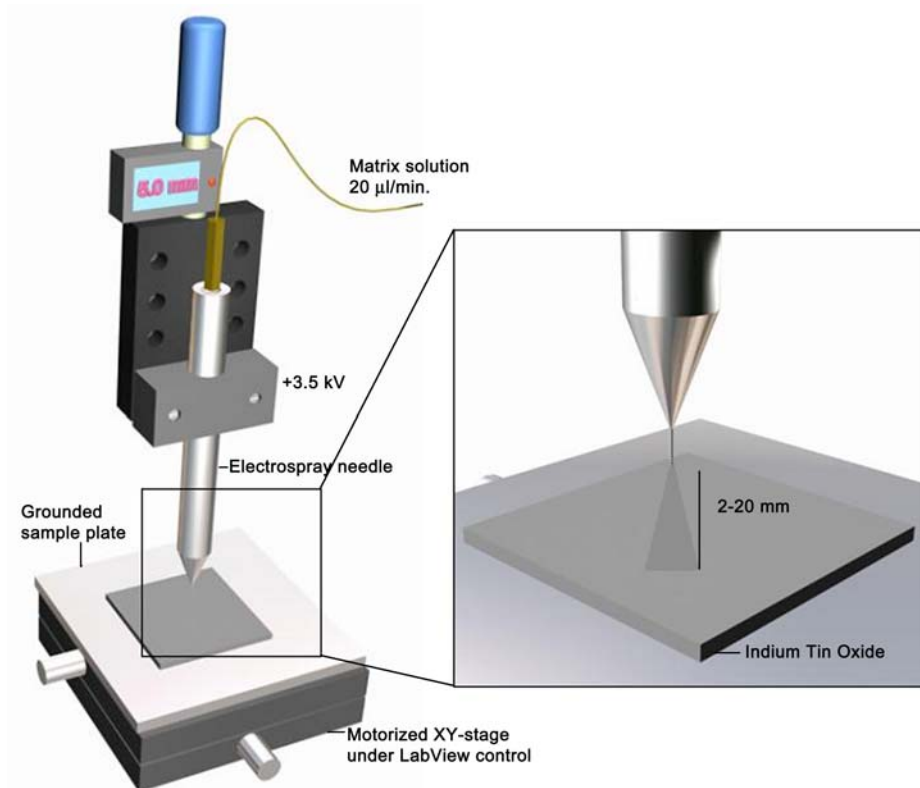
Figure 3. Schematic representation of the electrospray set-up.

high concentrations of salt. Furthermore segregation of the salt molecules from the matrix crystals results in an inhomogeneous sample surface where local variations influence the ionization process.[150,175,176] Washing the tissue sections can overcome these problems but great care has to be taken to prevent diffusion of the analyte molecules and/or washing away of the species of interest. The removal of salt from the tissue sections is typically realized by washing in 70-80% ethanol.[141,172] Recently, Lemaire et al.[131] showed the usefulness of more rigorous washing for the increase of peptide and protein signals, especially from older or even archived tissue sections. They showed that

the treatment of tissue sections with organic solvents such as chloroform, acetone, hexane, toluene, or xylene resulted in signal enhancement in MALDI direct tissue profiling. In this approach the tissue sections are not immersed in washing solvent but the solvent is dispensed on top of the sections using a glass syringe. The organic solvents remove interfering lipids and open up different lipid bilayers resulting in increased signal intensity but possibly also increased molecular diffusion by removal of the lipid structure. Therefore, when using lipid-extracting solvents as washing agent, one has to be extra careful in preventing diffusion of the molecules of interest, especially using high spatial resolution techniques.

Protocol

As described above the sample preparation steps are crucial for the success of the IMS experiments. From the dissection and sectioning of the tissue to the actual matrix application, the major concern is preparing MS compatible tissue samples (i.e. tissue sample giving the required information in a direct MALDI IMS experiment) while preventing analyte diffusion as much as possible. MS compatibility is a key issue in dissection and cryomicrotome cutting of the tissue sections. Blood sticking to the dissected organ should be limited as much as possible, no polymer based imbedding materials can be used and thickness of the tissue sections is limited. Further handling of the tissue samples is directed to attain as high as possible signal intensities with as little as possible redistribution of the analyte molecules. The protocols described here are guidelines to the different approaches of IMS. As an example we show the direct MALDI analysis of a rat brain tissue section both in microscope en microprobe mode.

3.2 Materials

REAGENTS
- α-cyano-4-hydroxycinnamic acid (HCCA) (Fluka; 70990) **!CAUTION** Irritating to the eyes, the respiratory system and the skin.

- 2,5-dihydroxybenzoic acid (DHB) (Fluka; 85707) **!CAUTION** Harmful if swallowed and irritating to the eyes, the respiratory system and the skin.
- Trifluoracetic acid (Aldrich; T6,220) **!CAUTION** Harmful by inhalation and causes severe burns. Harmful to aquatic organisms, may cause long-term adverse effects in the aquatic environment.
- HPLC grade water (Riedel-de Haën; 34877)
- Ethanol (Biosolve; 05250501) **!CAUTION** Highly Flammable
- Matrix solution: 15 mg/ml DHB or 10 mg/ml HCCA in 50% EtOH/0.1% TFA (electrospray deposition); 40 mg/ml DHB or 10 mg/ml HCCA in 50% EtOH/0.1% TFA (pressure driven deposition).
- Gelatine (De Twee Torens, Delft, The Netherlands)
- liquid isopentane, **!CAUTION** Isopentane can affect you when breathed in and can irritate the skin causing a rash or burning feeling on contact. Exposure to Isopentane can irritate the eyes, nose, and throat; can cause headache, nausea, weakness, dizziness, sleepiness, loss of coordination and even loss of consciousness. Repeated or prolonged contact with Isopentane can cause drying and cracking of the skin. Isopentane is a highly flammable liquid and a dangerous fire hazard.
- Dry ice
- Washing solution (1 and 2): ice-cold 70% ethanol.

EQUIPMENT
- Dissection microscope allowing low magnification (10×/40×) (CETI, Antwerpen, Belgium).
- Cryomicrotome; Leica CM 3000 cryostat (Leica Microsystems, Nussloch, Germany).
- Conductive glass slides; 25×50×1.1 mm unpolished float glass, SiO2 passivated/ indium-tin-oxide coated, Rs = 6±2 Ω (Delta Technologies; CG-40IN-1115)
- Applied Biosystems sample plate, SS, 100 well, numbers only, part number V503841
- -80 °C freezer.
- Desiccator containing a silica gel canister.

- Optical microscope (Leica DMRX) equipped with a digital camera (Nikon DXM1200).
- Chromatography sprayer, 10 ml (Sigma-Aldrich; Z529710).
- 9 mm screw top vials, 12×32 mm, (Waters, P/N 186000272).
- Quorum Technologies (Newhaven, East Sussex, U.K.) SC7640 sputter coater equipped with a gold target (SC510-314A), a FT7607 quartz crystal microbalance stage and a FT7690 film thickness monitor.
- Physical Electronics (Eden Prairie, MN) TRIFT-II (triple focusing time-of-flight) SIMS (ToF-SIMS) equipped with an $^{115}In^+$ liquid metal ion gun.
- Applied Biosystems 4700 proteomics MALDI TOF/TOF analyzer equipped with a 200 Hz Nd:YAG laser.

REAGENT SETUP
- Tissue sections

Male Wistar rats (Crl:WU) weighing 350 g were obtained from Charles River (Germany). **!CAUTION** Experimental procedures should be in accordance with current animal welfare regulation like the European directives (86/609/EEC).

Tissue samples: Freeze tissue directly in liquid isopentane after dissection, cool on dry ice and store at −80 ºC until use. When needed embed the tissue in compatible embedding material. For very small organs like the pituitary gland or a mollusk central nervous system (CNS), problems can arise during the cryomicrotome cutting process. Because of the small size of the organs, placement on the sample holder without contact with the support material is unlikely. Furthermore, the cutting of these small organs without embedding material increases the likelihood of damage in the resulting tissue sections, by rumpling or tearing. Embedding in non-polymer containing solutions like 10% gelatin or agarose helps to prevent damaging of the tissue and assist in cutting. Tissue is embedded in 10% gelatin at 30 ºC directly after dissection and frozen at −80 ºC. Gelatin embedding allows sectioning down to 5 μm thickness, results in no tissue damage during freezing and is compatible with MS.
CRITICAL STEP: Recent observations by Svensson et al.[177] point towards post-mortem changes in the proteome of susceptible peptides and proteins within minutes. To prevent these alterations of the sample Svensson et al.[177] use

focused microwave irradiation to sacrifice the animals. Since focused microwave irradiation is not available in every laboratory an alternative way to minimizing alterations is snap freezing of the dissected tissue and defrosting only just before sample preparation starts.

Never embed the tissue in polymer containing cryopreservative solution like Tissue-Tek O.C.T. Compound (product code #4583, Sakura Finetek USA, Inc.). Cryopreservative solutions will smear over the tissue surface during cutting and in the MS analysis the polymer signals will dominate.

EQUIPMENT SETUP

- **Home built electrospray deposition setup** In this setup, a syringe pump (KD Scientific) pumps matrix solution (10-50 μl/min) from a gastight syringe (Hamilton) through a stainless steel electrospray capillary (O.D. 220 μm, I.D. 100 μm) maintained at 3-5 kV (0-6 kV power supply, Heinzinger). The capillary is mounted on an electrically isolated manual translation stage (Thorlabs) in a vertical orientation. The stage is fitted with a digital micrometer (Mitutoyo) for accurate positioning of the needle tip with respect to the grounded sample plate. The sample plate is mounted on a XY moveable table (Thorlabs).

- **Mass spectrometer** Physical Electronics (Eden Prairie, MN) TRIFT-II mass spectrometer equipped with a MCP/phosphor screen/CCD camera (LaVision, Germany) optical detection combination and a MALDI ionization source (described in detail in reference 127). The instrument is equipped with a DP214 digitizer card with 1 GHz bandwidth and 2 GS/s sampling rate (acqiris, Switzerland) for readout of the MCP signals.

- **Software**
  (i) Both TRIFT systems are operated by WinCadence software (version 3.7.1.5) and controlled by the vacuum watcher (Physical Electronics, Watcher 2.1.2.140). AcqirisLive 2.11 controls the acqiris settings and data acquisition. LaVision, DaVis 6.2.3. controls the CCD camera settings and data acquisition.

  Mass spectral data analysis is performed with WinCadence 3.7.1.5, MatLab 7.0.4 (PCA), AWE3D 1.5.2.0 and tofToCsv (tool to convert entire m/z data file to a comma-separated-file (csv)). Image data

analysis is performed with WinCadence 3.7.1.5, MatLab 7.0.4 (PCA), DataCubeViewer, spatial image composer (SIC) and tof.bat. All software developed in our laboratory is available to other researchers on request.

(ii) The Applied Biosystems 4700 proteomics MALDI TOF/TOF analyzer is operated using the 4000 Series Explorer software. For imaging experiments an extra software package (4000 Series Imaging) is required which is freely available form the maldi-msi.org website.

Both mass spectral and image data analysis is performed using the BioMap software, which is freely available from the maldi-msi.org website.

3.3 Procedure

1│ Freeze tissue Place the dissected tissue on the sample holder in the cryostat. Tissue section can be attached to the sample holder by a very small amount of Tissue-Tek. Great care has to be taken that the Tissue-Tek does not come into contact with the tissue area of interest.

2│ Cut tissue section ~10 μm thick using a cryomicrotome at −20 ºC. 10 μm thickness is optimal for IMS; enough analyte molecules available for extraction and no problems with isolation.

3│ Pick up the tissue sections with either microscope glass slides or manufacturer sample plates, by thaw mounting (i.e. the tissue sticks to the glass or steel because it thaws slightly upon touching), place them in a closed container (e.g. plastic Petri dishes sealed with parafilm) on dry ice and store at −80 ºC until use.

CRITICAL STEP: Indium-tin-oxide glass slides show best performance in both microprobe and microscope mode imaging, because of the preserved conductivity of the sample.

4| Take a tissue section in its closed container from the −80 ºC storage and allow it to come to room temperature in a dry box with silica gel canisters before analysis.

CRITICAL STEP: When taking the samples out of the −80 ºC freezer, water condenses on the samples. For this reason samples are packed in Petri dishes closed by parafilm to prevent wetting of the tissue surface. The whole dish is placed in a desiccator, until the condensed water has been removed, after which the tissue is taken out of the Petri dish for washing.

5| Wash the tissue sections. The washing step is optional depending on the type of analysis. For (SIMS) analysis of small molecules like lipid messengers, steroids or even elemental distributions, the washing step is omitted to prevent diffusion. Also in the analysis of drug delivery systems, no washing step is used for this same reason.

For macromolecular analysis the washing is dependent on the type of analysis and the washing solution can be altered accordingly. For medium-size peptide analysis (i.e. ~1000-5000 Da) best results are obtained by washing twice in ice-cold 70% ethanol. Washing is achieved by following these steps: (i) Place the glass slide containing the tissue section in washing solution number one by immersing very gently and do not stir or shake. (ii) Leave the slide for one minute in the first washing solution and than take it out very gently and remove any big drops from the slide. (iii) Place the sample, again as gently as possible, in the second, fresh, washing solution for 1 minute. (iv) After the second washing step take out the slide, keep it in a horizontal position and gently blow a stream of nitrogen over the surface to assist in drying. (v) Place the tissue in the desiccator to let the tissue dry completely, else the tissue may detach from the glass slide and start to ripple.

CRITICAL STEP: Careful washing is critical in high spatial resolution imaging. To prevent diffusion of the analyte molecules place the sample in the washing solution as gently as possible and leave it untouched.

6| Matrix deposition is different depending on the spatial resolution required. For high spatial resolution IMS, electrospray deposition (ESD) in SIMS (Option A) and pressure driven spray, using a TLC sprayer, in MALDI (Option B) is used

in our experiments. The choice of matrix again determines the obtainable spatial resolution.

(A) Electrospray deposition

    (i)   Pump matrix solution, 15 mg/ml DHB or 10 mg/ml HCCA in 50% EtOH/0.1% TFA, from a gastight syringe through a stainless steel electrospray capillary maintained at 3.7 kV, for 10 min at a flow rate of 12 μl/h. Needle to sample plate distance is 5.0 mm. No drying or nebulisation gas is used. CRITICAL: Key issues in development of a matrix deposition method are optimal incorporation of analyte into the matrix crystals and minimal lateral diffusion. These two requirements can be met if the matrix arrives at the tissue surface in very small droplets before all solvent has evaporated.

       ?TROUBLESHOOTING

    (ii) Check matrix coverage using an optical microscope.

    (iii) Let the tissue sections dry for 30 min.

(B) Pressure driven deposition

    (i)   Use a TLC sprayer to spray matrix solution, 10 mg/ml HCCA or 40 mg/ml DHB in 50 % EtOH/0.1% TFA, at a nitrogen pressure of 0.3-0.4 bar. Use several spray cycles to achieve homogenous matrix coverage and allow the tissue to dry in-between the spray cycles in a horizontal position.

    (ii) Check matrix coverage using an optical microscope.

    (iii) Let the tissue sections dry before gold coating (30 min).

Gold coating for MetA-SIMS and stigmatic MALDI-IMS experiments.

7│ For MetA-SIMS, coat the tissue sections with 1 nm of gold directly on the tissue and for MALDI coat the matrix covered tissue sections with 4 nm of gold. This is done by performing the following steps: (i) Place the ITO slide with the sample in the Quorum Technologies SC7640 sputter coater. Make sure a gold target is installed. (ii) Press the start sequence button to pump down, flush with argon, further pump down the vacuum chamber and leak in argon until the pressure reaches 0.1 mbar (all done automatically). (iii) Enter the density of the metal used (19.30 g.cm^{-3} for gold) and the desired thickness of the sputtered

metal layer. (iv) Put the discharge voltage on 1 kV and press start. (v) Adjust the plasma current to 25 mA for homogenous coverage.

CRITICAL STEP: If the layers are too thick, only gold clusters will be observed.

Imaging mass spectrometry experiments

8│ IMS experiments described here are ME-SIMS, MetA-SIMS and MALDI experiments. The SIMS experiments are conducted on a Physical Electronics TRIFT-II equipped with an ^{115}In$^+$ liquid metal ion gun (SIMS). Stigmatic MALDI experiments on a Physical Electronics TRIFT-II equipped with a phosphor screen/CCD camera optical detection combination and a MALDI ionization source. The microprobe MALDI experiments on an Applied Biosystems 4700 proteomics analyzer.

The experimental procedure for the ME-SIMS and MetA-SIMS experiments is the same (Option A), but different from that for stigmatic MALDI (Option B) and microprobe MALDI (Option C).

(A) ME-SIMS and MetA-SIMS

(i) **Optimise setup for image quality.** Before conducting SIMS imaging experiments optimize the setup for image quality, using a copper grid with a 25 μm repeat. In the vacuum watcher close spectro gate valve (V5). In WinCadance software go to hardware, start the DC beam an raise the gain of the electron multiplier until the copper grid becomes visible on the secondary electron detector (SED).

(ii) Select lens 1 and wobble. Use the multiple variable aperture (MVA), on the side of the instrument to improve the image quality. When best result is achieved stop wobble, select lens 2 and start wobble again. Adjust beam steering (x and y) to improve the image quality when needed. At optimal image quality stop wobble, select blanker and start wobble again. This time adjust lens 2 to fix the image and lens 1 to refocus. After refocusing the procedure is repeated until a clear fixed and focused image of the copper grid can be seen on the SED.

(ii) In hardware make sure there is no voltage on the bunching parameter (perform the imaging measurements in unbunched mode for optimal image quality). Before the start of the experiment select under

acquisition set-up/advanced settings: save as raw file, in order to be able to post process the raw data after the measurement is completed.

(iii) **The experiment.** Perform the ME- or MetA-SIMS experiment in such a way that the analysis is conducted in the static SIMS regime. This can be achieved with a primary ion beam current of ~450 pA, a primary pulse length of 30 ns, a spot diameter of 500 nm and a primary ion energy of 15 kV. At 3 min per experiment this results in a primary ion dose of 4.9×10^{11} ions/cm^2.

(iv) For each chemical image, raster the primary beam over a 150×150 μm sample area, divided into 256×256 square pixels (larger or smaller areas can also be chosen). To image a significant larger surface, like a whole tissue section, analyze multiple 150×150 μm areas by stepping the sample stage in a mosaic pattern. To compensate for small deviations on the sample stage positioning take a 10 μm overlap with the previous acquired sample (the sample stage is moved by 140 μm).

(B) Stigmatic MALDI-IMS

(i) **Optimize setup for image quality.** Before conducting stigmatic MALDI imaging experiments optimize the setup for image quality, using a fine mesh TEM grid (19 μm squares, 25 μm pitch) overlain on analyte-doped matrix crystals. Optimize sample potential, immersion lens and transfer lens voltages to obtain a focused image of the grid structure on the phosphor screen.

(ii) **The experiment.** Set sample stage velocity on 0.1 mm/s and the laser repetition rate at 10 Hz.

(iii) Calculate the number of laser shots needed to complete one linescan over the tissue section and use this number as value for the number of images saved from the phosphor screen and mass spectra acquired.

(iv) After one linescan move the sample stage up by 60-80% of the laser spotsize and acquire another line scan. Repeat this step until the entire tissue section has been measured.

(C) Microprobe MALDI-IMS

(i) Load the ABI sample plate in the 4700 Proteomics Analyzer and determine the tissue section boundaries.

(ii) Take a test spectrum outside the tissue section to determine the acquisition method.

   CRITICAL STEP: the maximum number of data points per spectrum must always be lower than 32767. Increase the bin size or reduce the mass range to meet this criterion.

(iii) Select 'Manual Acquisition' with one spectrum, define up to 255 laser shots (100 laser shots in our case) and load the 4700 Imaging Tool (freely available from the maldi-msi.org website).

(iv) Set the coordinates of the tissue section boundaries and give the raster size, the numbers of pixels on the XY scale are calculated using the 'Dimensions' button. CRITICAL STEP: Increasing the number of pixels increases the level of detail in the imaged section. However, the size of the laser beam has to be taken into account to avoid multiple sampling of the same position.

(v) Give a file name and start the acquisition.

Data analysis

9│ **ME-SIMS and MetA-SIMS** (right after step 8A(iv)). In the WinCadence software each individual experiment is saved as .raw file to allow post processing of the data. In 'spectra' choose specific m/z ranges and select 'image' for each range. Now in 'acquisition', 'set-up/advanced settings' select 'acquire from raw file' and under the tab 'image' the selected distributions can be seen. For large tissue sections multiple imaging experiments are performed to cover the entire area. Viewing the tissue section in one image, made up out of the multiple experiments, can be accomplished by combining (stitching) the individual images. Two approaches of image stitching are available. First 150 μm^2 images are stitched together manually in image handling software like Adobe Photoshop. Second PCA based methods are used to generate feature based registration of the imaging data-cubes for the visualization of the imaging data.[178]

10│ **Stigmatic MALDI-IMS** (right after step 8B(iv)). For data analysis a problem-solving environment is developed, which is under continuous

improvement. Since two datasets are being recorded simultaneously, data can be processed separately and combined afterwards. The mass spectra can be analyzed as single shot spectra, combined spectra per linescan or combined spectra of the whole measurement. Microprobe images can be created with high detail per single mass, or at low detail for every mass and PCA routines[179] can be used to find correlations between distributions of m/z species. The stigmatic ion images can be stitched together showing either the total-ion-count (TIC) image of the entire tissue section or a high-resolution selected ion distribution.

(A) Mass spectral analysis

The MALDI mass spectral data is acquired using an Acqiris digitizer resulting in a single *.data file for every laser shot.

(i)   Mass spectral data can be visualized as single shot spectra per linescan in the 3D tool of AWE software.[180] A contour plot shows the m/z data on the x-axis and the selected ion current on the y-axis. The intensity data is presented in the z-direction as a heat plot allowing 3D visualization of the data. Using awe3D specific m/z species can be visualized per linescan without loosing low abundant signals in averaging logarithms.

(ii) Matlab routines add mass spectral data of a single linescan. These routines help in fast evaluation of the m/z species observed.

(iii) A Java routine (tofToCsv) is used to convert the entire mass spectral dataset into a comma-separated file, which can be visualized in e.g. Origin.

(B) Stigmatic image stitching

The stigmatic ion images are stitched together to form a linescan (spatial image composer (SIC)). These individual linescans are then combined to form the image of the entire tissue section (Figure 4a). The in-house developed software calculates the overlap of the consecutive laser shots and adds the intensity data of the overlapping areas in the images.

(C) Microprobe images

(i)   Detailed images are created using Java based software, which calculates intensity data for manually selected masses per laser-shot position. This low-resolution microprobe dataset is visualized, taking into account the sample stage velocity, laser repetition rate and
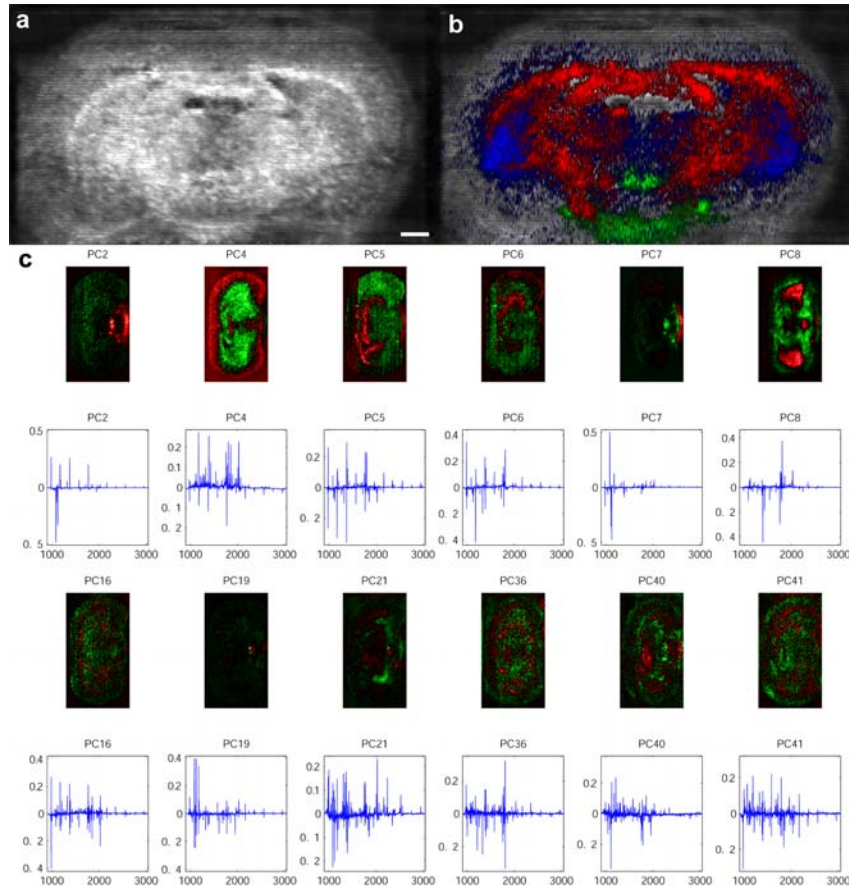
Figure 4. Example of images obtained with microscope MALDI-IMS. (**a**) High-resolution microscope mode TIC image of a rat brain tissue section. (**b**) The same microscope mode TIC image with overlain microprobe m/z data (m/z 1085 (vasopressin) in green, m/z 2030 in red and m/z 1431 in blue). (**c**) Correlation between different m/z species found in the microprobe dataset of the rat brain tissue section by PCA analysis. (Scale bar is 1 mm).

distance between linescans and can be overlain with the stigmatic ion images (Figure 4b). Image processing is done in imaging software like

Adobe Photoshop. **!CAUTION:** Software programs like Photoshop use automatic smoothing tools when rescaling or re-sampling the images.

(ii) Low resolution images of the entire microprobe dataset can be visualized using Data-cube-viewer. Here one can scroll trough the entire mass spectral dataset showing the 2D localization at every m/z value with the intensity data in the z-direction (comparable to the BioMap software).

(D) PCA

For the PCA, the acqiris ADC signals are read using MatLab (version 7.0.4, R14, SP2). The maximum size of the dataset is dependent on the available memory. Since the IMS datasets consist of relatively large areas with zero counts the data is stored in a Harwell-Boeing format, which omits the storage of zero counts. To further reduce the data size binning is performed. PCA is used to describe the original data by a pre-selected number of 'principal components' (PCs). These components are calculated to describe some percentage in variation (the variance) of the original spectral data. The components are calculated in descending order of variance. In this manner different correlated molecular components can be imaged together, rather than generating images of each individual peak in the dataset. As shown in Figure 4c, a single PC contains both a positive and negative spatial correlation (on the positive and negative scale in the graph and in red and green in the image). Many different types of spectral correlations can be found, for example the negative correlation in PC2, in Fig 4c, consists mainly of different pseudomolecular ions of the neuropeptide vasopressin. This technique can assist in finding biological processing steps in specialized regions in the tissue.

11│ **Microprobe MALDI-IMS** (right after step 8C(iv)). For the data analysis of the microprobe MALDI-IMS experiment we use the BioMap 3.7.4 software, which is freely available from the maldi-msi.org website. In our example we obtained the IMS dataset on an Applied Biosystems 4700 proteomics analyzer, which creates a, BioMap compatible, *.img file. However, datasets obtained with the Bruker Reflex IV or the Ultraflex II are also compatible with the BioMap software

after an additional conversion routine (available free of charge, details are described by Clerens, S. et al.[181]).

(i) Load the IMS dataset into BioMap by choosing the .img file in 'file' 'import' 'MSI'.

CRITICAL STEP: BioMap loads the entire dataset into the computers virtual memory and thus sufficient memory is needed (for medium sized datasets 2Gb).

(ii) Once the dataset is loaded into BioMap multiple visualization and data handling routines are available. Since the possibilities are too extensive to discuss in this protocol only some of the basic steps to visualizing the data are discussed. An example of images obtained with a microprobe IMS experiment and processed with the BioMap software is shown in Figure 5.

▪ The summed spectra of the imaging experiment can de visualized in the 'plot tool' ('analysis' 'plot' 'global' 'scan').

▪ Contrast of the selected m/z images can be adjusted by adjusting the minimum and maximum intensity value on the slide-bars in left-side toolbar. **!CAUTION:** The data is automatically shown as interpolated
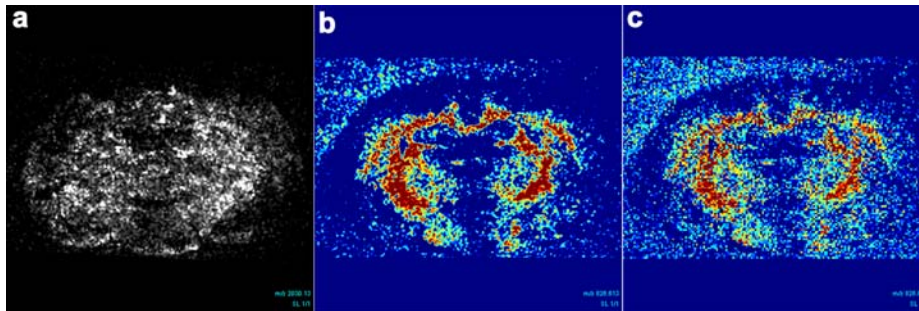
Figure 5. Example of images obtained with microprobe MALDI-IMS on an Applied Biosystems 4700 proteomics analyzer and processed with BioMap software. (**a**) Distribution of a selected mass (m/z 2030) in grayscale and (**b**) of a selected mass (m/z 826.6) in color scale (Split-blue-red). (**c**) Same image as in panel b but now without interpolation.

(smoothed) images. For the real (pixelated) image one has to choose 'voxel' instead of 'interpolate' in the 'display methods' of the image properties window (right mouse click on image) as shown in Figure 5C.

▪ Different m/z images can be selected either by scrolling through the mass spectrum in the plot tool or by adjusting the value of the datapoints in the left-side toolbar.

▪ The color of the images shown can be changed in the left-side toolbar by choosing the 'Set color table' button.

Troubleshooting

Step 6B(i)

The pressure on the sprayer is adjusted according to matrix solution used. For higher concentration solutions a higher pressure is needed. Also after several spray cycles sometimes a little higher pressure is needed due to small deposits of the matrix in the sprayer's tubes. The average pressure used is 0.3-0.4 bar.

Since the TLC sprayer's solution reservoir is relatively large compared to the amount of matrix solution needed to cover a single tissue section, use a smaller container (9 mm screw top vials, 12×32 mm from Waters) fill it with the matrix solution and place it inside the TLC container.

TIME LINE:

The timing of a single IMS experiment is difficult to indicate since this is very much dependent on the size of the sample to be analyzed. Furthermore, the time needed for data analysis depends heavily on the questions asked. For example if IMS is used to find information on a known species in the sample the answer can be found relatively fast after data processing. If, on the other hand, one is using the IMS technique as a discovery tool and for example wants to discriminate between (drug) treated and untreated or diseased and healthy tissue the data mining and comparison will take considerably longer.

As a general guideline:

Step 4,   Defrosting and drying of tissue sections 30 min.

Step 5,   Washing and drying of the tissue sections 10 min.

Step 6,   Electrospray matrix deposition 10 min (highly dependent on the size of the tissue section).

Pressure driven deposition 30 min.

Step 7,   Gold deposition 6 min. (~1.5 min per nm).

Step 8,   Highly dependent on the size of the tissue section.

ME-SIMS analysis: 3 min per 150 μm^2 area of the tissue section.

Stigmatic MALDI-IMS: For a rat brain tissue section (~1.5×0.9 mm) take a linescan of 1550 shots, which corresponds to 155 s. With a 120 μm stepsize between 2 linescans, 70 linescans are needed to complete the tissue section. This results in 3 h pure measuring time. Together with resetting all the parameters at the beginning of the measurement of each linescan a whole tissue section takes ~4 h to measure.

Microprobe MALDI-IMS of a single rat brain tissue section takes (depending on number of pixels and number of laser shots per pixel) ~4h to measure.

Step 9,   The construction of a single image takes ~0.5 min. The stitching of multiple images by hand is more time consuming and can take several hours depending on the sample size. Using PCA software this can be done much faster, depending on data size, processor speed and available memory, typically within one hour.

Step 10, Data analysis for MALDI-IMS using Data-cube-viewer or PCA based software, where both images and spectral information is processed at once, is relatively fast. The time limiting factor is the size of the dataset in combination with available processing power and memory. Loading and processing of the dataset typically takes 1 hour after which all information is readily available.

Information extracted by Data-cube-viewer and PCA can be analyzed in detail by the above described software tools.

Step 11, Data analysis for microprobe MALDI-IMS using the BioMap software is relatively fast. The loading of the dataset takes typically not more than 10 minutes after which the data readily available for investigation.

3.4 ANTICIPATED RESULTS

The described protocols for IMS allow the mapping of molecular distributions directly in tissue sections. The different approaches to SIMS are able to deliver images of distributions of small organic compounds like lipids, steroids and drugs, within single cells. Figure 4 shows a typical set of images obtained using MALDI IMS. In Figure 4A a TIC image of the rat brain tissue section shows the high spatial resolution imaging capabilities of the mass microscope. Figure 4B shows that the, in the same experiment recorded, m/z data can be used to show the distribution of both known and unknown species observed in the mass spectrum. In Figure 4C PCA and varimax analysis are used to show the localization of correlated molecular species within the features of the tissue section. The found correlation between the different molecular species can assist in the search for biological processing steps in specific areas of the tissue at cellular length scale spatial resolution.

Gold-Enhanced Biomolecular Surface Imaging of Cells and Tissue by SIMS and MALDI Mass Spectrometry[*]

4

Surface metallization by plasma coating enhances desorption/ionization of membrane components such as lipids and sterols in imaging time-of-flight secondary ion mass spectrometry (ToF-SIMS) of tissues and cells. High-resolution images of cholesterol and other membrane components were obtained for neuroblastoma cells, and revealed subcellular details (resolving power 1.5 μm). Alternatively, in matrix enhanced SIMS, 2,5-dihydroxybenzoic acid electrosprayed on neuroblastoma cells allowed intact molecular-ion imaging of phosphatidylcholine and sphingomyelin at the cellular level. Gold deposition on top of matrix-coated rat brain tissue sections strongly enhanced image quality and signal intensity in stigmatic matrix-assisted laser desorption/ionization imaging mass spectrometry. High-quality total ion count images were acquired and the neuropeptide vasopressin was localized in the rat brain tissue section at the hypothalamic area around the third ventricle. Although the mechanism of signal enhancement by gold deposition is under debate, the results we have obtained for cells and tissue sections illustrate the potential of this sample preparation technique for biomolecular surface imaging by mass spectrometry.

4.1 Introduction

Unraveling the spatial distribution of cellular membrane components is an important research topic in current molecular cell biology. Understanding the behavior and function of the major constituents of these membranes, i.e., lipids and sterols, has been hampered by methodological limitations, despite their relatively simple structures. Most of the current knowledge on lipid localization has been obtained using fluorescence imaging techniques.[22,182-184] The drawback of this technique is the need for fluorescent labeling of the molecule of interest. This is especially difficult in the case of lipids where only a few anti-lipid antibodies or specific lipid-binding protein domains[185] are available for fluorescent read-out. Artificial fluorescent probes are used that completely replace one of the fatty acid chains,[183,184] potentially resulting in perturbation of the lipid (physico)chemical properties.[183-185]

Ideally, a molecular imaging method should image the distribution of the native membrane components, omitting labeling altogether. One of the emerging alternatives in this field is imaging mass spectrometry, which provides both chemical specificity and spatial distributions of native components present at a bioorganic surface.[25] Recently, imaging matrix-assisted laser desorption/ionization mass spectrometry (MALDI-MS)[60] has been recognized as a tool for *in situ* proteomic tissue analysis.[9,24] Imaging MALDI-MS can typically analyze molecules up to 100 kDa, but has a limited spatial resolution of ~30-100 µm.[67,186] Secondary ion mass spectrometry (SIMS) can routinely achieve submicrometer spatial resolution,[73] using primary ion beams such as Ga^+. However, the sensitivity for high mass ions is limited due low secondary ion yields[187] as well as low detection efficiencies in current SIMS instrumentation.[188] SIMS has been used for imaging of elements (Na, K, Ca, etc.) in cells at high spatial resolution (~50 nm)[78,79] and in molecular imaging of (freeze fractured) single cells, showing only specific lipid fragments such as the phosphocholine headgroup at *m/z* 184 Da.[91-93,148]

In conventional SIMS analysis, a very thin (mono-)layer of sample is deposited on a surface. To enhance the ionization yield for large intact molecular ions by SIMS, different kinds of surface modifications (MALDI matrixes,[26,102,149-151]

silver,[152] and gold[103,105,106,153,154]) as well as the use of polyatomic primary ion beams[99,155-159] have been reported. Metallization of (organic) samples with silver and gold has been demonstrated to increase secondary ion yields of intact molecular ions in SIMS,[103,105,106,152-154] this technique is named Metal-Assisted (MetA) SIMS. The exact mechanism leading to the enhanced sputter yields of organic species after metallization is still under debate. Several explanations have been proposed: First, migration of mobile analytes onto gold nanoislands.[109] Second, gold enhances desorption/ionization by cooperative elevation of analyte molecules and metal atoms with similar momentum, as shown by molecular dynamics simulations.[108] Third, gold acts as cationizing agent leading to improved ion formation.[153,189] Additionally, suppression of surface charging by the presence of gold has shown to improve the quality of the images obtained for insulating samples.[103]

Another way of modifying the bioorganic surface is deposition of a MALDI matrix. Already in 1996, Wu and Odom[102] showed that MALDI sample preparation protocols can be used in SIMS to enhance the desorption/ionization yield of "large" molecular species. This technique is named matrix-enhanced (ME)-SIMS. In MALDI the presence of a matrix results in less fragmentation of the molecular ions by removal of most of the incident beam energy and collisional cooling of the ions in the plume with the matrix molecules.[101] We recently showed the usefulness of ME-SIMS in direct molecular imaging of biological tissue at subcellular resolution.[26,149] as well as in the analysis of phospholipids.[150] Here we compare ME-SIMS and MetA-SIMS in the direct molecular analysis of single neuroblastoma cells and rat brain tissue sections. Both techniques deliver high-resolution images of different molecular distributions at cellular resolution, without the need to label the target molecules. In addition, we show that gold coating of matrix sprayed rat brain tissue sections results in improved MS image quality of neuropeptide distributions in stigmatic MALDI imaging MS.

4.2 Experimental Section

Materials

2,5-Dihydroxybenzoic acid (DHB), α-cyano-4-hydroxycinnamic acid (HCCA), trifluoracetic acid (TFA), HPLC grade water, sucrose, cholesterol, and phosphatidylcholine (PC) brain extract were purchased from Sigma-Aldrich (Zwijndrecht, The Netherlands). Ethanol and methanol were purchased from Biosolve (Valkenswaard, The Netherlands).

Cell Cultures

Neuroblastoma cells were seeded in six-well plates at ~25.000 cells/well on conductive indium tin oxide (ITO)-coated glass slides (Delta Technologies, Stillwater, MN) and cultured in 3 ml of DMEM (Invitrogen, Breda, The Netherlands) supplemented with 10% serum and antibiotics. The cells were washed in 300 mM sucrose solution and milli-Q water after which they were frozen on dry ice, freeze-dried for 30 min, and stored at −80 °C. Prior to mass spectrometry the cell cultures were brought to room temperature in a desiccator over a silica gel canister (1 h). Conservation of cell morphology was checked by optical microscopy, using a Leica DMRX microscope with a Nikon DXM1200 digital camera.

Tissue Sections

Experimental procedures were in accordance with the European directives (86/609/EEC) and approved by the Commission on Laboratory Animal Experiments of the University Medical Centre Utrecht. Male Wistar rats (Crl:WU) weighing 350 g were obtained from Charles River (Germany). Rats were decapitated without prior anesthesia, and brains were dissected and frozen in liquid isopentane, cooled to −50 °C on dry ice, and then stored at −80 °C until sectioning. The 10-µm-thick rat brain tissue sections were cut at Interaural 7.2/Bregma −1.8 mm,[43] using a cryomicrotome. Sections were thaw-mounted on ITO-coated glass slides and were stored at −80 °C until use. Prior to mass spectrometry, tissue sections were brought to room temperature in a desiccator over a silica gel canister (1 h). For stigmatic MALDI experiments, tissues were briefly washed in cold 70% ethanol and dried at room temperature before matrix deposition.[172]

Matrix deposition

ME-SIMS matrix was applied using electrospray deposition as described previously.[190,191] Briefly, a 15 mg/ml solution of 2,5-DHB in 50% MeOH/0.1% TFA was pumped for 10 min at a flow rate of 12 µl/h from a stainless steel capillary (o.d. 220 µm, i.d. 100 µm) held at 3.8 keV and 5.0 mm over the grounded, maneuverable sample plate. Alternatively, a TLC sprayer (Sigma) was used to spray the same matrix solution for ME-SIMS, or 10 mg/ml HCCA in 50% EtOH/0.1% TFA, for MALDI-MS. The nitrogen pressure required for efficient nebulization was 0.3-0.4 bar.

Gold Deposition

Gold was sputter coated on the sample surface using a Quorum Technologies (Newhaven, East Sussex, U.K.) SC7640 sputter coater equipped with a FT7607 quartz crystal microbalance stage and a FT7690 film thickness monitor.

Mass Spectrometry

All static SIMS experiments were performed on a Physical Electronics (Eden Prairie, MN) TRIFT-II ToF-SIMS equipped with an ^{115}In$^+$ liquid metal ion gun, as described in chapter 2. In the ME-SIMS experiments, charge compensation was achieved by flooding the sample with low-energy electrons (29 eV, 40 nA, 2-mm-diameter spot) between each primary ion pulse. The ion dose was such that all analyses were conducted in the static SIMS regime (4.9×10^{11} ions/cm^2). The instrument was calibrated on the low-mass fragments CH_3, C_2H_5, and C_3H_5, which resulted in a mass accuracy for the imaging optimized instrument between 100 and 300 ppm, for the mass range between 0 and 1000 Da.

MALDI stigmatic imaging MS was performed on an extensively modified TRIFT-II instrument equipped with a nitrogen laser source and a phosphor screen/CCD camera combination as described in detail in chapter 2.

MALDI Data Processing

Single-shot 200-µm total ion count (TIC) MALDI stigmatic images were acquired and stored as tagged image file format (tiff) files with the corresponding synchronized ADC signals (Acqiris, Geneva, Switzerland). To image an entire rat brain, the sample stage was moved at 100 µm/s at a laser repetition rate of 9

Hz in a line scan. At the end of the line scan, the stage was stepped in the y direction by 150 µm. This process was repeated 62 times until the entire surface was imaged. Software was developed in-house to align all 1450 overlapping single-shot images into a line scan and, subsequently, all 63 line scans into an image. This high-resolution TIC image (resolving power ~4 µm) was overlaid with the course resolution ADC data (150 × 11 µm) at each position, a color scale indicating the intensity of the selected *m/z* for the image.

4.3 Results and Discussion

SIMS, ME-SIMS and MetA-SIMS of Lipids in Dried-Droplet Samples
Figure 1A shows a SIMS spectrum of a total brain phosphatidylcholine (PC) extract obtained with a 15-keV [115]In primary ion beam. Besides the low-mass fragments (not shown to prevent domination of the spectra), including the abundant choline headgroup fragment at *m/z* 184, no high-mass species are obtained. In Figure 1B, the PC extract is mixed with the MALDI matrix DHB and the ME-SIMS spectrum clearly shows the protonated molecular ions between *m/z* 700 and 800, as well as the protonated lipid dimers around *m/z* 1500. In Figure 1C, a spectrum is shown of PC spotted on a gold-coated (1-nm) silicon wafer, measured with the same 15-keV [115]In primary ion beam. The spectrum is very similar to the one obtained with ME-SIMS. The only difference between the two spectra is the presence of a gold cationized species at *m/z* 956 in the spectrum of PC from the gold-coated target. However, the protonated species at *m/z* 761 shows a ~5-fold higher intensity over the cationized PC. The same behavior is observed for other lipid species deposited on a gold-coated sample target. Since most of the PC will be present on the sample in its protonated form, the intensity enhancement effect of the gold-coated target seems to be more related to enhanced lipid desorption/ionization than cationization.
Figure 1D shows an experiment where first the PC is spotted on a silicon wafer after which 1-nm of gold is deposited on top of the sample. The sample was measured directly after metal coating, after 3 and 6 h, and the following day. The spectrum shows intense gold cluster ions, but the protonated or cationized
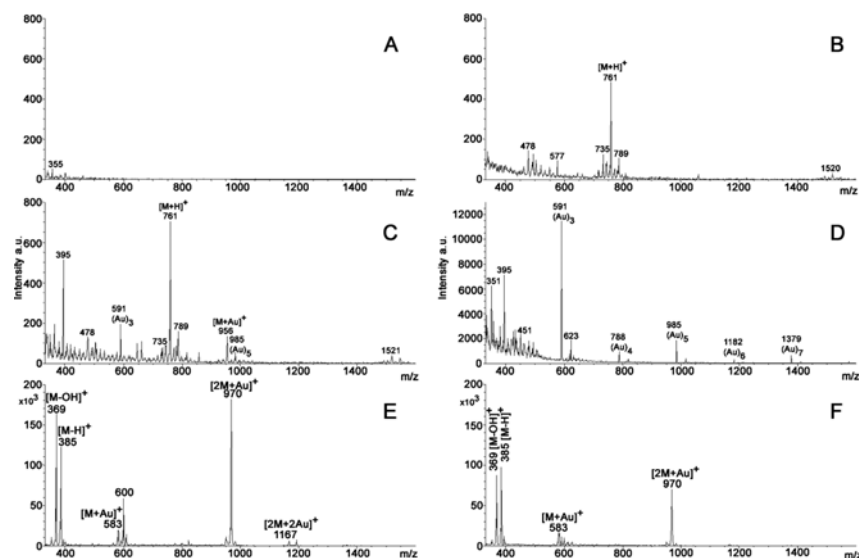
Figure 1. The influence of surface modification on phosphatidylcholine (PC) and cholesterol signals in SIMS. (A) SIMS spectrum of PC. (B) ME-SIMS spectrum of PC in 2,5 DHB (dried droplet). (C) SIMS spectrum of PC spotted on a gold-coated silicon wafer. (D) MetA-SIMS spectrum of PC spotted on a silicon wafer, covered by 1-nm of gold. (E) SIMS spectrum of cholesterol spotted on a gold-coated silicon wafer. (F) MetA-SIMS spectrum of cholesterol spotted on a silicon wafer, covered by 1-nm of gold.

molecular ion species of PC could not be detected. Another PC sample was placed in an oven, heated to 60 °C, and measured at similar time points, but here also no PC ions could be found. These results are in contrast to polymer studies, where a 2-nm overlayer of gold yielded either intense metal cationized species or signal enhancement for the protonated species.[153] A study by Adriaensen et al.[106] showed that the molecular information became visible after one or two weeks waiting, but this approach is biologically irrelevant. For comparison, the spectra in Figure 1 E and F show the SIMS spectra of cholesterol where either the cholesterol is spotted on the gold-coated target (1E) or the gold is sputtered on top of the cholesterol (1F). In both cases,

abundant cholesterol-derived pseudomolecular ions can be seen at *m/z* 369 [M-OH]$^+$ and *m/z* 385 [M-H]$^+$ as well as cationized species at *m/z* 583 [M+Au]$^+$, *m/z* 970 [2M+Au]$^+$, and *m/z* 1167 [2M+2Au]$^+$. The cholesterol sample gave the abundant signals right after metal coating. These results point to a molecule specific enhancement of the gold overlayer.

SIMS, ME-SIMS and MetA-SIMS in Direct Imaging of Rat Brain Tissue Sections

Raising the complexity of the biomolecular surface from a moderately complex PC mixture to a brain tissue section poses a challenge for ME-SIMS and MetA-SIMS (or any other MS imaging technique). The 10-µm-thick rat brain cryosections were cut at the level of the hypothalamus, using a cryomicrotome. Figure 2A shows a SIMS experiment directly on the tissue surface. In the spectrum, different diacylglycerol (DAG) and phospholipid species can be seen, however, at relatively low signal intensities. In the SIMS-only experiment, the total-ion-count (TIC) image shows a high-resolution image of the ventricle but the phospholipid signal intensities are too low to allow molecule-specific imaging experiments. To enhance molecular signal intensities in a previous study, we used electrospray matrix deposition yielding micrometer-sized matrix crystals at the tissue section surface.[149] In our current study, we use a TLC sprayer resulting in matrix crystal sizes of ~20 µm. To improve the crystallization of these relatively large crystals the tissue was washed in ice-cold 70% ethanol solution. These large matrix crystals result in a significant increase of the phospholipid signals shown in Figure 2B. The TIC image, however, is completely dominated by matrix crystal structures and the phospholipid signals co-localize within these crystal structures.This example clearly shows that matrix deposition resulting in large matrix crystals compromises the visible detail in SIMS analysis. Comparing panels A and B in Figure 2, an increase in signal intensity by 1 order of magnitude is observed for PC while the ceramide and DAG signals in the *m/z* 500-600 range increase only by a factor of 2, indicating reduced fragmentation in ME-SIMS. Except for the lipid signals, the spectrum shows no other molecular signals in ME-SIMS, while measuring this same section in our stigmatic MALDI instrument yielded signals up to 4000 Da. The major difference between the two approaches relates to the amount of sample consumed. While in SIMS the penetration depth is typically 10 nm, in MALDI each laser shot
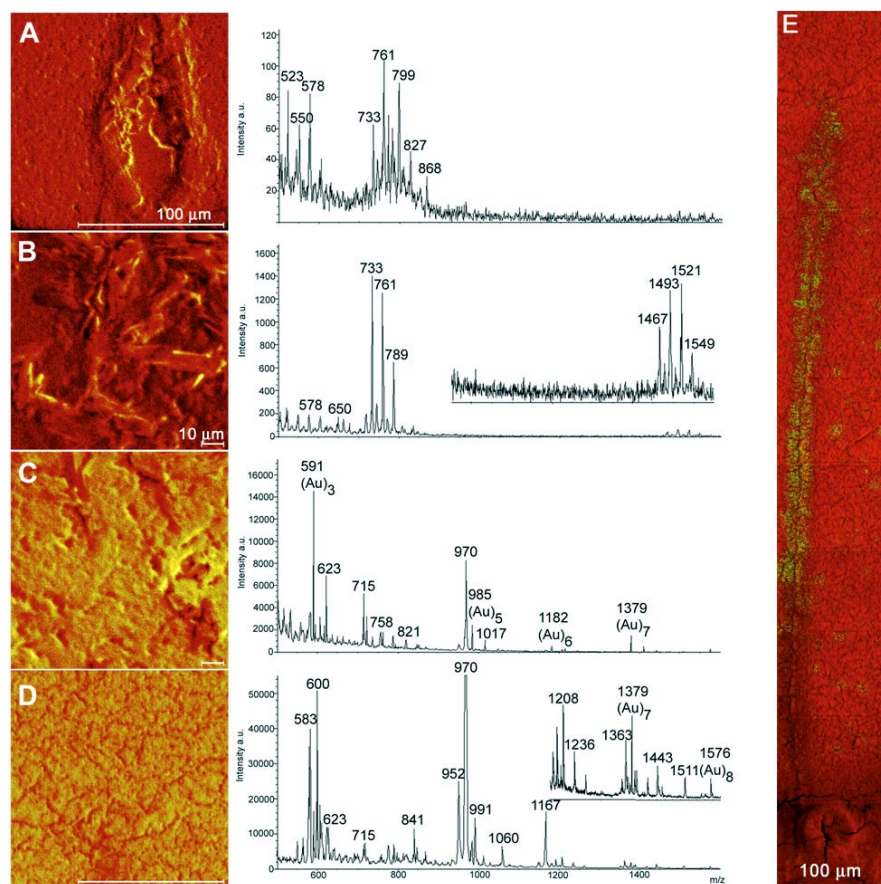
Figure 2. Total ion count (TIC) images and corresponding mass spectra of rat brain tissue sections after surface modification. (A) SIMS analysis of an untreated tissue section (scale bar 100 μm, 0-200 counts). (B) ME-SIMS analysis of a tissue section after TLC sprayed 2,5 DHB matrix (scale bar 10 μm, 0-350 counts). (C) ME-gold-SIMS analysis of tissue sprayed with 2,5 DHB and subsequently coated with 1-nm gold (scale bar 10 μm, 0-500 counts). (D) MetA-SIMS analysis of a tissue section coated with 1-nm gold (scale bar 100 μm, 0-1000 counts). (E) Mosaic of twenty MetA-SIMS experiments of the ventricle area of a rat brain tissue section after deposition of 1-nm of gold with in red TIC (0-800 counts) and in green localization of the ion at *m/z* 1443 (0-3 counts) (scale bar 100 μm). The total ion dose was 1.8×10^{12} ions/cm^2 in panels A, D and E, 5.1×10^{12} ions/cm^2 in panel B and 1.97×10^{12} ions/cm^2 in panel C.

consumes approximately 100 nm-1 µm of sample. A study by Hanton et al.,[191] showed that segregation of different molecular species occurs during crystallization of the matrix, and that ME-SIMS and MALDI yield different spectra for (complex) mixtures. These results agree with our observations where ME-SIMS and MALDI analysis of the same tissue section yield markedly different spectra. During crystallization, the surface-active lipids largely migrate to the crystal surface where they are readily accessible to the SIMS primary ion beam. Conversely, salts are excluded from the crystals altogether while peptides are mainly incorporated into the matrix crystals, the latter resulting in intense MALDI signals. To image peptide distributions with ME-SIMS, the crystal sizes have to be in the order of the sampling depth of the primary ion beam, strongly compromising sensitivity.

Figure 2C shows the effect of 1-nm of gold on top of the matrix crystals on the tissue. This approach results in reduced surface charging and therefore preserves the ion-optical image quality in stigmatic MALDI imaging. Furthermore, gold coating has been shown to increase signal intensity in conventional microprobe MALDI imaging.[192] In Figure 2C the dominant phospholipid signals have largely disappeared, and in addition to gold cluster signals, multiple novel signals are observed, which cannot be assigned to any of the commonly observed lipids. Inspecting the localization of the peaks observed in the gold-covered ME-SIMS spectrum reveals that several of the gold-enhanced ions localize within the crystals (for example *m/z* 970; data not shown), while others are present over the entire imaged area. Figure 2D shows the spectrum of a MetA-SIMS experiment, where a 1-nm layer of gold was deposited on an unwashed tissue section. Several of the observed peaks correspond to those in the gold-coated ME-SIMS spectrum, including the very abundant cholesterol [2M+Au]$^+$ peak at *m/z* 970. Several of the other abundant peaks (i.e., *m/z* 583, 600, 970, 952, and 1167) can also be attributed to cholesterol as can be seen from a comparison with Figure 1E. In the higher mass range, however, species are observed that do not correspond to cholesterol or the cationized lipid species, which are normally observed in SIMS spectra. These peaks remain yet unassigned, illustrating the need for SIMS tandem MS. That these species are tissue derived and not introduced by the gold coating can be seen from the overlay of the ion at *m/z* 1443 (green) with

the TIC image of the ventricle area in the rat brain (red), depicted in Figure 2 E. Here, a rat brain tissue section was covered with 1-nm of gold and the sample stage was stepped in a mosaic pattern, after which the resulting images were aligned to produce a single molecular image of the ventricle area in the rat brain. As can be seen from this image, the ion at *m/z* 1443 localizes very precisely within the ventricle as well as in some select areas in the neighboring tissue. Furthermore, these results show that the use of gold produces images with very high spatial resolution. In addition to the newly observed ions, it is clear from inspection of the intensity axes in Figure 2A-D that progressively the absolute signal intensity increases over 2 orders of magnitude. These high count rates are essential for imaging experiments where image contrast largely relies on the dynamic range within an image (also see Figures 3 and 6).

ME-SIMS Imaging of Single Neuroblastoma Cells
In tissue sections, the majority of the cells are transversely cut by the cryomicrotome displaying both membrane ridges between adjacent cells as well as cytosolic components and organelles. Single cells, however, grown on glass slides, frozen, and dried, pose a fundamentally different type of biological surface. In single-cell imaging MS studies, mainly cell surface components are likely to be sampled by the primary ion beam. Since ME-SIMS and especially MetA-SIMS are capable of imaging biological surfaces with very high spatial resolution, these techniques could be very well suited for direct analysis of lipid distributions on single-cell surfaces. For ME-SIMS the cells, grown on conductive ITO-coated glass slides, were covered with a thin layer of matrix by electrospray deposition yielding small (0.3-1 µm) matrix crystals. The crystal sizes obtained with the TLC sprayer, shown in Figure 2B and C, were in the order of 20 µm. Since a typical neuroblastoma cell is around 50 µm, one such crystal would cover half the cell body and thus the morphology of the matrix crystals, instead of the cell, would dominate the MS image. A second reason for the use of electrospray deposition is the thickness of the matrix layer and the SIMS sampling depth as already mentioned.
Figure 3 shows the capability of ME-SIMS to image the molecular ion distribution of intact lipids directly from single neuroblastoma cells. The ME-SIMS spectrum of these cell surfaces shows several lipid species in the mass range between *m/z*
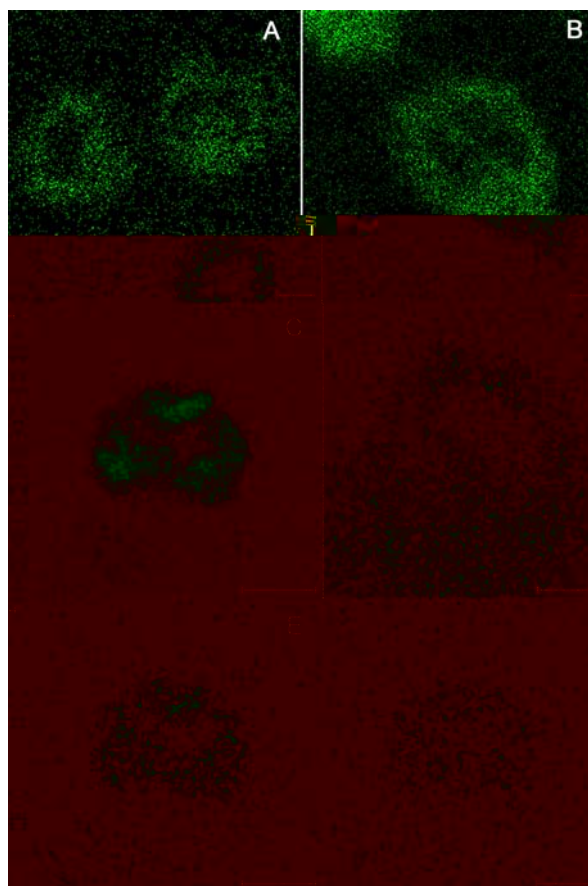
Figure 3. Molecular images of single neuroblastoma cells obtained with ME-SIMS. Selected ion count (SIC) images are (A) cholesterol fragment [M-OH]$^+$ (*m/z* 369, 0-5 counts), (B) cholesterol fragment (*m/z* 369, 0-7 counts), (C) phosphocholine headgroup (*m/z* 184, 0-7 counts). (D) Cholesterol fragment (*m/z* 369, 0-4 counts). (E) PC (*m/z* 761, 0-3 counts) and (F) SM (*m/z* 787, 0-3 counts). Panels C-F are acquired in the same experiment from the same cell. Scale bar in all images: 10 μm. Total ion dose A-B: 2.8×10^{12} ions/cm^2 and C-F: 8.0×10^{12} ions/cm^2.

700 and 900, ceramide and DAG species between *m/z* 500 and 700, and organic fragments in the lower mass range. The phospholipids; phosphatidylcholine and sphingomyelin (SM) can be readily identified (Table 1), together with the pseudomolecular ion signal for cholesterol at *m/z* 385 [M-H]$^+$ and the dominant fragment at *m/z* 369 [M-OH]$^+$. For comparison, using conventional SIMS without any matrix, only elements and low-mass organic fragments such as the phosphocholine headgroup (*m/z* 184) are observed.

Table 1. Phosphatidylcholine and sphingomyelin signals observed in single-cell ME-SIMS imaging experiments.

m/z	Ion
733	[SM+H]+ 18:0/16:1 / [PC+H]+ 16:0/16:1
747	[PE+H]+ 18:0/18:1
759	[SM+H]+ 20:1/16:1 / [PC+H]+ 16:0/18:2
761	[PC+H]+ 16:0/18:1
783	[PC+Na]+ 16:0/18:1
787	[SM+H]+ 22:0/16:1 / [PC+H]+ 18:1/18:1
789	[PC+H]+ 18:0/18:1
809	[PC+H]+ 20:4/18:1
811	[PC+H]+ 20:3/18:1

Panels A and B in Figure 3 show ME-SIMS images of the distribution of cholesterol in neuroblastoma cells. The images show the distribution of the dominant cholesterol fragment ion at *m/z* 369, over a 75×75 µm area. Figure 3A clearly shows three separate cells present in the imaged area, with the bottom cell only partly sampled by the SIMS ionization beam. The images show high cholesterol signal intensity at the border of the cells, the plasma membrane, compared to the center of the cells, corresponding to the nuclei. This observation is in line with previous observations where cholesterol was found primarily in the plasma membrane.[26,149,193]

Panels C-F in Figure 3 show ME-SIMS images of the same single neuroblastoma cell. The images correspond to a field of view of 40×40 µm and are centered on the *m/z* 184 signal, which is present in high concentrations in the nuclear membrane. The signals corresponding to the phosphocholine headgroup (Figure 3C) and the molecular ions of PC and SM, panels 3E and F, respectively, are all localized in the nuclear region. The cholesterol signal, and thus the plasma membrane, is partially outside the field of view. The lipid species are predominantly present along the border of the nucleus, as building blocks of the nuclear membrane. The nuclear signals are surrounded by the cholesterol

signal, corresponding to cellular outline formed by the plasma membrane (Figure 3D). The signal of ceramide species co-localize with the cholesterol signal (data not shown), in line with several reports.[194-197] The components of the nuclear membrane can be observed in the SIMS analysis since they dissolve in the acidic matrix solution upon spraying. This can occur when the plasma and nuclear membranes make contact during the drying process of the cells before matrix deposition. Figure 4 shows an optical image (50×50 µm) of a single neuroblastoma cell obtained with a differential interference contrast (DIC)
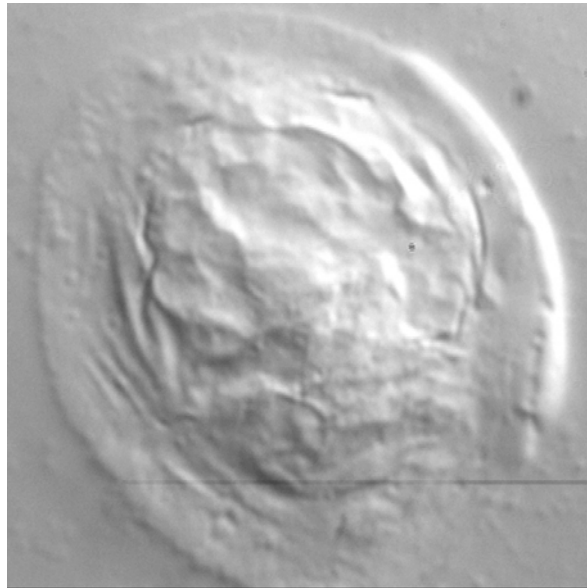
Figure 4. Differential interference contrast (DIC) microscope image of a single neuroblastoma cell after washing and drying. Field of view: 50×50 µm.

microscope. The image clearly shows that the outside rim of the cell is much flatter than the center where the nucleus is located. To keep the damage to the cells as limited as possible, the cells are first washed in a 300 mM sucrose

solution to wash away the salts from the growth medium while preventing hypotonic shock resulting in cell lysis. For this reason the second wash step, with milli-Q water, is a quick rinse followed by prompt drying in a vacuum chamber. The timing of the milli-Q wash is critical; exposure of the cells to water longer than 30 s results in hypotonic shock for >90% of the cells. Although intact lipids such as PC and SM are localized within the cellular outlines by ME-SIMS, a higher resolution MS technique in combination with a higher dynamic range and higher intensity signals would improve SIMS for molecular imaging of complex biological surfaces. Gold coating, analogous to tissue imaging (Figure 2D), can be used to enhance the ion yields from single cells.

MetA-SIMS Imaging of Single Neuroblastoma Cells
In Figure 5, the MetA-SIMS spectrum of single neuroblastoma cell surfaces coated with 1-nm gold is shown. In panel A the lowest mass range (*m/z* 0-250) was blanked to prevent saturation of the detector with low-mass ions, with no further effect on the measurement. In the mass range between *m/z* 250 and 500, a very abundant pseudomolecular ion signal of cholesterol (*m/z* 385) together with the dominant fragment ion (*m/z* 369) can be observed. Upon gold deposition, a very rich mass spectral signature is observed consisting of signals in the *m/z* 500-1300 range. No readily interpretable masses were observed other than cholesterol and a DAG species (*m/z* 607). Count rates for most ions in the spectrum were high enough to allow imaging and thus localization of the signals. Almost all of the species observed, other than the gold clusters, co-localize with the neuroblastoma cell surfaces.

The use of gold to enhance the secondary ion yield also greatly enhances the image quality in imaging SIMS experiments[103], as can be seen in Figure 6. Figure 6 shows selected ion count (SIC) images of three separate experiments (panels A and B, C and D, and panel E). The first four rows (A-D) show images of multiple cells within a 150×150 μm field of view. The last row (E) shows an image of a single cell in a 75×75 μm field of view. Several localization patterns can be distinguished: in panel A, cholesterol is found on the entire cell surface, with higher intensity at the cellular outlines, whereas the *m/z* 607 signal is highly intensive at the outline only. In panel B, the localization of the
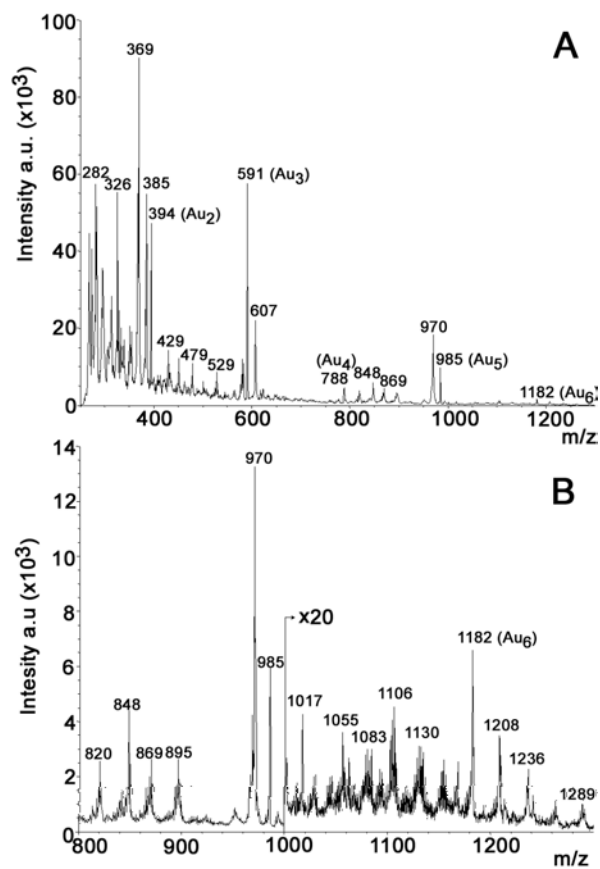
Figure 5. MetA-SIMS spectrum of neuroblastoma cells after deposition of 1-nm gold. (A) Mass range 250-1300 Da; low-mass ions (<250 Da) were blanked to prevent detector saturation. (B) The same spectrum, zoomed-in on the 800-1300 Da mass range. The spectrum was obtained by sampling a 150 × 150 μm area by the primary ion beam. $(Au)_n$ marks indicate the gold cluster *m/z* values.

pseudomolecular cholesterol ion at *m/z* 970 follows that of the *m/z* 369 pseudomolecular ion; however, the increased signal intensity at the cell outlines is not observed. This difference in localization between different pseudomolecular ions of the same molecular species had been observed before and is described elsewhere.[89] The *m/z* 1080 signal in panel 6B shows a distribution throughout the cell surface and only the overlay of *m/z* 970/1080 shows that at the cellular outlines the *m/z* 1080 signal is absent, illustrating the power of overlaying SIC images in two colors to pinpoint subtleties in
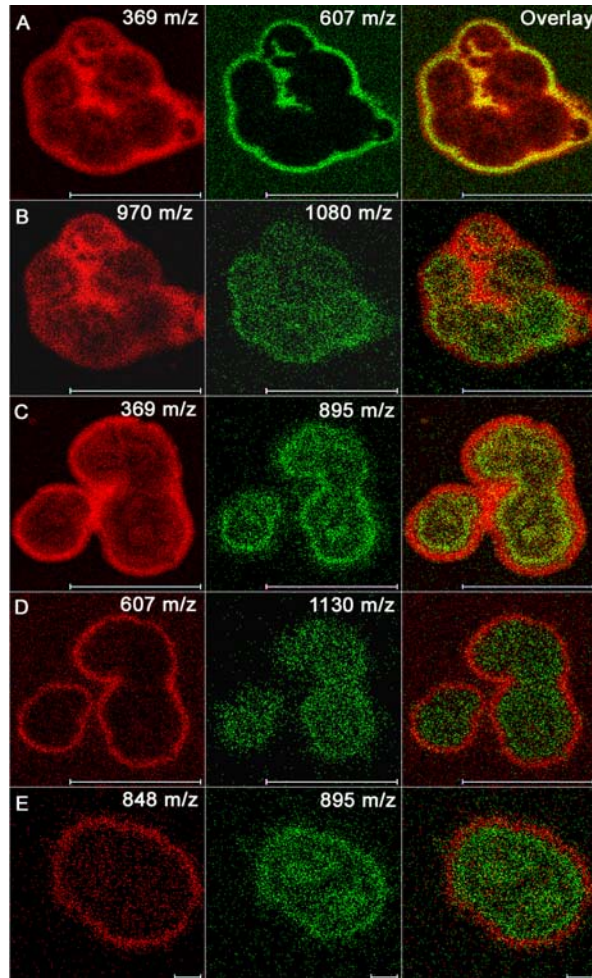
Figure 6. Cellular localization of MetA-SIMS selected ion count signals from neuroblastoma cells. Cells were imaged after deposition of 1-nm gold. (A) *m/z* 369 (cholesterol [M-OH]$^+$, 0-14 counts) and *m/z* 607 (DAG, 0-6 counts). (B) *m/z* 970 (cholesterol [2M+Au]$^+$, 0-4 counts) and *m/z* 1080 (0-1 counts). (C) *m/z* 369 (cholesterol [M-OH]$^+$, 0-12 counts) and *m/z* 895 (0-2 counts). (D) *m/z* 607 (DAG, 0-4 counts) and *m/z* 1130 (0-1 counts). (E) *m/z* 848 (0-1 counts) and *m/z* 895 (0-1 counts). (Au)$_n$ marks indicate the gold-cluster *m/z* values. Scale bar: 100 μm in panels A-D and 10 μm in panel E. Total ion dose 1.18×10^{12} ions/cm^2 in panels A-D and 4.7×10^{12} ions/cm^2 in panel E.

localization. In panel C, the cholesterol and *m/z* 895 distributions show an intermediate pattern, between A and B. The *m/z* 895 signal localizes at the cellular surface with increased intensity at the outlines and on first sight co-localizes with cholesterol. However, the overlay shows that the cellular outline is highlighted by the cholesterol signal whereas *m/z* 895 localizes on the cell

surface, like *m/z* 1080. Similar behavior is observed for *m/z* 607 and *m/z* 1130 in panel D, which shows the same cell cluster. Also, in panel E, this type of localization is observed for *m/z* 848 and *m/z* 895. Although identification of the well-localized signals in Figure 6 is required for the technique to be relevant for biology, the potential of MetA-SIMS for biological surface imaging is high. Compared to ME-SIMS, the lateral resolution of MetA-SIMS is higher. In our previous ME-SIMS imaging study of *Lymnaea stagnalis* nervous tissue,[149] we calculated an experimental resolving power. The resolving power is a convolution of the SIMS instrumental spatial resolution and the sample handling/matrix deposition protocol. The resolving power is calculated from a line scan analysis. For the cholesterol image, shown in Figure 6A, the MetA-SIMS resolving power is 1.5 μm, a factor of ~2 better than determined previously for ME-SIMS.[149] In Figure 6C, it can be seen that the obtained spatial resolution is high enough to distinguish subcellular details.

MetA-SIMS Imaging of Molecular Distributions in Growth Cones
The high spatial resolution capabilities of MetA-SIMS make it possible to study the distribution of different molecular species at subcellular length scales. Figure 7 shows a MetA-SIMS experiment of a single neuroblastoma cell containing an axonal growth cone. Growth cones are highly motile and sensitive structures responsible for the correct wiring of axons and dendrites in the developing nervous system. Growth cones are able to select the correct path toward their target by responding to the appropriate set of molecular signals.[198-200] One of the questions related to this system is whether the molecular content of the neuroblastoma cell body is similar to the developing axon and the growth cone. Since with MetA-SIMS the obtainable spatial resolution has been shown to be 2 μm the molecular distributions within the axon can de shown. Figure 7 shows the preliminary results on the MetA-SIMS imaging experiment of these growth cones. In Figure 7A the distribution of the [M-OH]$^+$ species of cholesterol at 369 m/z is shown. A very intense signal is seen in the cell body and a less intense signal in the growth cone. In the cell body the signal is concentrated in the centre due to the drying of the cell as shown in Figure 4. In the axon the signal is difficult to distinguish because of the drying artifacts of the sample and the resulting shadowing effect in the SIMS experiment. Still a decrease in signal

intensity is can be observed compared to the signal in the cell body and the growth cone. Figure 7B shows the distribution of the [2M+Au]$^+$ signal of cholesterol at 970 m/z. The distribution of the [2M+Au]$^+$ signal of cholesterol is very different from the [M-OH]$^+$ signal probably caused by the increased formation of gold islands at the rim of the cell. The contrast in this image is slightly better and now it can be clearly seen that cholesterol is much less abundant in the axon compared to the growth cone and cell body. These results show the possibilities of a high spatial resolution imaging technique like MetA-SIMS in mapping molecular distributions at cellular length scales and below.
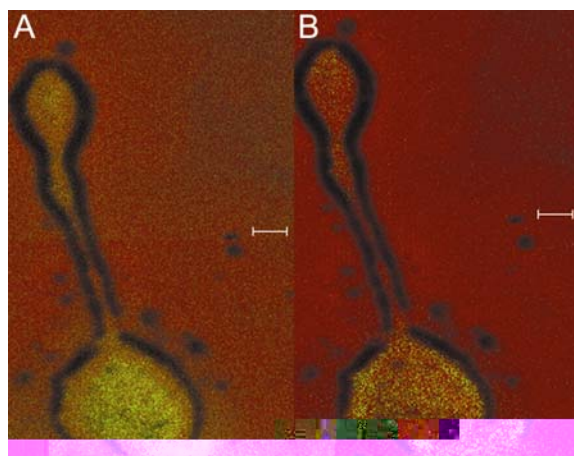
Figure 7. Localization of cholesterol in a single neuroblastoma cell body, axon and growth cone. Distribution of A) the [M-OH]$^+$ and B) the [2M+Au]$^+$ pseudomolecular ion of cholesterol overlain on the TIC image. Scale bar is 10 µm.

Comparison of SIMS, ME-SIMS and MetA-SIMS for Single Cell Imaging
Using conventional static SIMS, several lipids are observed but no intact-molecule imaging is possible at the cellular level. However, the technique does not require any surface modification and therefore does not introduce artifacts. In a ME-SIMS spectrum, several lipid species and their fragments can be identified and imaged but signal intensities in the higher mass range are still relatively low. To increase the yield of the higher mass species, larger matrix crystals are required, compromising spatial detail. Furthermore, ME-SIMS requires extensive surface modification since surface analytes have to be

incorporated in the matrix crystals (i.e., surface wetting will occur). Conversely, MetA-SIMS relies on a gas-phase deposition process and, therefore, does not require liquid-surface interaction. In MetA-SIMS, lateral analyte diffusion is minimized, only on the nanometer scale migration on gold islands may occur. The signal intensity of cholesterol in the MetA-SIMS experiment is ~50 times higher compared to the DHB-coated samples. In MetA-SIMS, the area where abundant phospholipid peaks could be seen in the ME-SIMS spectrum has changed dramatically. In the region between m/z 500 and 800, where in the ME-SIMS spectrum ion signals corresponding to ceramide, DAG, and phospholipid species could be found, almost no signal can be seen. The region between m/z 800 and 1300 on the other hand shows a large number of peaks, which are not obtained by ME-SIMS. The MetA-SIMS spectra in Figures 2 and 5 are quite similar, indicating that MetA-SIMS signals are most likely generic cell membrane components such as lipids. For MetA-SIMS to become a biological relevant technique these peaks have to assigned, again showing the need for tandem MS in SIMS.

The mechanism of MetA-SIMS and the role of the gold layer are still unclear. Previously, migration of mobile analytes onto gold nanoislands has been proposed.[105,109] Atomic force microscopy (AFM) showed that gold islands in the order of 100 nm are formed on tissue (Figure 8.). Indeed, increased signal
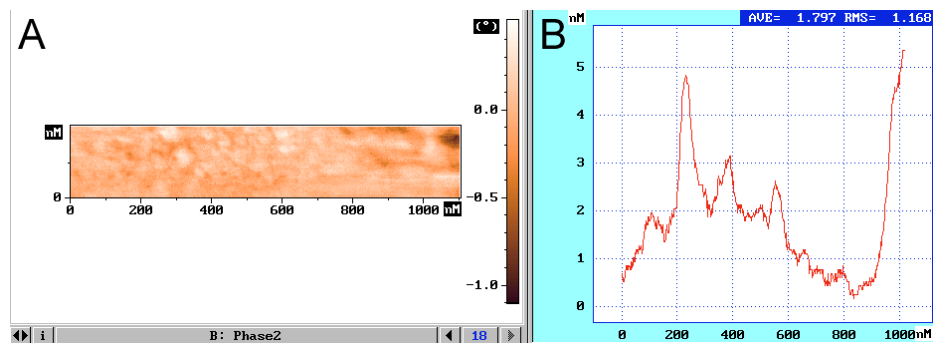
Figure 8. AFM measurement of gold nanoislands on top of a tissue section. A) AFM image of the tissue surface. B) plot of the width and height of the observed islands.

intensities were obtained for a mobile analyte like cholesterol when gold was deposited on a thin cholesterol layer. However, migration of surface-active phospholipids onto gold nanoislands is not seen, not from the thin-layer preparation or from the tissue sections or cells. Delcorte et al.[105] already showed this explanation to be questionable for larger molecules (2000 Da). Another explanation is the increased stopping power by a layer of gold. However, stopping power is only increased if the sample surface is gold and the analytes are deposited as a thin (mono-)layer on top, this is not the case for tissues or cells *covered* by gold. Yet another mechanism includes gold as cationizing agent leading to improved ion formation.[153,189] Indeed, several of the observed signals are cationized by gold in the MetA-SIMS experiments. However, the dominant species found in SIMS and ME-SIMS analysis are not found in MetA-SIMS, neither protonated nor cationized. Furthermore, gold deposition on the matrix crystals in the ME-SIMS analysis, revealed species within these crystals not observed before. These observations point to a molecule-selective enhancement by the sputtered gold.

Gold-Enhanced MALDI Imaging of Rat Brain Sections
Not only for SIMS but also for MALDI-MS imaging, gold deposition results in enhanced image quality and signal intensity. In conventional microprobe MALDI imaging MS (~100 µm laser spot) gold deposition on matrix-covered tissue sections resulted in enhanced signal intensity.[192] Here we show the effect of gold deposition on tissue using a stigmatic imaging MALDI mass spectrometer. In stigmatic imaging, a large surface area (200 µm) is illuminated by a laser and the spatial origin of the desorbed molecules is retained during the Time-of-Flight separation.[127] In stigmatic MALDI imaging, the MS image quality is not related to laser spot size but is related to the quality of the ion optics. The stigmatic TRIFT II instrument ion optics are sensitive to changes in the sample potential. Isolating samples such as tissue sections are prone to charging (and hence potential bias) and therefore result in extensively blurred stigmatic images. Deposition of 5 nm of gold on top of pneumatically sprayed HCCA matrix reduces charging of the tissue section and, therefore, improves stigmatic MALDI image quality. In Figure 9, a stigmatic MALDI imaging experiment of rat brain tissue is shown. To image a large surface area, such as a rat brain tissue

87
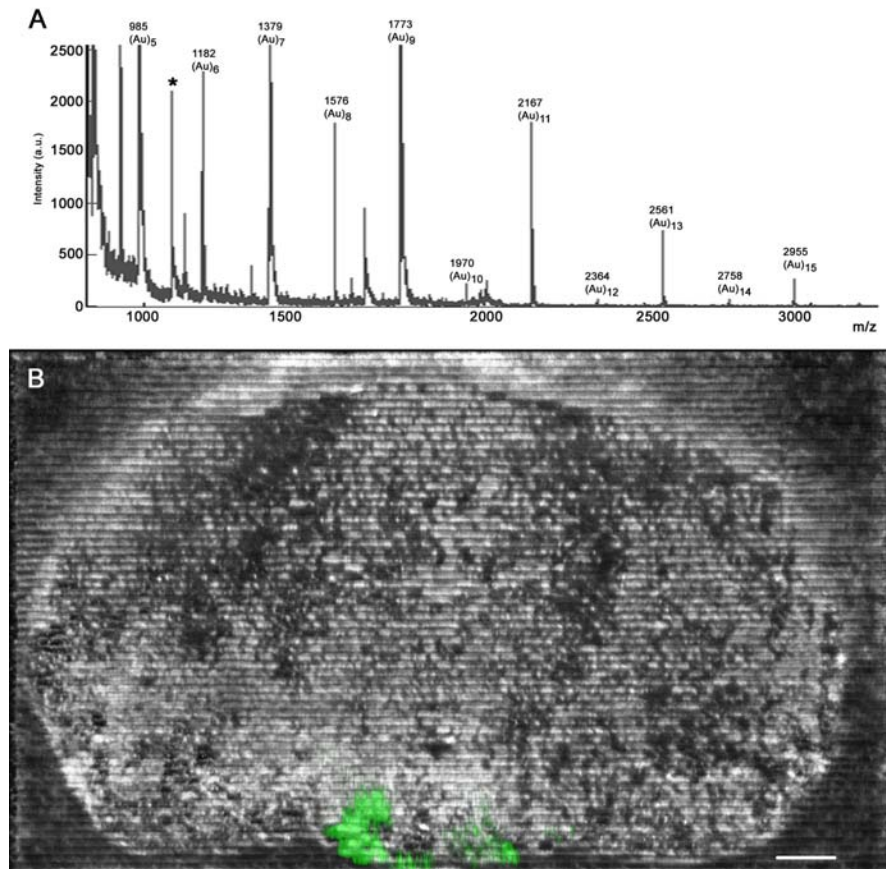
Figure 9. MALDI stigmatic imaging of a rat brain tissue section. (A) A line-scan summed mass spectrum showing gold cluster peaks and several peptide peaks, with the vasopressin mass at *m/z* 1085 (*). (B) The TIC image (gray-scale) of a 4-HCCA coated rat brain tissue section overlaid with the selected ion image for vasopressin (green). Scale bar: 1 mm.

section, the sample stage is stepped under a continuously firing laser beam. Single-shot images and spectra are recorded at 9 Hz while the sample stage moves in a line scan at 100 µm/s. In Figure 9A, the summed mass spectrum of a line scan over the rat brain is shown. Multiple well-resolved peaks in the 800-

2500 Da range are obtained, among which a dominant signal for the neuropeptide vasopressin at *m/z* 1085 (*).

Figure 9B shows 63 line scans, of 1450 individual images each, aligned using in-house-developed software (spatial image composer 0.8) to construct a rat brain TIC image (gray scale). The TIC image is overlaid with the molecule-specific image of vasopressin (green), which is constructed from the mass spectral data of the individual laser shots. Imaging MS localizes vasopressin in the hypothalamic area around the third ventricle, where it is known to be synthesized and released,[201,202] and where the V1b vasopressin receptor has been localized previously by immunohistochemistry.[203] The same experiment omitting gold deposition resulted in both blurred TIC images and reduced signal intensity (neuropeptide localization was not possible). Only after gold deposition the results shown in Figure 9 could be obtained.

4.4 Conclusions

ME-SIMS enhances lipid molecular ion signals over conventional static SIMS at the expense of surface analyte diffusion and surface corrugation by matrix deposition. MetA-SIMS shows highly enhanced as well as new signals from cells and tissues after gold deposition without lateral analyte diffusion, but analyte identification is required for interpretation of the high-resolution ion images in a biological context.

The effect of gold deposition on MALDI stigmatic imaging is most likely related to suppression of surface charging and provides a straightforward sample preparation strategy for MALDI-MS imaging of tissues. An explanation for the signal enhancement in microprobe MALDI imaging may also be related to suppression of surface charging, however other mechanisms cannot be excluded. Gold deposition on matrix crystals does not increase signal intensity or mass range in SIMS. The combination of ME-SIMS and MetA-SIMS is therefore not useful for tissue or single-cell analysis.

We have shown that surface modification by applying either a matrix (ME-SIMS), or a layer of metal (MetA-SIMS and stigmatic MALDI-MS) results in

enhanced intact molecule signals in imaging MS at the single cell and tissue level. Although the mechanism of signal enhancement by gold deposition is under debate, the results we have obtained for cells and tissue sections illustrate the potential of this sample preparation technique for biomolecular surface imaging by mass spectrometry.

Direct Molecular Imaging of *Lymnaea stagnalis* Nervous Tissue at Subcellular Spatial Resolution by Mass Spectrometry[**]

5

In the first part of this chapter the influence of the tissue microenvironment on the ionization efficiencies of different pseudomolecular ions of cholesterol, $[M-H]^+$, $[M-OH]^+$ and $[2M+Au]^+$ is described. High-resolution images of cholesterol were obtained from *Lymnaea stagnalis* nervous tissue using Metal-Assisted (MetA) Time-of-Flight Secondary Ion Mass Spectrometry (ToF-SIMS). The spatial distributions of these ions illustrate the influence of the biological matrix on the formation of specific pseudomolecular ions derived from the same molecular species.

In the second part the imaging capabilities of ToF-SIMS and MALDI-MS sample preparation methods were combined. We used this method, named matrix-enhanced (ME) SIMS, for direct molecular imaging of nervous tissue at micrometer spatial resolution. Cryosections of the cerebral ganglia of the fresh water snail *Lymnaea stagnalis* were placed on indium tin oxide coated conductive glass slides and covered with a thin layer of 2,5-dihydroxybenzoic acid, by electrospray deposition. High-resolution molecular ion maps of cholesterol and the neuropeptide APGWamide were constructed. APGWamide was predominantly localized in the cluster of neurons that regulate male copulation behavior of *Lymnaea*. ME-SIMS imaging allows direct molecule-specific imaging from tissue sections, without labelling and, opens a complementary mass window (<2500 Da) to MALDI imaging mass spectrometry, at an order of magnitude higher spatial resolution (<3 µm).

---

[*] A.F. Maarten Altelaar, Jan van Minnen, Connie R. Jiménez, Ron M.A. Heeren and Sander R. Piersma, *Anal. Chem.* **2005**, *77(3)*, 735-741.

[*] A.F. Maarten Altelaar, Jan van Minnen, Ron M.A. Heeren, and Sander R. Piersma, *Appl. Surf. Science,* **2006**, *252 (19)*, 6702-6705

5.1 Introduction

Mapping the dynamic state of the proteome inside a specific cell or tissue section is a challenging area in biological research. Standard molecular tissue (imaging) analyses are usually performed by immunocytochemistry[32,37,204] or fluorescence microscopy.[20,21,205,206] In these affinity-based methods a reporter molecule is linked to a target molecule using an antibody-antigen reaction, providing specific molecular information but limiting these techniques to known target molecules. Recently, imaging matrix-assisted laser desorption/ionization mass spectrometry (MALDI-MS) has been recognized as a tool for *in situ* proteomic analysis of (diseased) tissue.[9,24]

Imaging MS can spatially map surface components in tissue sections without pre-selection using the intrinsic property of molecular mass. The imaging MS approach for mapping protein and peptide distributions in mammalian tissues, developed in the group of Caprioli, has been seminal in the mass spectrometric community[60,207] and beyond.[25]

In imaging MS experiments, the ionization beam is rastered over the sample surface acquiring a data array of x,y-coordinates, with each position containing an entire mass spectrum. The current spatial resolution of MALDI microprobe imaging is in the 30-100 μm range[67,186], although development of new instrumentation with micrometer resolution has been reported.[145] With the current spatial resolution the technique is capable of mapping the molecular distribution at the tissue level but not at a cellular level, with most animal cells ranging from 5 - 50 μm in size.

Although secondary ion mass spectrometry (SIMS)[69] does not yield intact protein and peptide signals from cells and tissue sections, it does have several advantages compared to MALDI. The most important advantage of SIMS over MALDI is the chemical imaging capabilities routinely delivering submicron spatial resolution.[73] Furthermore, the SIMS technique is very sensitive and remarkably versatile since it can analyse almost any kind of solid surface.[104] Using SIMS, imaging at subcellular spatial resolution of elements, in dynamic SIMS,[75,78,79] and small organic components, in static SIMS, has been achieved.[74,86,148] The difference between the two regimes is the density of the primary ion beam at

the sample surface. In dynamic SIMS a primary ion dose of approximately 10^{16} ions per cm^{-2} is used, which results in the sample surface being eroded in time and most molecular species being completely fragmented. In static SIMS an ion dose $< 10^{13}$ ions per cm^{-2} is used and only the first monolayer of the surface is damaged.[72-74] Consequently, this lower primary ion dose in static SIMS results in reduced fragmentation and thus a higher yield of intact, low molecular weight organic molecules, as well as their fragments.

To enhance the yield of intact molecular species in SIMS, fragmentation by the primary ion beam during desorption ("sputtering" in SIMS terminology) has to be minimized. Several approaches have been reported, such as different kinds of sample surface coating (MALDI matrixes[26,102,149-151], silver[152,193] and gold[103,105,106,153,154]) and the use of polyatomic primary ion beams.[99,155-159] Metallization of (organic) samples with silver and gold has demonstrated to increase secondary ion yields of intact molecular ions in SIMS,[103,105,106,152-154] this technique is named Metal-Assisted (MetA) SIMS. Another way of modifying the bioorganic surface is deposition of a MALDI matrix. MALDI is capable of producing ions at significantly higher masses than SIMS. In MALDI the matrix absorbs most of the incident particle energy, thus preventing analyte fragmentation. Furthermore, fragmentation in the plume is reduced by collisional cooling with the matrix molecules.[101] MALDI sample preparation protocols combined with SIMS analysis, have previously shown to yield intact molecular ions for polymers, phospholipids, oligonucleotides and peptides, and proteins >10 kDa.[102,150,151,191] This technique is named matrix-enhanced (ME)-SIMS. In ME-SIMS standard MALDI matrixes are used, with 2,5-dihydroxy-benzoic acid (DHB) giving signal intensity enhancement for the widest range of molecular species.[102] One of the advantages of ME-SIMS is that it is both easy and cheap to implement. Standard SIMS instrumentation and MALDI sample preparations protocols can be used.

When using MALDI sample preparation protocols in imaging MS, the most important parameter is optimal incorporation of the analyte into the matrix crystals with minimal lateral diffusion. Problems arise when the well-known dried droplet (DD) method[58] is used for matrix deposition. Matrix droplets deposited on top of a cryo-microtome cut tissue section with the DD method spread over the surface and crystallize. This leads to very large matrix crystal sizes (tens of

micrometers) and lateral (x,y) analyte diffusion after wetting of the surface. The resulting non-uniform matrix coverage of the sample surface severely hampers the spatial resolution of the technique. These problems can be overcome when the matrix arrives at the tissue surface in very small droplets, forming matrix crystals in the order of or smaller than the minimal lateral resolution of the imaging mass spectrometer used. Matrix solutions can be sprayed into small droplets using pneumatic nebulization (airbrush)[172] or electrospray deposition (ESD)[174,190], the latter method giving smaller and more mono-disperse droplets. Several recent studies point to preferential ionization of lipid and sterol species in SIMS imaging of biological surfaces.[152,156,157,193] Imprinting tissue on silver coated surfaces, metallization of biological surfaces with silver or gold and the use of polyatomimetS99r1(y)4.9( )neams ma

~20.000 neurons that are clustered into a small number of major ganglia. Many of these neurons are peptidergic, of large size (50-150 μm) and easily identifiable from animal to animal.[213] Following the single-cell MALDI breakthrough, direct mass spectrometric analyses of invertebrate single neurons have provided a wealth of information about neuropeptides and their processing.[36,62] However, isolation of individual neurons is laborious, and only large, accessible neurons (such as the VD1 and the RPD2 neurons in *Lymnaea*[30,34,35]) can be sampled. In addition to mass spectrometric methods, neuropeptide distributions in nervous tissue of *Lymnaea stagnalis* have been characterized by means of molecular techniques[213], and immunocytochemistry.[37] Given the availability of both spatial as well as molecular information for *Lymnaea* neuropeptides, the brain of this mollusc represents an excellent model tissue for the development of high-resolution peptide imaging MS methodology. Mass spectrometric imaging at subcellular resolution can potentially map cell-specific neuropeptide distributions in tissue sections opening up a completely new analytical window.

5.2 Experimental section

Materials.
DHB, trifluoroacetic acid (TFA), acetonitrile (ACN), acetone and cholesterol were purchased from Sigma-Aldrich (Zwijndrecht, The Netherlands), HPLC grade water and methanol were purchased from Merck (Darmstadt, Germany). APGWamide was synthesized as reported previously.[37]

Tissue Sampling Protocol.
Freshwater snails (*Lymnaea stagnalis*) were raised under laboratory conditions; 20 ± 1 °C water temperature, 12 h light/12 h dark cycle and fed lettuce *ad libitum*.[32] Adult specimens were decapitated and the cerebral ganglia and connecting commissure were dissected, directly embedded in 10% gelatine (De Twee Torens, Delft, The Netherlands) at 30 °C and frozen at −80 °C. Gelatine embedding allows cryostat sectioning down to 5 μm thickness and does not

interfere with ME-SIMS analysis. 10 μm tissue sections were cut on a Leica CM 3000 cryostat (Leica Microsystems, Nussloch, Germany) at −20 °C. Sections were picked up on indium tin oxide (ITO, 4-8 Ω resistance) coated glass slides (Delta Technologies, Stillwater MN), dried in a stream of warm air for 1 minute and then quickly frozen on dry ice and stored at −80 °C. Conservation of morphology was checked by optical microscopy during the sectioning, drying and storage process. No obvious ice crystal damage was observed after freezing at −80 °C in gelatine. Light microscopy images were acquired using a Leica DMRX microscope with a Nikon DXM1200 digital camera. Prior to mass spectrometry, frozen tissue sections were brought to room temperature in a dessicator over a silica gel canister.

Extraction and Prepurification of Peptides.
The commissure was dissected under a microscope and directly transferred to an eppendorf reaction tube. The peptides were extracted by adding 30 μl of 0.1 M acetic acid after which the solution was boiled for 5 min and sonicated for 5 min. The solution was centrifuged for 5 min at 14000 RPM and the supernatant was purified using a C18 ZipTip (Millipore corporation, Bedford, MA). For MS analysis the extracts were spotted on a stainless steel target and diluted (1:1) with matrix solution (DHB in 50% aqueous ACN).

Electrospray Matrix Deposition.
For ESD a syringe pump (KD Scientific, New Hope PA) pumps matrix solution (15 mg/ml DHB in 50% MeOH/0.1% TFA (V/V)) from a gastight syringe (Hamilton Bonaduz, Switzerland) through a stainless steel electrospray capillary (o.d. 220 μm, i.d. 100 μm) maintained at 3-5 kV. The capillary is mounted on an electrically isolated manual translation stage (Thorlabs, Newton NJ) in a vertical orientation. The stage is fitted with a digital micrometer (Mitutoyo, Kawasaki, Japan) for accurate positioning of the needle tip with respect to the grounded sample plate. The sample plate is mounted on a x,y moveable table (Thorlabs, Newton NJ). Matrix deposition was performed by spraying for 10 min at a flow rate of 12 μl/h, a voltage of 4.7 kV and a needle to sample plate distance of 5.0 mm.

Gold deposition

Gold was sputter coated on the sample surface using a Quorum Technologies (Newhaven, East Sussex, U.K.) SC7640 sputter coater equipped with a FT7607 quartz crystal microbalance stage and a FT7690 film thickness monitor.

Mass Spectrometry.

All static SIMS experiments were performed on a Physical Electronics (Eden Prairie, MN) TRIFT-II time-of-flight (ToF) SIMS equipped with an $^{115}In^+$ liquid metal ion gun, as described before.

MALDI ToF MS spectra were acquired using a Bruker BIFLEX (Bruker-Franzen Analytik, Bremen, Germany) system equipped with a SCOUT ion source and a 337 nm nitrogen laser VLS-337i (Laser Science, Newton, MA). All analyses shown here were carried out in the reflectron mode with an acceleration voltage of 20 kV.

Scanning Electron Microscopy.

Measurements were performed on a FEI XL30 SFEG scanning electron microscope (SEM) (FEI company, Eindhoven, The Netherlands). The accelerator voltage of the system was 2-3 kV. Samples were coated with a thin carbon layer to improve the conductivity of the sample and so prevent charge accumulation.

5.3 Results and Discussion

Meta-SIMS

A MetA-SIMS spectrum of cholesterol spotted on a gold-coated (5 nm) silicon wafer, obtained with a 15 KeV ^{115}In primary ion beam, is shown in Figure 1A. The pseudo-molecular ion $[M-H]^+$ at *m/z* 385 and the dominant cholesterol fragment $[M-OH]^+$ at *m/z* 369 can be clearly seen. In addition to these high intensity cholesterol peaks also several gold cationized species can be observed with the most dominant peak at *m/z* 970, corresponding to the $[2M+Au]^+$ species. In Figure 1C and D the spectra of two imaging SIMS experiments of *Lymnaea stagnalis* nervous tissue are shown, measured with the same 15 KeV
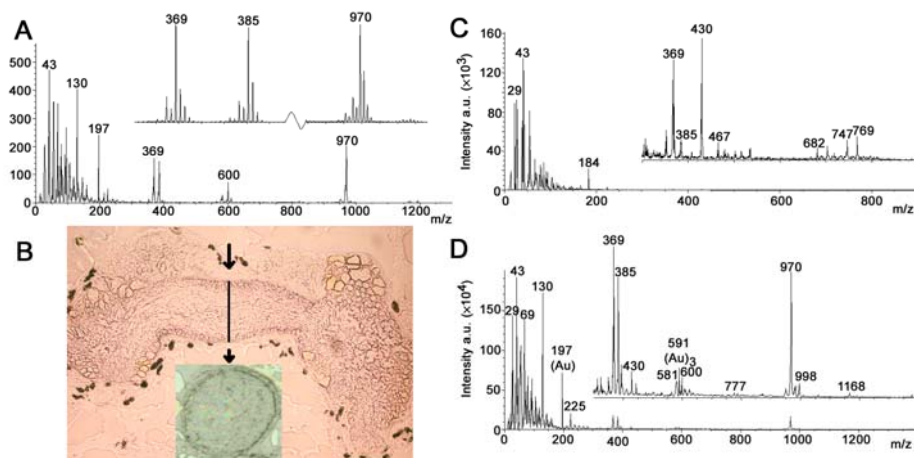
Figure 1. SIMS imaging of cholesterol and *Lymnaea stagnalis* nervous tissue with (A) MetA-SIMS spectrum of cholesterol spotted on a gold coated (5nm) silicon wafer (high mass range enhanced by factor of 2.5) (B) Optical microscopy image of *Lymnaea stagnalis* nervous tissue showing the left and right cerebral ganglia and the connecting commissure, inset shows cryomicrotome section of the commissure used in the MetA-SIMS analysis. (C) SIMS spectrum and (D) MetA-SIMS spectrum of *Lymnaea stagnalis* nervous tissue (high mass range enhanced by factor of 200 and 10 respectively).

[115]In primary ion beam. In Figure 1C the SIMS experiment was conducted directly on the *Lymnaea* tissue without any surface modifications. The spectrum shows several low mass fragments, the phosphocholine headgroup fragment at *m/z* 184 and several higher mass species. All of the species in the higher mass range are either lipids between *m/z* 700-800, lipid-derived species (diacylglycerols and ceramides) between *m/z* 500-700 or sterols, the cholesterol fragment at *m/z* 369 and vitamin E at *m/z* 430. In Figure 1D a similar *Lymnaea* nervous tissue section is examined by SIMS after the deposition of 1 nm of gold on top of the surface, using a sputter coater. It can be seen that the spectrum drastically changes, with a strong enhancement of the cholesterol signals, the appearance of several gold cationized cholesterol peaks and a decrease (or even disappearance) of the peaks from the lipids and lipid derived species. The enhancement for the dominant cholesterol fragment at *m/z* 369, after gold deposition is two orders of magnitude while the enhancement for the
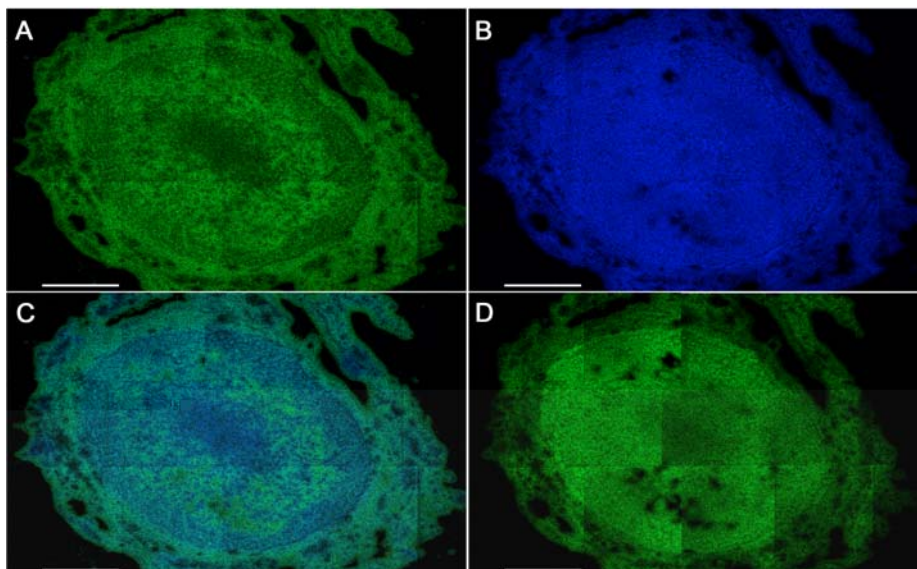
Figure 2. (A) MetA-SIMS image of cholesterol pseudomolecular ion [M-H]$^+$ distribution (*m/z* 385, green, 0-20 counts). (B) MetA-SIMS image of cholesterol fragment ion [M-OH]$^+$ distribution (*m/z* 369, blue, 0-16 counts). (C) Overlay image of cholesterol pseudomolecular ion [M-H]$^+$ (*m/z* 385, green, 0-20 counts) and cholesterol fragment ion [M-OH]$^+$ distributions (*m/z* 369, blue, 0-25 counts). (D) MetA-SIMS image of cholesterol pseudomolecular ion distribution [2M+Au]$^+$ (*m/z* 970, green, 0-5 counts). Scale bars are 100 μm.

pseudomolecular ion at *m/z* 385 is even slightly higher. Also, in the MetA SIMS tissue analysis the gold cationized species at *m/z* 970 is very dominant. Figure 1E-H shows the MetA-SIMS images of the *Lymnaea* nervous tissue sections after 1 nm gold deposition. The images were obtained from the commissure, connecting the two cerebral ganglia, cut in the axial plane using a cryomicrotome, as shown in Figure 1B. The Figures 1E and F show the spatial distribution of two cholesterol derived peaks, namely the [M-H]$^+$ peak at *m/z* 385 and the fragment peak at *m/z* 369. Although the two images depict the spatial distribution of the same molecule, they show remarkable differences, as can be seen in the overlay image of Figure 1G. Looking at the image of the *m/z*

369 signal of cholesterol, the highest abundance can be found at the border of the oval structure and in the centre. Conversely, the *m/z* 385 signal of cholesterol shows the highest intensity as an oval ring between the border and the center of the commissure tissue section. It is known from both optical microscopy and electron microscopy studies that the commissure consists of two morphological compartments, separated by a sheath of glial cells.[214] The neurohaemal area of the caudodorsal cells forms the outer compartment, while the inner compartment consists of thousands of axons. Furthermore, ventral caudodorsal cells send axons through the inner compartment.[214] Inspecting the images in Figure 1E and F and the overlay in Figure 1G, these inner and outer compartments as well as the separating sheath of glial cells can be clearly distinguished. The signal intensity of the *m/z* 385 signal is most intense at the glial cell area, separating the two compartments, while the *m/z* 369 peak shows the highest intensity at the inner compartment and increased signal intensity at the outer compartment. It is clear from these results that the microenvironment surrounding the molecule of interest plays a crucial role in its ionization. Taking either one of the cholesterol-specific peaks to illustrate its distribution would give a false image. Furthermore, quantitative statements on cholesterol concentrations in these highly heterogeneous biological surfaces will be prone to errors, since matrix effects on the ionization efficiencies have to be taken into account.

In Figure 1H we show the spatial distribution of the $[2M+Au]^+$ ion of cholesterol at *m/z* 970. The image shows a different distribution of the pseudomolecular ion than in Figures 1E and F. The image seems to be a convolution between the first two images, showing a decrease of signal intensity in the centre of the tissue and more or less homogeneous signal intensity through the rest of the tissue.

ME-SIMS
Figure 2 compar.3(o)-5TT2 18.6(h)-7.7(s)7.1(pe(ct)--2.7(r.3(o)(a)-4.5(of)-5.5(a cco)-53(mmFi)-4.7ssc)-6. e staignaia
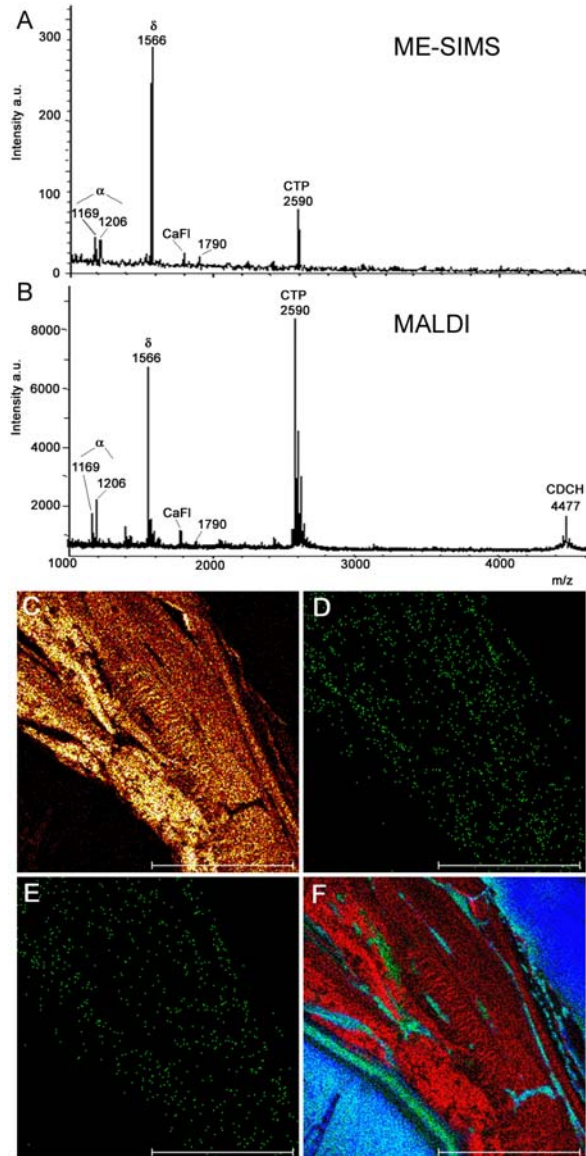
Figure 2. ME-SIMS vs. MALDI. (A) ME-SIMS and (B) MALDI spectrum of a commissure extract of the pond snail *Lymnaea stagnalis*. Both spectra were obtained using standard dried droplet sample preparation with DHB as matrix. The peptides identified are; α-caudorsal cell peptide (α, protonated and cationized), δ peptide (δ), HFFYGPYDVFQRD Vamide (*m/z* 1790), Calfluxin (CaFl), carboxyl terminal peptide (CTP) and caudodorsal cell hormone (CDCH). The ME-SIMS measurements used indium primary ions (total ion dose 8.9 × 10^{11} ions/cm^2) and the MALDI experiments 250 shots of the 4 ns 337 nm nitrogen laser.

(C-F) SIMS images of dried droplet sample preparation, with (C) DHB (154 *m/z*, 0-14 counts), (D) δ - peptide (1566 *m/z*, 0-2 counts), (E) CTP-peptide (2590 *m/z*, 0-2 counts) and (F) overlay of DHB (red, 0-14 counts), sodium (blue, 0-5 counts) and potassium (green, 0-10 counts). Scale bars are 100 µm.

precursor, which initiates egg laying in *Lymnaea*.[38] Peptides derived from the

CDCH precursor and present in both spectra are: αCDCP (protonated and cationized), δ peptide, Calfluxin (CaFl) and the carboxyl terminal peptide (CTP). In addition, the recently described HFFYGPYDVFQRDVamide (*m/z* 1790),[38] not encoded by the CDCH precursor, was detected as well. In the MALDI spectrum an additional mass can be seen at 4477 *m/z*, corresponding to the protonated CDCH precursor, not observed in the ME-SIMS spectrum. There are two principal factors why the higher mass peptide is not seen in the ME-SIMS spectrum. First, the desorption and ionization process of both techniques differ significantly, as explained in chapter 2 and reference 26. Second, given the lower mass range of conventional SIMS, the TRIFT has been optimized for low mass ions (< *m/z* 2500). The limited post acceleration (8 kV) results in reduced detection efficiency for larger molecules,[188] like the peptide at 4477 *m/z*. The ME-SIMS peptide analysis of a biological extract exemplifies the use of SIMS together with standard MALDI sample preparation protocols in the analysis of peptides with a molecular weight up to 2500 Da, at biologically relevant concentrations. Omitting the matrix yielded SIMS spectra with signals only ranging up to 200 Da and did not show any molecular signals. The imaging capabilities of the SIMS instrument allowed spatial analysis of the molecular distribution of the matrix and peptide molecules in the DD experiment (Figure 2 panels C-F). The matrix signal in Figure 2C shows a single crystal >150 μm in length and ~100 μm in width, formed using the DD method. The peptide signals (Figure 2D and E) are confined to the matrix crystals, while the cations are segregated (Figure 2F) as observed earlier.[150] These large matrix crystals are not an issue in MALDI imaging studies where the laser spot-size ranges between 20 and 50 μm.[67,186] Since the typical SIMS experimental spatial resolution is 1 μm,[73] these large crystals will interfere with the SIMS spatial analysis. So, not to compromise the obtainable spatial resolution in ME-SIMS, the matrix crystals must be 1 μm or smaller. Electrospray matrix deposition results in the required matrix crystal sizes (≤ 1 μm).

For the direct molecular imaging of *Lymnaea stagnalis* nervous tissue by ME-SIMS, 10 μm thick tissue sections were cut using a cryomicrotome. The tissue sections were covered with DHB as moderating matrix. Figure 3A shows an optical image of a tissue section of the central nervous system of *Lymnaea*; labeled regions are the left and right cerebral ganglia (Cg$_l$ and Cg$_r$), connecting
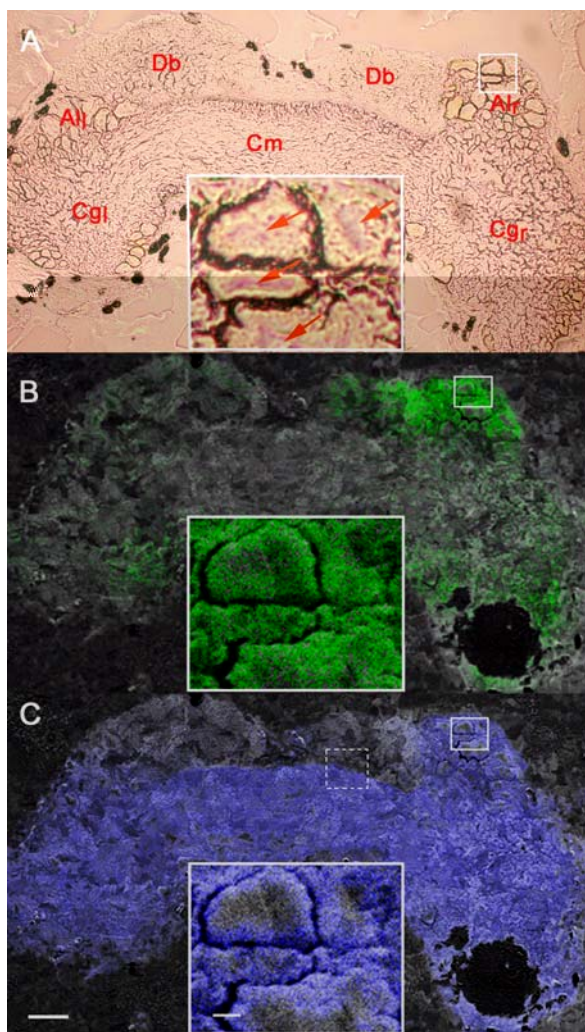
Figure 3. Direct molecular imaging of *Lymnaea stagnalis* nervous tissue by ME-SIMS. (A) Optical image of the *Lymnaea* cerebral ganglia, inset shows high magnification image of neurons in the anterior lobe (solid box), arrows indicate nuclei. Different regions in the section are: right and left cerebral ganglia (Cg_r and Cg_l), anterior lobe (Al), commissure (Cm) and dorsal bodies (Db). (B) ME-SIMS image of APGWamide (429.0-433.2 *m/z*; green, 0-3 counts) distribution. (C) ME-SIMS image of cholesterol (368.2-371.3 *m/z*; blue, 0-4 counts) distribution. Scale bar: 200 μm, scale bar inset: 10 μm. Molecular images (B & C) are presented as coloured overlays on top of the grey-scale TIC (total ion count) image (mass range: 1.0-5000 *m/z*, 0-140 counts). The ME-SIMS measurements used indium primary ions (total ion dose 4.9×10^{11} ions/cm^2).

commissure (Cm), the dorsal bodies (Db) and the left and right anterior lobe (Al_l and AL_r). In the inset of Figure 3A a high magnification image of the anterior lobe is presented (boxed area), clearly showing the large neurons and their nuclei, indicated by the red arrows. Approximately 120-150 neurons are present

in the right anterior lobe, playing a central role in the reproduction of *Lymnaea*.[32,33,37]

ME-SIMS spectra of *Lymnaea* nervous tissue, after ESD, show cholesterol signals at 386 *m/z* (M)[+] and the dominant fragment ion at 369 *m/z* (M-OH)[+], a signal at 430 *m/z* and lower abundance masses in the range of 500-1000 *m/z* (Figure 4). The 430 *m/z* signal is assigned to the neuropeptide APGWamide, previously structurally characterized by single-cell MALDI MS/MS[36] and localized by immunocytochemistry.[37] The assignment of the peak is based on both mass and localization. A different species closely related in mass (i.e. vitamin E) is also observed in SIMS analysis but does not give such distinct localization patterns as shown in these measurements.

APGWamide plays a key role in the regulation of the male reproductive activity of *Lymnaea*. cDNA studies have shown that from every precursor protein 10 copies of APGWamide are synthesized, together with single copies of several other peptides.[33,36,215] In addition to the low *m/z* ions (<130 *m/z*) and the matrix ions (154 and 137 *m/z*), the cholesterol and the APGWamide signal were intense enough for ME-SIMS imaging.

The sampled area in one ToF-SIMS experiment was 150 × 150 μm. To image a larger section, the sample stage was stepped in a mosaic pattern and the resulting images were aligned to produce a single molecular image. To cover the entire tissue section 77 SIMS experiments of three minutes per experiment were conducted. In Figure 3B and C, mass spectral images of the same tissue section as in Figure 3A are shown after matrix deposition, ME-SIMS data acquisition, and processing. The total ion count (TIC) images are presented in greyscale and overlaid with the molecular images of APGWamide (green) and cholesterol (blue). ME-SIMS images of *Lymnaea* nervous tissue show that APGWamide is predominantly localized in the right anterior lobe (Figure 3B). In addition to the strong APGWamide signal in the right anterior lobe, less abundant localization can be found in de left anterior lobe and the left and right cerebral ganglion, which is in agreement with immunocytochemistry results.[37] Non-homogeneous subcellular APGWamide distributions were observed for the large neurons in the anterior lobe (Figure 3B inset). The higher cytosolic neuropeptide signals contrast with the central darker part of the cell corresponding to the nucleus.

Indeed precursor and active peptides are packaged in cytosolically localized, secretory vesicles,[216] in line with the ME-SIMS data.

Cholesterol signals are found in comparable intensity on the entire tissue section except for the dorsal bodies, non-nervous neuroendocrine organs located at the dorsal surface of the cerebral ganglia[217], where signal intensity is decreased (Figure 3C). The origin for the difference in cholesterol signal intensity in the ME-SIMS image is unclear. In the optical image (Figure 3A) can be seen that the tissue morphology of the dorsal bodies differs from the rest of the section. The highest cholesterol signal is obtained at the cellular plasma membrane but not at the nuclear membrane (Figure 3C inset), in line with recent observations on cholesterol localization.[193,218-220] These results illustrate the subcellular imaging capabilities of the ME-SIMS technique. In the TIC image the cellular outlines can be observed readily, especially for large neurons (see insets Figure 3). The TIC image contains in each pixel the sum of all ions (elements, low-mass-fragment ions and molecular ions) arriving at the detector for a given location on the tissue. Although molecular information is not obtained in the TIC images, morphological detail is comparable with conventional light microscopy, allowing the alignment of 77 individual images of 150 × 150 µm into a mosaic pattern. The overlay of TIC and molecular images thus combines both morphological and molecular information. Cholesterol and APGWamide ME-SIMS signals are confined to the tissue section. This indicates that neither the tissue-sampling protocol nor the electrospray-matrix-deposition method give rise to extensive peptide redistribution over the surface at the micrometer scale, corroborating the observations of Kruse *et al*.[186] The images in Figure 3B and C show a circular hole in the lower right cerebral ganglion where, due to an electrospray artifact, no matrix was deposited. The clear boundary of the circular hole shows that migration of analyte doped matrix crystals on top of a tissue section does not occur. Furthermore, in the absence of matrix (the hole) the molecular ion signals, seen in the area with matrix, were absent. ToF-SIMS imaging experiments of *Lymnaea* nervous tissue sections without the application of a moderating matrix gave very few high mass signals except for *m/z* 184 (Figure 4A). The signal at *m/z* 184 is attributed to phosphocholine, the polar headgroup of the lipids phosphatidylcholine (PC) and sphingomyelin (SM),[221,222] the two major constituents of the lipid bilayer in the brain. This result is in agreement

105
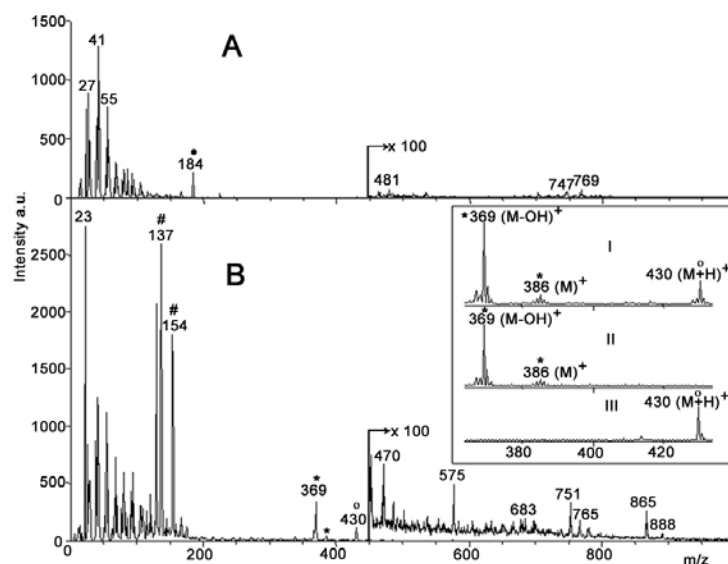
Figure 4. ToF-SIMS spectra of the *Lymnaea* nervous tissue before (A) and after (B) ESD matrix deposition. Marked peaks are: DHB (M)$^+$ at 154 *m/z* and (M-OH)$^+$ at 137 *m/z* (#), phosphocholine fragment ion at 184 *m/z* (●), cholesterol (M)$^+$ at 386 *m/z* and (M-OH)$^+$ at 369 *m/z* (*), and APGWamide (M+H)$^+$ at 430 *m/z* (○). Inset shows (I) zoomed area of spectrum B and ME-SIMS spectra of (II) synthetic cholesterol and (III) synthetic APGWamide.

with earlier SIMS studies, where the phosphocholine headgroup was used for imaging of the PC distribution.[73,91,223] Matrix addition does complicate the SIMS imaging analysis since it modifies the tissue surface. A comparison of the DD and the ESD method by SIMS revealed a highly non-uniform distribution of the matrix over the surface in the DD sample. Furthermore, the sample consisted of regions with abundant peptide signal next to regions where no peptide signal was detected, although matrix molecules were present. The SIMS images obtained after ESD however, showed a uniform distribution of the same selected ions. These results are in agreement with previous studies where it has been shown that in the DD method highly non-uniform matrix crystals are formed.[150,175,191] These local matrix crystal variations will result in
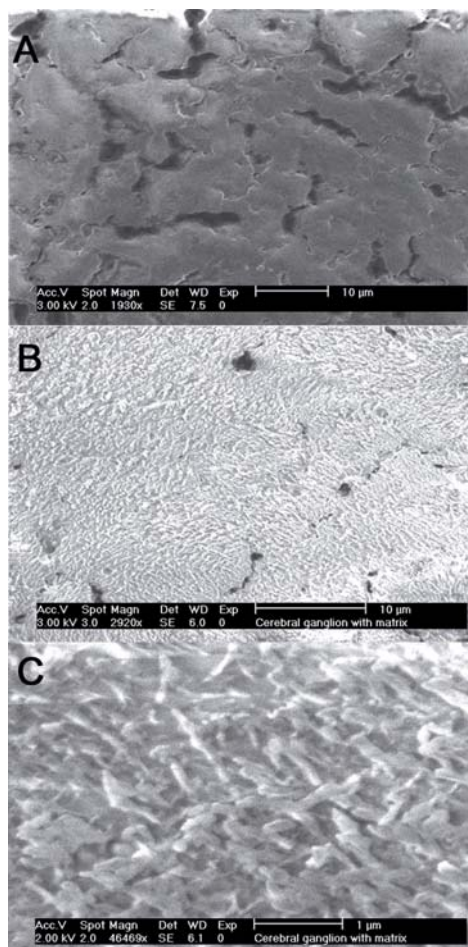
Figure 5. Scanning electron microscopy images of *Lymnaea stagnalis* nervous tissue (A) prior to matrix application (scale bar 10 µm) and (B) after ESD of DHB (scale bar 10 µm). (C) Higher magnification image showing sub-micron crystal dimensions after ESD (length ~0.5-1 µm, width ~0.2-0.4 µm) (scale bar 1 µm).

unrepresentative images of the molecular distribution in a tissue, when using the DD method in combination with the high spatial resolution of imaging ToF-SIMS. Figure 5 shows scanning electron microscopy (SEM) images of the surface of *Lymnaea* nervous tissue before (5A) and after (5B and C) ESD. The SEM images clearly show that homogeneously distributed, sub-micron sized (length ~0.5-1 µm, width ~0.2-0.4 µm) crystals are formed (Figure 5C). For

comparison, the heterogeneously distributed matrix crystals formed on-tissue from the dried droplet method appeared in sizes exceeding 20 µm (data not shown).
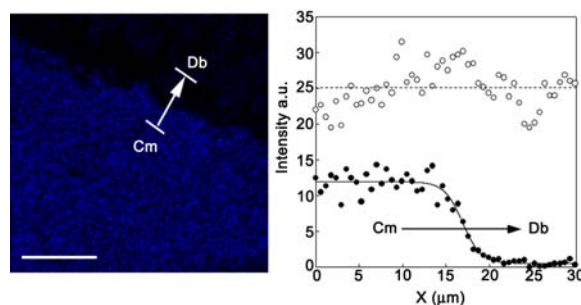
Figure 6. Experimental resolution of direct tissue ME-SIMS. (A) Cholesterol distribution (blue) in the commissure (Cm) and dorsal body (Db) area (dashed box in Figure 3C). Scale bar: 50 µm. The arrow indicates a line scan orthogonal to the commissure - dorsal body transition (length 30 µm, width 3.5 µm). (B) Cholesterol (●) and DHB intensity data (○) of the same line scan.

The resolving power of molecular imaging of biological tissues by ME-SIMS is a convolution of the SIMS instrument spatial resolution (primary ion beam focus) and the tissue sampling/matrix deposition protocol. To determine the resolving power of the ME-SIMS imaging method, the sharp decrease in cholesterol (*m/z* 369) signal intensity going from the commissure to the dorsal bodies is examined. A (30 µm) line scan was taken (Figure 6) and the resolving power was defined by taking the length Δx required to go from 80% to 20% cholesterol signal intensity.[148] Cholesterol intensity data (●) along the line were fitted with a sigmoidal function $I = I_0 + \dfrac{a}{1 + e^{(\frac{x-x_0}{b})}}$ (solid line) defining the length Δx. Fitted values are: I_0 = 0.56±0.28 counts, a = 11.41±0.37 counts, b = −1.06±0.19 µm and x_0 = 16.90±0.22 µm with R=0.979. A lateral resolving power (Δx) of 2.9 µm was calculated (with I-I_0 = 100%). For comparison, the

DHB signal (O) along the same linescan showed homogeneous coating of the tissue section surface by the matrix.

If extensive analyte diffusion/redistribution would occur due to cryostat sectioning, drying or surface wetting during ESD, then this should result in decreased resolution. The calculated resolving power of 2.9 µm, a factor ~3 lower than the SIMS experimental resolution (1 µm), indicates that the tissue sampling and matrix deposition protocol does not excessively compromise the spatial resolution in ME-SIMS.

5.4 Conclusions

We have shown that direct molecular imaging of nervous tissue at subcellular resolution is feasible by using matrix-enhanced SIMS. Electrospray matrix deposition preserves the spatial distribution of surface analytes in tissue sections and allows peptide ionization using SIMS.

ME-SIMS localized the peptide APGWamide in the anterior lobe of the right Cg, consistent with immunocytochemical data. The spatial resolution of peptide imaging by ME-SIMS is about one order of magnitude better than that of microprobe mode imaging MALDI.

High-Resolution MALDI Imaging Mass Spectrometry allows Localization of Peptide Distributionsat Cellular Length Scales in Pituitary Tissue Sections[*]

6

MALDI imaging mass spectrometry (IMS) has been used to determine peptide distributions directly from rat, mouse and human pituitary tissue sections. Since these organs are small (10^2-10^3 μm) the spatial resolution of IMS is a key issue in molecular imaging of pituitary tissue sections. Here we show that high-resolution IMS allows localization of neuropeptide distributions within different cell clusters of a single organ of a pituitary tissue section. The sample preparation protocol does not result in analyte redistribution and is therefore applicable to IMS experiments at cellular length scales. The stigmatic imaging mass spectrometer used in this study produces selected ion count images with pixel sizes of 500 nm and a resolving power of 4 μm, yielding superior spatial detail compared to images obtained in microprobe imaging experiments. Furthermore, we show that with imaging mass spectrometry a distinction can be made between different mammalian tissue sections based on differences in the amino acid sequence of neuropeptides with the same function. This example demonstrates the power of IMS for label-free molecular imaging at relevant biological length scales.

6.1 Introduction

Imaging mass spectrometry (IMS) has proven to be a powerful tool in the investigation of molecular distributions in both healthy and diseased tissue.[25,65,67,141,143,144] Matrix assisted laser desorption/ionization (MALDI) MS has shown to produce peptide and protein signals directly from tissue sections.[25,141,143,210] As in any imaging technique the obtainable spatial resolution is a key issue. Our current aim is to obtain cellular resolution, without compromising the original spatial distributions of the molecules of interest. In IMS, both instrumentation and sample preparation issues have limited the spatial resolution. In conventional microprobe MALDI-IMS the obtainable spatial resolution is determined by a combination of the laser spotsize and the sample preparation technique. Typically, the laser spotsize in MALDI-IMS ranges from ~50 to 200 μm. The spatial resolution of MALDI imaging has been increased by developing optical lenses, able to focus the laser to submicron dimensions.[145] However, it has been shown that the sensitivity of MALDI for high mass molecules decreases significantly with decreasing spot size (two orders of magnitude for spot sizes of ≈7 μm diameter).[224]

Recently, a new approach to MALDI imaging has been developed in our group: the stigmatic mass microscope.[127,141] In this instrument the obtainable spatial resolution is independent from the size of the desorption/ionization area. The desorbed ions within a large laser spot (150 × 200 μm) retain their original spatial distribution during Time-of-Flight (ToF) separation and are detected by a position sensitive detector. The resulting stigmatic images at highest magnification have a pixel size of 500 nm and a resolving power of 4 μm, both for UV and IR lasers.[127,147] With the mass microscope we approach the spatial resolution obtained by secondary ion mass spectrometry (SIMS) but with the ability to desorb large organic molecules like peptides and proteins. In addition, this high spatial resolution is obtained with much higher speed of analysis.[127]

In order to benefit from this high spatial resolution, the preparation of the tissue sections before MALDI analysis is of crucial importance. The goal is to obtain sufficient peptide and protein signal intensity from matrix crystals smaller than the tissue features of interest and without redistribution of the analyte

molecules. One method of improving signal intensity is washing of the tissue sections. If no washing step is performed before addition of the MALDI matrix, the physiological saline hampers the crystallization of the MALDI matrix. When a washing step is performed the crystallization of the matrix on the tissue results in more uniform and smaller sized crystals, but diffusion of the molecular content has to be limited as much as possible. The addition of the matrix itself can also determine the maximum obtainable spatial resolution. If the matrix is added in droplets as in piezodispensing or in acoustic deposition,[135] the size of the droplets, and thus the maximum obtainable spatial resolution, is in the order of 150-250 μm. Other approaches to matrix deposition like electrospray or pressure driven deposition result in much smaller matrix crystals (~0.5-1 μm, 1-10 μm respectively), but smaller crystals can compromise sensitivity in MALDI-MS.

The tissue size and the morphological length scales will ultimately determine the spatial resolution needed in IMS. The first direct MALDI-MS analysis of peptides from dissected cells was already performed over a decade ago,[34,35] followed by the first example of profiling of peptides in rat pituitary tissue, by Caprioli *et al*.[60] in 1997.

The pituitary gland is a small organ at the base of the brain, connected to the hypothalamus. The pituitary is part of the endocrine signaling system and secretes hormones into the circulatory system. The primary function of the pituitary gland is regulation of the endocrine system itself by controlling the function of the other glands in the endocrine system. The action of the pituitary is regulated by signals coming from the hypothalamus. In endocrine signaling a high concentration of hormones (e.g. neuropeptides) are secreted in a burst-like manner. The high neuropeptide content in the pituitary gland makes the organ an excellent model for analysis with IMS.

The pituitary is made up out of two different regions called the adenohypophysis (or anterior and intermediate lobe) and the neurohypophysis (or posterior lobe).[225] The cells of the anterior lobe synthesize and secrete at least seven peptide hormones associated with growth, development, metabolism, and sexual function. The intermediate lobe synthesizes and releases specific peptide products from the pro-opiomelanocortin (POMC) precursor protein, among which the well characterized α-melanocyte stimulating hormone (MSH). The posterior

pituitary does not synthesize but only stores and secretes the peptides vasopressin and oxytocin, derived from the ProVP and ProOX precursors respectively. These peptides are synthesized in the paraventricular and supraoptic nuclei of the hypothalamus and subsequently transported and stored in the posterior lobe.[45,225,226] We recently showed the localization of the peptide vasopressin in the hypothalamic area using imaging MS.[141]

Here we use imaging MALDI-MS to study the peptide distributions in pituitary tissue of rat, mouse and human. We show that both improved instrumentation and sample preparation protocols allow mapping of neuropeptide distributions at high spatial resolution, showing features at cellular length scales.

6.2 Experimental section

Materials

α-cyano-4-hydroxycinnamic acid (HCCA), 2,5-dihydroxybenzoic acid (DHB) trifluoracetic acid (TFA) and HPLC grade water were purchased from Sigma-Aldrich (Zwijndrecht, The Netherlands). Ethanol was purchased from Biosolve (Valkenswaard, The Netherlands).

Tissue sections
Rat:
Experimental procedures were in accordance with the European directives (86/609/EEC) and approved by the Commission on Laboratory Animal Experiments of the University Medical Centre Utrecht. Male Wistar rats (Crl:WU) weighing 350 g were obtained from Charleltlrthrma.5(c)-ny(nds5( )]TJ8/TT2 139(n0.406652 TD0 Tc0

seMah,enamlen- tined3-opurcEs-

Human:

Normal pituitary glands were obtained at autopsy from individuals who had died of unrelated causes, and whose pituitary glands showed normal growth features. The tissue was snap frozen in liquid nitrogen and stored at -70 °C.

10 µm thick pituitary tissue sections were cut from all species using a cryomicrotome at −17 °C. Sections were thaw-mounted on ITO-coated glass slides and were stored at −80 °C until use. Prior to mass spectrometry, tissue sections were brought to room temperature in a desiccator over a silica gel canister (1 hr).

Sample preparation

After drying, both rat and human pituitary tissue sections were washed twice for 1 minute in ice-cold 70% ethanol and dried at room temperature.[172] Mouse pituitary tissue sections were not washed before matrix deposition. In the case of the human pituitary tissue sections, adjunct sections were Haematoxylin and Eosin (H&E) stained to check and compare morphological features. A TLC sprayer (Sigma-Aldrich, Zwijndrecht, The Netherlands) was used to spray the matrix solution, 10 mg/ml HCCA or 40 mg/ml DHB in 50 % EtOH / 0.1 % TFA, for MALDI MS. The nitrogen pressure required for efficient nebulisation was 0.3-0.4 bar. Gold was sputter coated on the sample surface using a Quorum Technologies (Newhaven, East Sussex, U.K.) SC7640 sputter coater equipped with a FT7607 quartz crystal microbalance stage and a FT7690 film thickness monitor.

Imaging Mass Spectrometry

MALDI stigmatic imaging MS was performed on an extensively modified Physical Electronics (Eden Prairie, MN) TRIFT-II (triple focusing time-of-flight) mass spectrometer equipped with a phosphor screen/CCD camera optical detection combination as described in detail by Luxembourg *et al*.[127] The ion optics of this mass spectrometric microscope have been designed such that a magnified (ion-optical) image of the surface is mapped onto a two-dimensional detector.[130] In short, a custom-designed interface was constructed that controls the size, position and homogeneity of the UV laser spot. It consists of an ultrahigh vacuum compatible microscope objective (LMU-5X-NUV, Optics For Research)

with a focal length of 40 mm. This is mounted on a telescopic and maneuverable UHV flange for use with a wedge, diode pumped solid-state Nd-YAG laser source, at 355 nm wavelength and 2 ns pulse duration (BrightSolutions, Italy). The desorbed ions are extracted through a 3.2 keV electric field into the ToF analyzer and post-accelerated by an additional 9 kV prior to detection on a 1-in.-diameter dual microchannel plate (DMCP) phosphor screen detector assembly (APD 30 25 12/10/12 PS I EDR 60:1 P-20 MgO-coated, Burle Industries GmbH, Baesweiler, Germany) located in the instrument's final image plane. Mass spectra are obtained from the MCP detector after which ion images are formed on the phosphor screen and projected onto a CCD camera with 9.9-µm pixel size (Imager 3, La Vision, Goettingen, Germany) by a zoom lens (Thales Optem, Fairport, NY) that reduces the image size to fit the CCD chip. High-speed ion blankers are used to control which ions reach the detector. The total magnification obtained in the MALDI-ion microscope is determined by an ion-optical and a light-optical component. Depending on the settings of the instrument, images were recorded with 10× or 20× overall magnification, resulting in images pixel sizes of 1 µm and 500 nm respectively.

Single-shot 200 µm total-ion-count (TIC) MALDI stigmatic images were acquired and stored as tagged image file format (tiff) files with the corresponding synchronized ADC signals (Acqiris, Geneva, Switzerland). To image an entire pituitary tissue section individual linescans were acquired by moving the sample stage at 100 µm/s while continuously firing the laser with a repetition rate of 10 Hz. At the end of the linescan (i.e. tissue section) the stage was stepped in the y direction by 80, 100 or 120 µm increments. This process was repeated as many times as required to image the entire tissue section.

Mass Spectrometry

Electrospray-MS was performed on a quadrupole ToF Q-ToF 2 instrument (Micromass, Manchester, UK) coupled on-line with a capillary HPLC (CapLC) (Waters, Milford, MA, USA). Peptides were separated on a capillary C18 reversed-phase column (75 µm ID, 15 cm) (LC Packings, Amsterdam, The Netherlands) using a 5–60% acetonitrile gradient in 0.1% formic acid (80 min; 200 nL/min). The column was connected to a metal-coated fused-silica electrospray needle (tip ID, 10 µm) (NewObjective, Woburn, MA, USA).

FTICR-MS experiments were performed on a 7 T Bruker Daltonics Apex III equipped with a nitrogen laser (337 nm). At each position, the ions generated from 10 laser shots were accumulated in an external hexapole ion trap and then transferred to the ICR cell for detection or tandem mass spectrometry.

MALDI data processing
Software was developed in-house to align all overlapping single shot images into a line-scan, and subsequently all line-scans into an image. This high resolution TIC image (pixel size 500 nm, resolving power ~4 µm) was overlaid with the course resolution ADC data at each position. For comparison purposes the ADC image data was digitally resampled at different pixel sizes and treated like regular microprobe data.

6.3 Results and Discussion

High resolution IMS
Figure 1 shows a schematic representation of the different protocols used to obtain high-resolution MS images. In stigmatic imaging the obtainable spatial resolution is not dependent on the size of the laser spot but depends on the quality of the ion-optics. After irradiation by the 150×200 µm homogeneous laser pulse the desorbed ions pass an immersion lens/transfer lens combination followed by a high-speed blanker. Subsequently time-of-flight separation takes place. Three semi-hemispherical electrostatic analyzers (ESA) are integral part of the 2m-flight path and are responsible for up to 200 eV kinetic energy compensation. After the third ESA the ions pass a second high-speed blanker which, in combination with the first high-speed blanker, can be used for selected ion imaging. All ions desorbed from the tissue surface preserve their original spatial distribution during time-of-flight separation and are depicted at a position sensitive detector. This allows the simultaneous recording of a microscope and microprobe dataset is a single experiment.
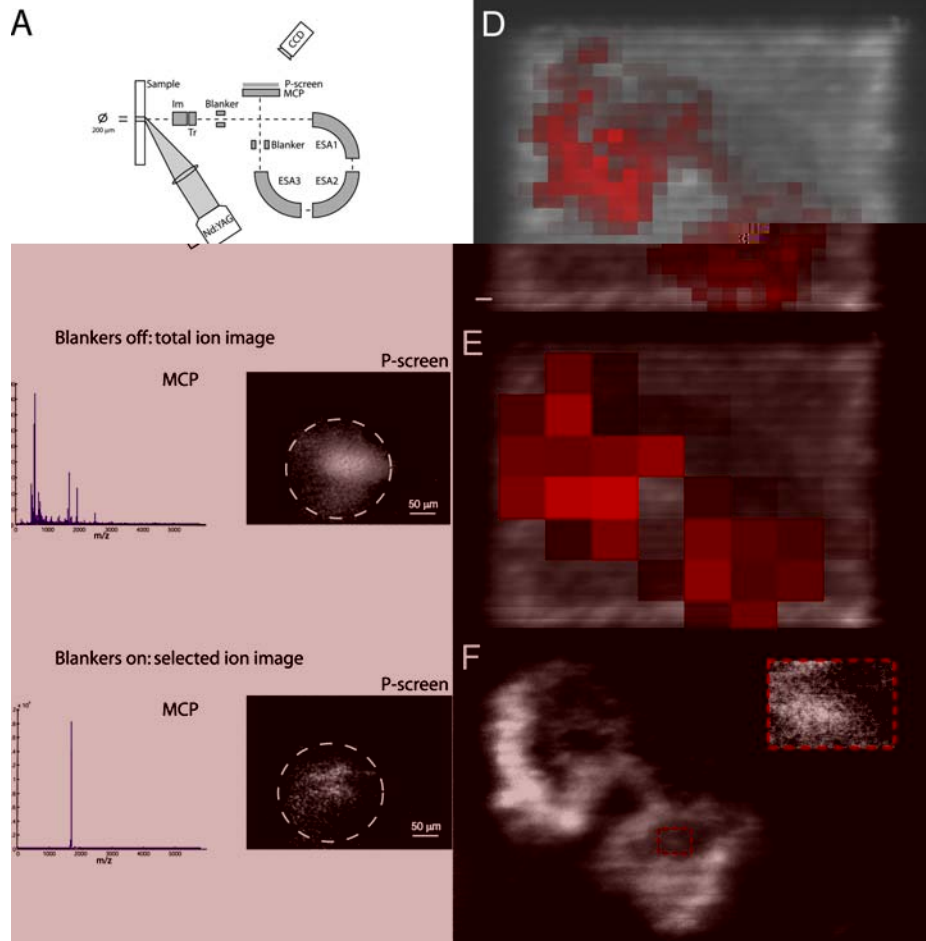
Figure 1. Instrumentation of the stigmatic mass microscope and a comparison with microprobe IMS. (A) Schematic representation of the Physical Electronics Trift II mass spectrometer (B) TIC and (C) stigmatic single ion imaging. The distribution of the neuropeptide α-MSH (diacetylated) in microprobe imaging, depicted with a resampled pixel size of (D) 80×80 μm (red) and (E) 250×250 μm (red) and overlaid on the stigmatic TIC image, is compared to (F) the stigmatic ion image of diacetylated-α-MSH, with in the inset an enlarged area of the ion distribution. Scale bar is 100 μm.

The position sensitive detector consists of a CCD camera phosphor screen assembly, where snapshots of the ions reaching the phosphor screen are taken (Fig. 1A). These snapshots are used to construct the stigmatic ion images while at the same time the acquired m/z data can be used to construct course resolution microprobe ion images. In order to construct whole tissue images a linescan is taken over the entire tissue section, by moving the sample stage at a constant speed (typically 100 µm/s) under a continuously firing laser. At the end of a linescan the sample stage is moved upwards by 40-60% of the laser spotsize and another linescan is taken, until the entire tissue section is measured. With in-house developed software the stigmatic ion images are stitched together to form a linescan. These individual linescans are then combined to form the TIC image of the entire tissue section (Fig. 1B). The in-house developed software calculates the overlap of the consecutive laser shots and adds the intensity data of the overlapping areas in the images. As can be seen in Figure 1C, the TRIFT high-speed blankers can be used to record stigmatic selected ion images. In this case the high-speed blankers are used to remove all ions except the ones passing through a ~3 µs time window, which is set manually. In the mass spectrum a single isolated peak can be seen at the selected m/z position. Since only this single ion reaches the position sensitive detector, high spatial resolution mass resolved SIC images can be created.

Figures 1D-F, show the localization of the neuropeptide α-MSH in mouse pituitary tissue. The images in Figure 1D and E show a microscope mode TIC image (grey) in the background overlaid with microprobe mode selected-ion-count (SIC) image constructed from the MCP m/z data of diacetylated (diAc) α-MSH (red). In order to record the TIC image of the entire tissue section, 25 individual linescans were acquired with intervals of 80 µm, resulting in 10×80 µm pixels. To compare the obtainable spatial resolution in the conventional microprobe mode versus the microscope mode Figure 1D and E are depicted with a digitally resampled 80×80 µm (Figure 1D) and 250×250 µm (Figure 1E) spatial resolution, the latter one representing the spatial resolution used in recent MALDI imaging literature.[65] In this figure it can be clearly seen that the spatial resolution obtained with the conventional approach is too low to be able to localize neuropeptides within tissue features at cellular length scales. Figure 1E shows a selected ion microscope mode image of the same tissue section.

Here, the distribution of the diAc-α-MSH ion is imaged, blanking all other ions desorbed, as can be seen in the corresponding mass spectrum in Figure 1C. The diAc-α-MSH ions pass through the ToF mass spectrometer and form an ion-optical image at the position sensitive detector, comparable to wide field optical microcopy. Since the diAc-α-MSH ions original spatial orientation at the surface of the tissue is not disturbed during ToF analysis the image depicted at the position sensitive detector is a true reflection of this spatial orientation, showing spatial detail from within the laserspot. In this manner molecular images can be obtained with pixel sizes of 500 nm and a spatial resolving power of 4 µm. The comparison of this image with the ones in Figure 1D and E, demonstrates that the microscope mode approach delivers superior spatial detail.

Sample preparation
The precise localization of neuropeptides in pituitary tissue sections by IMS requires a robust sample preparation technique. To perform direct tissue MALDI-IMS, multiple approaches can be utilized. First there is the choice whether to wash the tissue sections. If no washing step is performed the physiological conditions of the tissue hamper the crystallization of the MALDI matrix. In this case DHB is used as matrix because of its tolerance to high salt loads. Washing the sample results in uniform crystallization of the matrix on top of the tissue, irrespective of the chosen matrix, but holds the possibility of diffusion or washing out of the molecules of interest. After washing HCCA can be added as matrix in several spray cycles, which result in much smaller crystal sizes than DHB. Because of these small matrix crystals this technique is better suited for high spatial resolution imaging. In order to prevent diffusion of the peptides as much as possible the tissue sections are immersed in 70% ice-cold ethanol, while producing a minimal amount of movement of the solvent. The tissue sections are left in this first solution for 1 minute without further movement and than transferred to the second 70% ice-cold ethanol solution for the second wash step, taking the same precautions. In the study of the mouse pituitary sections no washing step was performed and concentrated DHB solution (40 mg/ml) was sprayed directly on the tissue surface. The DHB matrix still crystallizes on the tissue surface but distinct differences between the crystals on and adjacent to the tissue surface can be seen. The crystals formed adjacent to

the tissue are much more translucent, spiked and differ a lot in size while the crystals on the surface of the tissue are dark and much more homogenous rectangular. This is caused by the salt, which is incorporated in the matrix crystals on the tissue surface.[150] Still, the unwashed tissue resulted in a rich MALDI spectrum after covering with the DHB matrix. After drying of the tissue sections, 5 nm of gold is deposited on top of the matrix crystals in order to prevent charging of the surface. Prevention of surface charging helps the analysis in two ways, one: because of the increased signal intensities observed, and two: it prevents blurring of the stigmatic images. Charging of the surface causes blurring of the stigmatic ion optical images, since the ion-optics are sensitive to small changes in the sample potential.

Neuropeptide localization

Figure 2 shows the summed mass spectra of rat (2A), mouse (2B) and human (2C) pituitary tissue sections from IMS experiments. The spectra show a rich signature containing several peptides derived from the POMC precursor protein along with vasopressin at m/z 1084 and oxytocin at m/z 1028 (sodiated), derived from the ProVP and ProOX precursors, respectively. One of the POMC peptides, α-MSH is present in different degrees of acetylation (table 1), with the most abundant form being diacetylated α-MSH in the spectra from mouse and rat. It is known from literature that the degree of acetylation plays a role in the potency of the neuropeptide.[227,228] Other POMC peptides seen in the spectra are the joining (J) peptide and Corticotropin-like intermediary peptide (CLIP) and a CLIP fragment, POMC potential peptide and β-endorphin. The mass spectra of the three pituitary tissue sections show clear differences from each other. In the mass spectrum of the mouse pituitary the vasopressin signal is absent, which can be explained by the absence of the neurohypophysis in the mouse pituitary tissue section. More importantly, the abundant J-peptide peak is not present in the mass spectrum of the human pituitary tissue, since this peptide is absent in the human POMC sequence. The POMC amino acid sequences in mouse, rat and human differ from each other by multiple amino acid substitutions.
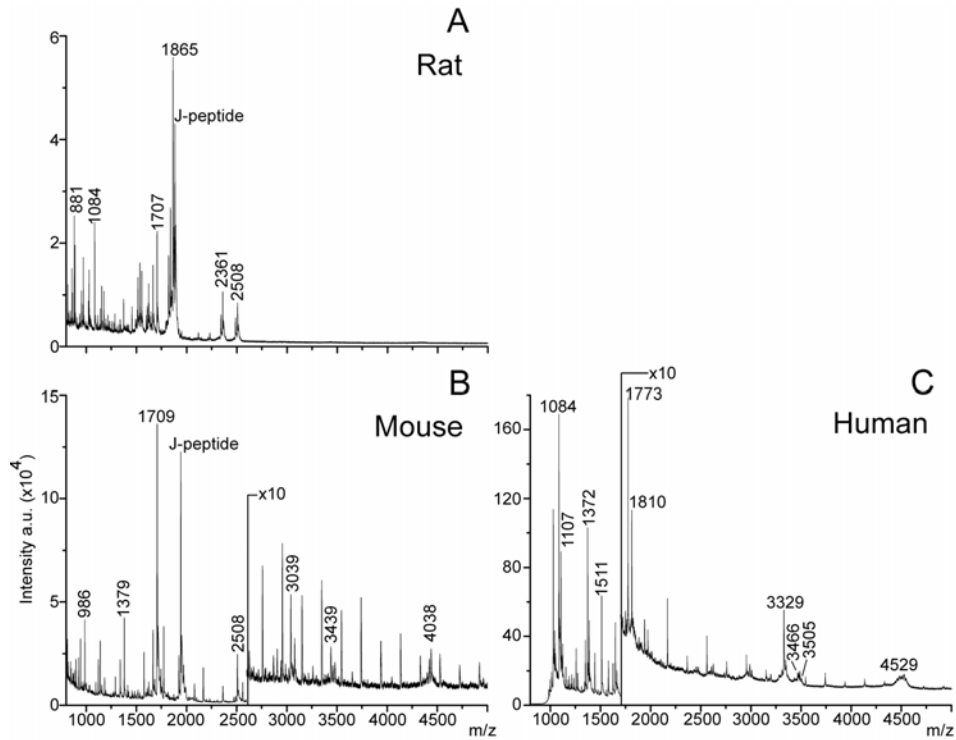
Figure 2. MALDI-IMS spectra of mammalian pituitary tissue sections. Summed mass spectra of direct MALDI analysis of a (A) HCCA covered rat pituitary, (B) DHB covered mouse pituitary and (C) HCCA covered human pituitary tissue section.

The molecular weight of the POMC protein in mouse, rat and human is 26707, 26540 and 29424 Da respectively, showing the largest difference exists between the human protein compared to the ones from mouse and rat. For this reason similar processing steps in the different organisms may lead to peptides with small differences in their amino acid sequence and thus in their mass. For example the amino acid sequence of β-endorphin in rat (YGGFMTSEKSQTPLVTLFKNAIIKNVHKKGQ, mass 3463.86) differs one amino acid from the sequence in mice (YGGFMTSEKSQTPLVTLFKNAIIKNAHKKGQ, mass

3435.83) and three amino acids from the β-endorphin sequences in humans (YGGFMTSEKSQTPLVTLFKNAIIKN<u>AY</u>KKG<u>E</u>, mass 3462.82). The before mentioned J-peptide, which differs 58 Da in mass between mouse and rat is even completely absent in humans. This phenomenon can be used to distinguish between different tissue types using IMS, where conventional imaging techniques like staining or fluorescence microscopy cannot. Furthermore, using MS the presence of amino acid substitutions are detected simultaneously with the imaging experiment itself. This demonstrates the possibility of IMS to reveal peptide or protein modifications directly from diseased tissue.

To verify the assignment of the observed peptides both LC-MS/MS and high mass accuracy MALDI FTICR-MS were used. In the LC-MS/MS experiment an extract of the rat pituitary was analyzed using a Q-ToF 2. Using this method, we were able to confirm the identity of peptides like vasopressin (data not shown). However, it is not trivial to elucidate the (endogenous) neuropeptide sequences from the masses observed in the imaging experiment using this technique. The use of a different ionization technique, electrospray versus MALDI, favors the ionization of different peptides and there are no databases available to identify endogenous neuropeptides on bases of their MS/MS spectra. To overcome these difficulties we used MALDI FTICR-MS, directly on mouse pituitary tissue sections to confirm the peptide assignments. Here the exact same sample preparation and ionization technique as in IMS can be used combined with high mass accuracy data analysis of the endogenous neuropeptides. Although the accurate mass analysis was enough to confirm the peptide assignments, we performed an infrared multiphoton dissociation (IRMPD) experiment on one of the peptides (J-peptide at m/z 1941) in the mouse pituitary. The resulting spectrum shows the expected fragments of the J-peptide and further helped in validating the assignment of the peptides. Table 1 shows the assigned peaks from the different MS experiments. In the MALDI ToF spectra a lot of unidentified peaks remain and thus further tandem MS experiments are required to assign these peaks as well.

Table 1. Peptides from the MALDI-IMS analysis of rat, mouse and human pituitary and the FT-ICR analysis of the mouse pituitary tissue sections. All observed masses in the MALDI-IMS analysis are average masses except for the ones marked with a *, the masses obtained in the FT-ICR experiment are all mono-isotopic.

Peptide	Rat Pituitary IMS		Mouse Pituitary IMS		FT-ICR		Human Pituitary IMS	
	Observed	Expected	Observed	Expected	Observed*	Expected*	Observed	Expected
ProOT/Oxytocin (+Na)	*1028,5	1028,4					1029,6	1029,2
ProVP/vasopressin	*1083,7	1083,4					*1084,3	1083,4
POMC/des-Ac-α-MSH (5-13)							*1154,6	1154,6
ProVP/C-terminal fragment	1608,2	1607,8						
POMC/ des-Ac-α-MSH	1623,4	1623,9	1624,2	1623,9			1623,9	1623,9
POMC/Ac-α-MSH	1665,5	1665,9	1666,3	1665,9	1664,813	1664,801		
POMC/diAc-α-MSH	1707,3	1708,0	1708,2	1708,0	1706,825	1706,811		
POMC/J-peptide (-18 Da)	1864,6							
POMC/J-peptide	1882,9	1883,9	1942,7	1942,0	1940,879	1940,863		
ProVP/C-terminal fragment	1948,2	1948,2						
POMC/Arg-CLIP (1-21)	2360,2	2360,6						
POMC/Arg-CLIP (1-22)	2507,3	2507,8	2507,9	2507,8	2506,297	2506,262		
POMC/Arg-CLIP (+Na)					2527,237	2527,260		
POMC/potential peptide							3006,9	3006,2
POMC/β-endorphin			3439,9	3438,1			3466,5	3466,1
POMC/Ac-β-endorphin			3479,8	3480,1			3505,0	3507,0

*mono-isotopic.

Figure 3A shows an optical image of a pituitary gland from an adult rat. The rat pituitary consists of three distinct regions; the anterior, intermediate and posterior lobe. In Figure 3B the stigmatic total-ion-count (TIC) image of the entire rat pituitary tissue section is shown in grayscale.
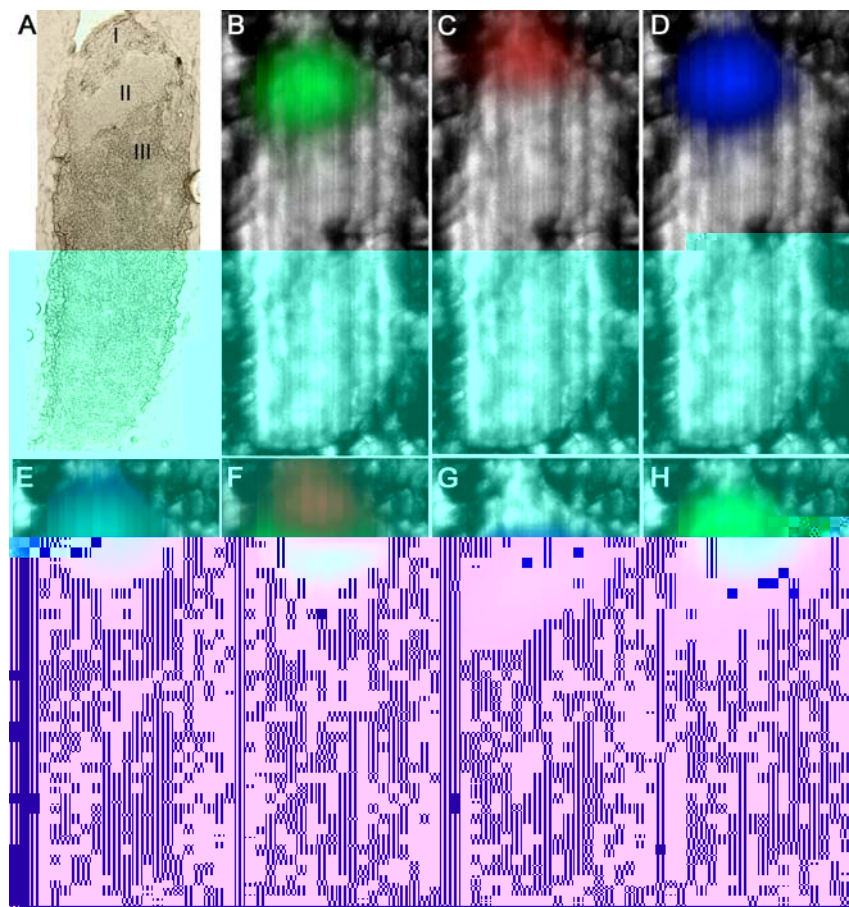
Figure 3. Molecular imaging of rat pituitary tissue by MALDI-IMS. (A) Optical image of an untreated rat pituitary tissue section, with (I) the posterior lobe, (II) the intermediate lobe and (III) the anterior lobe. (B) Distribution of the selected ion image of vasopressin (green), (C) oxytocin (red) and (D) c-terminal fragment of the ProVP precursor (blue) overlaid on the TIC image in grayscale. (E) Combined distributions of vasopressin (green) and the c-terminal fragment (blue) and (F) vasopressin (green) and oxytocin (red) overlaid on the TIC image in grayscale. (G) Distribution of the selected ion image of α-MSH (blue) and (H) Combined distributions of vasopressin (green) α-MSH (blue) overlaid on the TIC image in grayscale. Scale bar is 200 μm, tissue was covered with HCCA.

Figure 3C-I show the MS images of the neuropeptide distributions in rat pituitary. In this experiment after each linescan the sample stage was moved upwards by 100 μm, resulting in a pixel size for the overlaid course m/z data of 10×100 μm. The images clearly show distinct localization of several endogenous neuropeptides in the different lobes of the pituitary. The POMC peptide α-MSH, in its different forms of acetylation, is localized in the intermediate pituitary were it is synthesized and secreted (3H). The peptides vasopressin (3C) and oxytocin (3D) are localized in the posterior pituitary. A difference in localization can be seen between oxytocin and vasopressin within the same posterior pituitary (3G), while signals derived from the ProVP precursor (3E) at m/z 1610 (c-terminal fragment) and m/z 1947 (fragment 156-168) co-localize with the vasopressin signal (F). This result shows the ability to distinguish between clusters of different secretory cells within a ~250 μm^2 area of the rat pituitary, using high spatial resolution imaging MS.

In the human pituitary tissue the peptide vasopressin is abundantly present, protonated and sodiated, as well as the sodiated form of oxytocin. α-MSH is only present in its des-acetylated form while β-endorphin can be found both with and without an acetyl group. Since the human pituitary is approximately ten times bigger than the mouse and rat pituitary, the signal intensity of the combined mass spectra is also ~10 times higher.

Figure 4A shows an optical image of a human pituitary tissue section. The tissue section comprises both the adenohypophysis (left) and the neurohypophysis (right). Figure 4B shows the TIC image of the human pituitary tissue section. The contours and spatial details can again be clearly distinguished. Figures 4C-F show the molecular distribution of several neuropeptides in the human pituitary. The experiment was conducted in a similar fashion as in the case of the rat pituitary tissue, with the only difference being the distance between two linescans, which was 120 μm, resulting in a microprobe SIC pixel size of 10×120 μm. Both vasopressin (4C) and oxytocin (4D) nicely localize within the neurohypophysis and α-MSH in the adenohypophysis (4E).
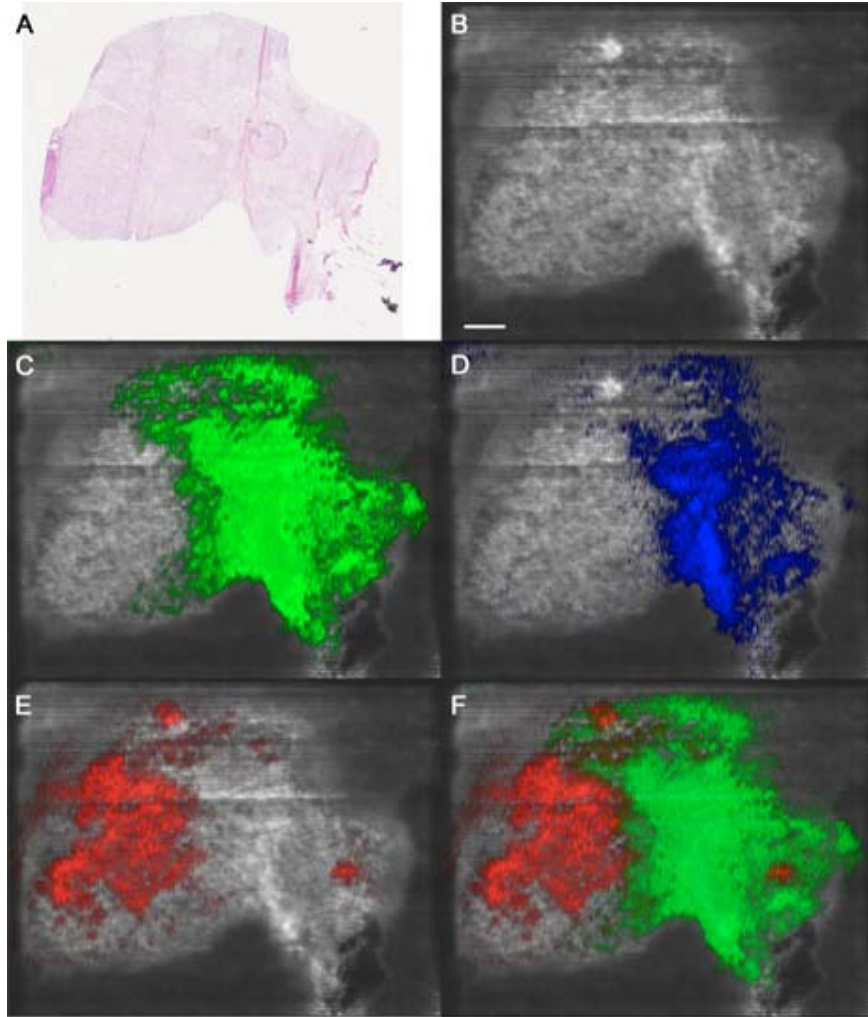
Figure 4. Molecular imaging of human pituitary tissue by MALDI-IMS. (A) Optical image of an H&E stained human pituitary tissue section. (B) TIC MALDI-IMS image in grayscale of a tissue section adjacent to the one in the optical image. Neuropeptide distributions overlaid on the grayscale TIC image with (C) vasopressin in green (D) oxytocin in blue (E) α-MSH in red. (F) Overlay of vasopressin (green) and α-MSH (red). Scale bar is 1 mm.

6.4 Conclusions

The high spatial resolution capability of the mass microscope allows localization of neuropeptides directly from tissue within tissue features at cell cluster length scales. In this approach either the combination of a high-resolution TIC background image with overlaid mass spectral data or high-resolution single ion microscope images can be obtained with the latter showing unprecedented detail with pixel sizes of 500 nm and resolving power of 4 μm. The sample preparation used to obtain the high-resolution images did not lead to diffusion of the analytes within or from the tissue. MS is able to distinguish different types of mammalian tissue based on the presence of differences in amino acid sequences of (neuro)peptides with similar function. This feature gives IMS an advantage over conventional imaging techniques in that it is able to look for small peptide or protein modifications (amino acid substitutions and post-translational modifications) in diseased tissue without prior knowledge.

Bibliography

1.	Preuss, T. M., Caceres, M., Oldham, M. C. & Geschwind, D. H. *Human brain evolution: Insights from microarrays*. Nature Rev. Genet. **5**, 850-860 (2004).
2.	Watanabe, H. et al. *DNA sequence and comparative analysis of chimpanzee chromosome 22*. Nature **429**, 382-388 (2004).
3.	Venter, J. C. et al. *The sequence of the human genome*. Science **291**, 1304-1351 (2001).
4.	Lander, E. S. et al. *Initial sequencing and analysis of the human genome*. Nature **409**, 860-921 (2001).
5.	Patterson, S. D. & Aebersold, R. H. *Proteomics: the first decade and beyond*. Nature Genet. **33**, 311-323 (2003).
6.	Aebersold, R. *Constellations in a cellular universe*. Nature **422**, 115-116 (2003).
7.	Elek, G. & Lapis, K. *A path or a new road in laboratory diagnostics? Biological mass spectrometry: Facts and perspectives*. Pathol. Oncol. Res. **12**, 179-183 (2006).
8.	Pandey, A. & Mann, M. *Proteomics to study genes and genomes*. Nature **405**, 837-846 (2000).
9.	Hanash, S. *Disease proteomics*. Nature **422**, 226-232 (2003).
10.	Figeys, D. *Proteomics approaches in drug discovery*. Anal. Chem. **74**, 413a-419a (2002).
11.	Stamm, S. et al. *Function of alternative splicing*. Gene **344**, 1-20 (2005).
12.	Chung, J.-J., Shikano, S., Hanyu, Y. & Li, M. *Functional diversity of protein C-termini: more than zipcoding?* Trends Cell Biol. **12**, 146-150 (2002).
13.	Grabowski, P. J. & Black, D. L. *Alternative RNA splicing in the nervous system*. Prog. Neurobiol. **65**, 289-308 (2001).
14.	Dreger, M. *Subcellular proteomics*. Mass Spectrom. Rev. **22**, 27-56 (2003).
15.	Andersen, J. S. & Mann, M. *Organellar proteomics: turning inventories into insights*. EMBO Reports **7**, 874-879 (2006).
16.	Kumar, A. et al. *Subcellular localization of the yeast proteome*. Genes Dev. **16**, 707-719 (2002).
17.	Calero, M. et al. *Dual Prenylation Is Required for Rab Protein Localization and Function*. Mol. Biol. Cell **14**, 1852-1867 (2003).
18.	Phizicky, E., Bastiaens, P. I. H., Zhu, H., Snyder, M. & Fields, S. *Protein analysis on a proteomic scale*. Nature **422**, 208-215 (2003).

19. Zaccai, M. & Lipshitz, H. D. *Role of Adducin-like (hu-li tai shao) mRNA and protein localization in regulating cytoskeletal structure and function during Drosophila oogenesis and early embryogenesis*. Dev. Genet. **19**, 249-257 (1996).

20. Bastiaens, P. I. H. & Pepperkok, R. *Observing proteins in their natural habitat: the living cell*. Trends Biochem. Sci. **25**, 631-637 (2000).

21. Wouters, F. S., Verveer, P. J. & Bastiaens, P. I. H. *Imaging biochemistry inside cells*. Trends Cell Biol. **11**, 203-211 (2001).

22. Zhang, J., Campbell, R. E., Ting, A. Y. & Tsien, R. Y. *Creating new fluorescent probes for cell biology*. Nature Rev. Mol. Cell Bio. **3**, 906-918 (2002).

23. Huh, W. K. et al. *Global analysis of protein localization in budding yeast*. Nature **425**, 686-691 (2003).

24. Aebersold, R. & Mann, M. *Mass spectrometry-based proteomics*. Nature **422**, 198-207 (2003).

25. Stoeckli, M., Chaurand, P., Hallahan, D. E. & Caprioli, R. M. *Imaging mass spectrometry: a new technology for the analysis of protein expression in mammalian tissues*. Nature Med. **7**, 493-6 (2001).

26. McDonnell, L. A. et al. *Subcellular imaging mass spectrometry of brain tissue*. J. Mass Spectrom. **40**, 160-168 (2005).

27. Alberts, B. *Molecular biology of the cell* Garland Science, New York ; London, 1227-1242, 2002.

28. Jimenez, C. R. *Generation of Complex Peptide Diversity in Neuroendocrine Cells of Lymnaea stagnalis and the Rat*. Molecular Neurobiology, Vrije Universtiteit, Amsterdam, 1997.

29. Vangolen, F. A. et al. *Co-Localized Neuropeptides Conopressin and Ala-Pro-Gly-Trp-Nh2 Have Antagonistic Effects on the Vas-Deferens of Lymnaea*. Neuroscience **69**, 1275-1287 (1995).

30. Jimenez, C. R. et al. *Direct mass spectrometric peptide profiling and sequencing of single neurons reveals differential peptide patterns in a small neuronal network*. Biochemistry-Us **37**, 2070-2076 (1998).

31. Li, L. J., Garden, R. W. & Sweedler, J. V. *Single-cell MALDI: a new tool for direct peptide profiling*. Trends in Biotechnology **18**, 151-160 (2000).

32. De Lange, R. P. J., van Golen, F. A. & van Minnen, J. *Diversity in cell specific co-expression of four neuropeptide genes involved in control of male copulation behaviour in Lymnaea stagnalis.* Neuroscience **78**, 289-299 (1997).

33. De Lange, R. P. J. & van Minnen, J. *Localization of the neuropeptide APGWamide in gastropod molluscs by in situ hybridization and immunocytochemistry*. Gen. Comp. Endocrinol. **109**, 166-174 (1998).

34. Jimenez, C. R. et al. *Neuropeptide Expression and Processing as Revealed by Direct Matrix-Assisted Laser-Desorption Ionization Mass-Spectrometry of Single Neurons*. J. Neurochem. **62**, 404-407 (1994).

35. van Veelen, P. A. et al. *Direct Peptide Profiling of Single Neurons by Matrix-Assisted Laser-Desorption Ionization Mass-Spectrometry*. Org. Mass Spectrom. **28**, 1542-1546 (1993).

36. Li, K. W. et al. *Structural elucidation of a peptide from a single neuron by matrix-assisted laser desorption/ionization employing a tandem double focusing magnetic-orthogonal acceleration time-of-flight mass spectrometer*. Anal. Chem. **69**, 563-565 (1997).

37. Croll, R. P. & van Minnen, J. *Distribution of the Peptide Ala-Pro-Gly-Trp-Nh2 (Apgwamide) in the Nervous-System and Periphery of the Snail Lymnaea-Stagnalis as Revealed by Immunocytochemistry and Insitu Hybridization*. J. Comp. Neurol. **324**, 567-574 (1992).

38. Jimenez, C. R. et al. *Spatio-temporal dynamics of the egg-laying-inducing peptides during an egg-laying cycle: a semiquantitative matrix-assisted laser desorption/ionization mass spectrometry approach*. J. Neurochem. **89**, 865-75 (2004).

39. Mckinley, M. J. et al. *Circumventricular Organs - Neuroendocrine Interfaces between the Brain and the Hemal Milieu*. Front. Neuroendocrinol. **11**, 91-127 (1990).

40. McKinley, M. J. & Oldfield, B. J. *The brain as an endocrine target for peptide hormones*. Trends Endocrin. Met. **9**, 349-354 (1998).

41. Markakis, E. A. *Development of the neuroendocrine hypothalamus*. Front. Neuroendocrinol. **23**, 257-291 (2002).

42. Swaab, D. F. et al. *Functional Neuroanatomy and Neuropathology of the Human Hypothalamus*. Anat. Embryol. **187**, 317-330 (1993).

43. Paxinos, G. & Watson, C. *The rat brain in stereotaxic coordinates* Academic Press, San Diego, xxvi , [237] of plates, 1998.

44. Campbell, P. & Dhand, R. *Obesity*. Nature **404**, 631 (2000).

45. Pritchard, L. E., Turnbull, A. V. & White, A. *Pro-opiomelanocortin processing in the hypothalamus: impact on melanocortin signalling and obesity*. J. Endocrinol. **172**, 411-421 (2002).

46. Poggioli, R., Vergoni, A. V. & Bertolini, A. *ACTH-(1-24) and [alpha]-MSH antagonize feeding behavior stimulated by kappa opiate agonists*. Peptides **7**, 843-848 (1986).

47. Irani, B. G. & Haskell-Luevano, C. *Feeding effects of melanocortin ligands - A historical perspective*. Peptides **26**, 1788-1799 (2005).

48. Chung, S. & Civelli, O. *Orphan neuropeptides: Novel neuropeptides modulating sleep or feeding*. Neuropeptides **40**, 233-243 (2006).

49.   Gershengorn, M. C. & Osman, R. *Minireview: Insights into G protein-coupled receptor function using molecular models*. Endocrinology **142**, 2-10 (2001).

50.   Tanaka, S., Yora, T., Nakayama, K., Inoue, K. & Kurosumi, K. *Proteolytic processing of pro-opiomelanocortin occurs in acidifying secretory granules of AtT-20 cells*. J. Histochem. Cytochem. **45**, 425-436 (1997).

51.   Xu, H. X. & Shields, D. *Prohormone Processing in the Trans-Golgi Network - Endoproteolytic Cleavage of Prosomatostatin and Formation of Nascent Secretory Vesicles in Permeabilized Cells*. J. Cell Biol. **122**, 1169-1184 (1993).

52.   Hillebrand, J. J. G., de Wied, D. & Adan, R. A. H. *Neuropeptides, food intake and body weight regulation: a hypothalamic focus*. Peptides **23**, 2283-2306 (2002).

53.   Schwartz, M. W., Woods, S. C., Porte, D., Seeley, R. J. & Baskin, D. G. *Central nervous system control of food intake*. Nature **404**, 661-671 (2000).

54.   Fan, W., Boston, B. A., Kesterson, R. A., Hruby, V. J. & Cone, R. D. *Role of melanocortinergic neurons in feeding and the agouti obesity syndrome*. Nature **385**, 165-168 (1997).

55.   Flier, J. S. & Maratos-Flier, E. *Obesity and the hypothalamus: Novel peptides for new pathways*. Cell **92**, 437-440 (1998).

56.   Tsujii, S. & Bray, G. A. *Acetylation alters the feeding response to MSH and beta-endorphin*. Brain Res. Bull. **23**, 165-169 (1989).

57.   Stuart, J. N., Hummon, A. B. & Sweedler, J. V. *The chemistry of thought: Neurotransmitters in the brain*. Anal. Chem. **76**, 120a-128a (2004).

58.   Karas, M. & Hillenkamp, F. *Laser Desorption Ionization of Proteins with Molecular Masses Exceeding 10000 Daltons*. Anal. Chem. **60**, 2299-2301 (1988).

59.   Garden, R. W., Moroz, L. L., Moroz, T. P., Shippy, S. A. & Sweedler, J. V. *Excess Salt Removal with Matrix Rinsing: Direct Peptide Profiling of Neurons from Marine Invertebrates Using Matrix-assisted Laser Desorption/Ionization Time-of-flight Mass Spectrometry*. J. Mass Spectrom. **31**, 1126-1130 (1996).

60.   Caprioli, R. M., Farmer, T. B. & Gile, J. *Molecular imaging of biological samples: Localization of peptides and proteins using MALDI-TOF MS*. Anal. Chem. **69**, 4751-4760 (1997).

61.   Rubakhin, S. S., Churchill, J. D., Greenough, W. T. & Sweedler, J. V. *Profiling signaling peptides in single mammalian cells using mass spectrometry*. Anal. Chem. **78**, 7267-7272 (2006).

62.   Rubakhin, S. S., Garden, R. W., Fuller, R. R. & Sweedler, J. V. *Measuring the peptides in individual organelles with mass spectrometry*. Nature Biotechnol. **18**, 172-175 (2000).

63.   Rohner, T. C., Staab, D. & Stoeckli, M. *MALDI mass spectrometric imaging of biological tissue sections*. Mech. Ageing Dev. **126**, 177-185 (2005).

64.   Stoeckli, M., Staab, D., Staufenbiel, M., Wiederhold, K. H. & Signor, L. *Molecular imaging of amyloid beta peptides in mouse brain sections using mass spectrometry*. Anal. Biochem. **311**, 33-39 (2002).

65.   Skold, K. et al. *Decreased Striatal Levels of PEP-19 Following MPTP Lesion in the Mouse*. J. Proteome Res. **5**, 262-269 (2006).

66.   Meistermann, H. et al. *Biomarker Discovery by Imaging Mass Spectrometry: Transthyretin is a Biomarker for Gentamicin-induced Nephrotoxicity in Rat*. Mol Cell Proteomics **5**, 1876-1886 (2006).

67.   Chaurand, P., Schwartz, S. A. & Caprioli, R. M. *Profiling and imaging proteins in tissue sections by MS*. Analytical Chemistry **76**, 86a-93a (2004).

68.   Khatib-Shahidi, S., Andersson, M., Herman, J. L., Gillespie, T. A. & Caprioli, R. M. *Direct molecular analysis of whole-body animal tissue sections by imaging MALDI mass spectrometry*. Anal. Chem. **78**, 6448-6456 (2006).

69.   Vickerman, J. C. & Briggs, D. *ToF-SIMS: surface analysis by mass spectrometry* IM Publications and SurfaceSpectra Limited, Chichester, 2001.

70.   Pacholski, M. L. & Winograd, N. *Imaging with mass spectrometry*. Chem. Rev. **99**, 2977-3005 (1999).

71.   Van Vaeck, L., Adriaens, A. & Gijbels, R. *Static secondary ion mass spectrometry: (S-SIMS) Part 1. Methodology and structural interpretation*. Mass Spectrom. Rev. **18**, 1-47 (1999).

72.   John, C. M. & Odom, R. W. *Static secondary ion mass spectrometry (SSIMS) of biological compounds in tissue and tissue-like matrices*. Int. J. Mass Spectrom. **161**, 47-67 (1997).

73.   Todd, P. J., McMahon, J. M., Short, R. T. & McCandlish, C. A. *Organic SIMS of biologic tissue*. Anal. Chem. **69**, A529-A535 (1997).

74.   Todd, P. J., Schaaff, T. G., Chaurand, P. & Caprioli, R. M. *Organic ion imaging of biological tissue with secondary ion mass spectrometry and matrix-assisted laser desorption/ionization*. J. Mass Spectrom. **36**, 355-69 (2001).

75.   Chandra, S. & Morrison, G. H. *Imaging Ion and Molecular-Transport at Subcellular Resolution by Secondary-Ion Mass-Spectrometry*. Int. J. Mass Spectrom. **143**, 161-176 (1995).

76. Kleinfeld, A. M., Kampf, J. P. & Lechene, C. *Transport of 13C-oleate in adipocytes measured using multi imaging mass spectrometry*. J. Am. Soc. Mass Spectr. **15**, 1572-1580 (2004).

77. Peteranderl, R. & Lechene, C. *Measure of carbon and nitrogen stable isotope ratios in cultured cells*. J. Am. Soc. Mass Spectr. **15**, 478-485 (2004).

78. Chandra, S., Smith, D. R. & Morrison, G. H. *Subcellular imaging by dynamic SIMS ion microscopy*. Anal. Chem. **72**, 104A-114A (2000).

79. Strick, R., Strissel, P. L., Gavrilov, K. & Levi-Setti, R. *Cation-chromatin binding as shown by ion microscopy is essential for the structural integrity of chromosomes*. J. Cell Biol. **155**, 899-910 (2001).

80. Hallegot, P., Peteranderl, R. & Lechene, C. *In-Situ imaging mass spectrometry analysis of melanin granules in the human hair shaft*. J. Invest. Dermatol. **122**, 381-386 (2004).

81. Mangabeira, P. A. O. et al. *Accumulation of chromium in root tissues of Eichhornia crassipes (Mart.) Solms. in Cachoeira river - Brazil*. Appl. Surf. Sci. **231-2**, 497-501 (2004).

82. Mangabeira, P. A. et al. *Chromium localization in plant tissues of Lycopersicum esculentum Mill using ICP-MS and ion microscopy (SIMS)*. Appl. Surf. Sci. **252**, 3488-3501 (2006).

83. Imai, T., Tanabe, K., Kato, T. & Fukushima, K. *Localization of ferruginol, a diterpene phenol, in Cryptomeria japonica heartwood by time-of-flight secondary ion mass spectrometry*. Planta **221**, 549-556 (2005).

84. Monroe, E. B., Jurchen, J. C., Lee, J., Rubakhin, S. S. & Sweedler, J. V. *Vitamin E imaging and localization in the neuronal membrane*. J. Am. Chem. Soc. **127**, 12152-12153 (2005).

85. Amemiya, T., Gong, H., Takaya, K., Tozu, M. & Ohashi, Y. *Changes of vitamins A and E in the rat retina under light and dark conditions detected with TOF-SIMS*. Appl. Surf. Sci. **203**, 738-741 (2003).

86. Pacholski, M. L., Cannon, D. M., Jr., Ewing, A. G. & Winograd, N. *Static time-of-flight secondary ion mass spectrometry imaging of freeze-fractured, frozen-hydrated biological membranes*. Rapid Commun. Mass Spectrom. **12**, 1232-5 (1998).

87. McQuaw, C. M., Sostarecz, A. G., Zheng, L. L., Ewing, A. G. & Winograd, N. *Lateral heterogeneity of dipalmitoylphosphatidylethanolamine-cholesterol Langmuir-Blodgett films investigated with imaging time-of-flight secondary ion mass spectrometry and atomic force microscopy*. Langmuir **21**, 807-813 (2005).

88. Ostrowski, S. G. et al. *Secondary ion MS imaging of lipids in picoliter vials with a buckminsterfullerene ion source*. Anal. Chem. **77**, 6190-6196 (2005).

89.	Altelaar, A. F. M., van Minnen, J., Heeren, R. M. A. & Piersma, S. R. *The influence of the cholesterol microenvironment in tissue sections on molecular ionization efficiencies and distributions in ToF-SIMS*. Appl. Surf. Sci. **252**, 6702-6705 (2006).

90.	Gong, H., Amemiya, T., Takaya, K., Tozu, M. & Ohashi, Y. *Time-of-flight secondary ion mass spectrometry of fatty acids in rat retina*. Appl. Surf. Sci. **203**, 734-737 (2003).

91.	Ostrowski, S. G., Van Bell, C. T., Winograd, N. & Ewing, A. G. *Mass spectrometric imaging of highly curved membranes during Tetrahymena mating*. Science **305**, 71-73 (2004).

92.	Roddy, T. P., Cannon, D. M., Meserole, C. A., Winograd, N. & Ewing, A. G. *Imaging of freeze-fractured cells with in situ fluorescence and time-of-flight secondary ion mass spectrometry*. Anal. Chem. **74**, 4011-4019 (2002).

93.	Roddy, T. P., Cannon, D. M., Ostrowski, S. G., Winograd, N. & Ewing, A. G. *Identification of cellular sections with imaging mass spectrometry following freeze fracture*. Anal. Chem. **74**, 4020-4026 (2002).

94.	Appelhans, A. D. & Delmore, J. E. *Comparison of Polyatomic and Atomic Primary Beams for Secondary Ion Mass-Spectrometry of Organics*. Anal. Chem. **61**, 1087-1093 (1989).

95.	Winograd, N. *The magic of cluster SIMS*. Anal. Chem. **77**, 142a-149a (2005).

96.	Gillen, G. & Fahey, A. *Secondary ion mass spectrometry using cluster primary ion beams*. Appl. Surf. Sci. **203**, 209-213 (2003).

97.	Postawa, Z. et al. *Microscopic insights into the sputtering of Ag{111} induced by C-60 and Ga bombardment*. J. Phys. Chem. B **108**, 7831-7838 (2004).

98.	Zaric, R., Pearson, B., Krantzman, K. D. & Garrison, B. J. *Molecular dynamics simulations to explore the effect of projectile size on the ejection of organic targets from metal surfaces*. Int. J. Mass Spectrom. **174**, 155-166 (1998).

99.	Weibel, D. et al. *A C-60 primary ion beam system for time of flight secondary ion mass spectrometry: Its development and secondary ion yield characteristics*. Anal. Chem. **75**, 1754-1764 (2003).

100.	Fletcher, J. S. et al. *TOF-SIMS analysis using C-60- effect of impact energy on yield and damage*. Anal. Chem. **78**, 1827-1831 (2006).

101.	Zenobi, R. & Knochenmuss, R. *Ion formation in MALDI mass spectrometry*. Mass Spectrom. Rev. **17**, 337-366 (1998).

102.	Wu, K. J. & Odom, R. W. *Matrix-enhanced secondary ion mass spectrometry: a method for molecular analysis of solid surfaces*. Anal. Chem. **68**, 573-882 (1996).

103. Delcorte, A. & Bertrand, P. *Interest of silver and gold metallization for molecular SIMS and SIMS imaging*. Appl. Surf. Sci. **231-2**, 250-255 (2004).
104. Delcorte, A. & Garrison, B. J. *High yield events of molecular emission induced by kiloelectronvolt particle bombardment*. J. Phys. Chem. B **104**, 6785-6800 (2000).
105. Delcorte, A., Medard, N. & Bertrand, P. *Organic secondary ion mass spectrometry: Sensitivity enhancement by gold deposition*. Anal. Chem. **74**, 4955-4968 (2002).
106. Adriaensen, L., Vangaever, F. & Gijbels, R. *Metal-assisted secondary ion mass spectrometry: Influence of Ag and Au deposition on molecular ion yields*. Anal. Chem. **76**, 6777-6785 (2004).
107. Delcorte, A. & Garrison, B. J. *Particle-induced desorption of kilodalton molecules embedded in a matrix: A molecular dynamics study*. J. Phys. Chem. B **107**, 2297-2310 (2003).
108. Delcorte, A., Vanden Eynde, X., Bertrand, P., Vickerman, J. C. & Garrison, B. J. *Kiloelectronvolt particle-induced emission and fragmentation of polystyrene molecules adsorbed on silver: Insights from molecular dynamics*. J. Phys. Chem. B **104**, 2673-2691 (2000).
109. Hagenhoff, B. in *ToF-SIMS : surface analysis by mass spectrometry* (ed. Briggs, D.) 293 (SurfaceSpectra and IM, Chichester, 2001).
110. Karas, M., Bachmann, D. & Hillenkamp, F. *Influence of the Wavelength in High-Irradiance Ultraviolet Laser Desorption Mass Spectrometry of Organic Molecules*. Anal. Chem. **57**, 2935-2939 (1985).
111. Tanaka, K. et al. *Protein and polymer analyses up to m/z 100 000 by laser ionization time-of-flight mass spectrometry*. Rapid Commun. Mass Spectrom. **2**, 151-153 (1988).
112. Zhigilei, L. V., Kodali, P. B. S. & Garrison, B. J. *A microscopic view of laser ablation*. J. Phys. Chem. B **102**, 2845-2853 (1998).
113. Knochenmuss, R. *A quantitative model of ultraviolet matrix-assisted laser desorption/ionization including analyte ion generation*. Anal. Chem. **75**, 2199-2207 (2003).
114. Karas, M., Gluckmann, M. & Schafer, J. *Ionization in matrix-assisted laser desorption/ionization: singly charged molecular ions are the lucky survivors*. J. Mass Spectrom. **35**, 1-12 (2000).
115. Karas, M. & Kruger, R. *Ion formation in MALDI: The cluster ionization mechanism*. Chem. Rev. **103**, 427-439 (2003).
116. Knochenmuss, R. & Zhigilei, L. V. *Molecular dynamics model of ultraviolet matrix-assisted laser desorption/ionization including ionization processes*. J. Phys. Chem. B **109**, 22947-22957 (2005).
117. Dreisewerd, K. *The desorption process in MALDI*. Chem. Rev. **103**, 395-425 (2003).

118. Dreisewerd, K., Schurenberg, M., Karas, M. & Hillenkamp, F. *Influence of the Laser Intensity and Spot Size on the Desorption of Molecules and Ions in Matrix-Assisted Laser-Desorption Ionization with a Uniform Beam Profile*. Int. J. Mass Spectrom. **141**, 127-148 (1995).
119. Knochenmuss, R. *A quantitative model of ultraviolet matrix-assisted laser desorption/ionization*. J. Mass Spectrom. **37**, 867-877 (2002).
120. Horneffer, V. et al. *Is the incorporation of analytes into matrix crystals a prerequisite for matrix-assisted laser desorption/ionization mass spectrometry? A study of five positional isomers of dihydroxybenzoic acid*. Int. J. Mass Spectrom. **187**, 859-870 (1999).
121. Horneffer, V. et al. *Matrix-analyte-interaction in MALDI-MS: Pellet and nano-electrospray preparations*. Int. J. Mass Spectrom. **249**, 426-432 (2006).
122. Trimpin, S., Rader, H. J. & Mullen, K. *Investigations of theoretical principles for MALDI-MS derived from solvent-free sample preparation - Part I. Preorganization*. Int. J. Mass Spectrom. **253**, 13-21 (2006).
123. Wang, M. Z. & Fitzgerald, M. C. *A solid sample preparation method that reduces signal suppression effects in the MALDI analysis of peptides*. Anal. Chem. **73**, 625-631 (2001).
124. Schlosser, G., Pocsfalvi, G., Huszar, E., Malorni, A. & Hudecz, F. *MALDI-TOF mass spectrometry of a combinatorial peptide library: effect of matrix composition on signal suppression*. J. Mass Spectrom. **40**, 1590-1594 (2005).
125. Krause, E., Wenschuh, H. & Jungblut, P. R. *The dominance of arginine-containing peptides in MALDI-derived tryptic mass fingerprints of proteins*. Anal. Chem. **71**, 4160-4165 (1999).
126. Luxembourg, S. L. *Thesis: Mass Microscopy: Imaging Biomolecules on Surfaces*. Macromolecular Ion Physics, AMOLF, Amsterdam, 2005.
127. Luxembourg, S. L., Mize, T. H., McDonnell, L. A. & Heeren, R. M. A. *High-spatial resolution mass spectrometric imaging of peptide and protein distributions on a surface*. Anal. Chem. **76**, 5339-5344 (2004).
128. Schueler, B. W. *ToF-SIMS: surface analysis by mass spectrometry* (ed. Briggs, D.), IM Publications and SurfaceSpectra Limited, Chichester, 75-94, 2001.
129. Schueler, B., Sander, P. & Reed, D. A. *A Time-of-Flight Secondary Ion-Microscope*. Vacuum **41**, 1661-1664 (1990).
130. Schueler, B. W. *Microscope Imaging by Time-of-Flight Secondary Ion Mass-Spectrometry*. Microsc. Microanal. Microstruct. **3**, 119-139 (1992).
131. Lemaire, R. et al. *MALDI-MS Direct Tissue Analysis of Proteins: Improving Signal Sensitivity Using Organic Treatments*. Anal. Chem. **78**, 7145-7153 (2006).

132.   Lemaire, R. et al. *Solid Ionic Matrixes for Direct Tissue Analysis and MALDI Imaging*. Anal. Chem. **78**, 809-819 (2006).

133.   Nakanishi, T., Ohtsu, I., Furuta, M., Ando, E. & Nishimura, O. *Direct MS/MS Analysis of Proteins Blotted on Membranes by a Matrix-Assisted Laser Desorption/Ionization-Quadrupole Ion Trap-Time-of-Flight Tandem Mass Spectrometer*. J. Proteome Res. **4**, 743-747 (2005).

134.   Ohtsu, I., Nakanisi, T., Furuta, M., Ando, E. & Nishimura, O. *Direct Matrix-Assisted Laser Desorption/Ionization Time-of-Flight Mass Spectrometric Identification of Proteins on Membrane Detected by Western Blotting and Lectin Blotting*. J. Proteome Res. **4**, 1391-1396 (2005).

135.   Aerni, H. R., Cornett, D. S. & Caprioli, R. M. *Automated acoustic matrix deposition for MALDI sample preparation*. Anal. Chem. **78**, 827-834 (2006).

136.   Dierks, T. et al. *Multiple sulfatase deficiency is caused by mutations in the gene encoding the human C-alpha-formylglycine generating enzyme*. Cell **113**, 435-444 (2003).

137.   Guo, L., Munzberg, H., Stuart, R. C., Nillni, E. A. & Bjorbaek, C. *N-acetylation of hypothalamic {alpha}-melanocyte-stimulating hormone and regulation by leptin*. PNAS **101**, 11797-11802 (2004).

138.   Wang, J. Z., GrundkeIqbal, I. & Iqbal, K. *Glycosylation of microtubule-associated protein tau: An abnormal posttranslational modification in Alzheimer's disease*. Nature Med. **2**, 871-875 (1996).

139.   Raina, A. K. et al. *Acetylation: A novel posttranslational modification in Alzheimer disease.* J. Neuropath. Exp. Neur. **62**, 551-551 (2003).

140.   Hoozemans, J. J. M. et al. *The unfolded protein response affects neuronal cell cycle protein expression: Implications for Alzheimer's disease pathogenesis*. Exp. Geront. **41**, 380-386 (2006).

141.   Altelaar, A. F. M. et al. *Gold-Enhanced Biomolecular Surface Imaging of Cells and Tissue by SIMS and MALDI Mass Spectrometry*. Anal. Chem. **78**, 734-742 (2006).

142.   Altelaar, A. F. M. et al. *High-resolution MALDI imaging mass spectrometry allows localization of peptide distributions at cellular length scales in pituitary tissue sections*. Int. J. Mass Spectrom. **260**, 203-211 (2007).

143.   Pierson, J. et al. *Molecular profiling of experimental Parkinson's disease: Direct analysis of peptides and proteins on brain tissue sections by MALDI mass spectrometry*. J. Proteome Res. **3**, 289-295 (2004).

144.   Pierson, J., Svenningsson, P., Caprioli, R. M. & Andren, P. E. *Increased levels of ubiquitin in the 6-OHDA-lesioned striatum of rats*. J. Proteome Res. **4**, 223-226 (2005).

145.   Spengler, B. & Hubert, M. *Scanning microprobe matrix-assisted laser desorption ionization (SMALDI) mass spectrometry: Instrumentation for sub-micrometer resolved LDI and MALDI surface analysis*. J. Am. Soc. Mass Spectr. **13**, 735-748 (2002).

146.   Jurchen, J. C., Rubakhin, S. S. & Sweedler, J. V. *MALDI-MS imaging of features smaller than the size of the laser beam*. J. Am. Soc. Mass Spectr. **16**, 1654-1659 (2005).

147.   Luxembourg, S. L., McDonnell, L. A., Mize, T. H. & Heeren, R. M. A. *Infrared mass spectrometric imaging below the diffraction limit*. J. Proteome Res. **4**, 671-673 (2005).

148.   Colliver, T. L. et al. *Atomic and molecular imaging at the single-cell level with TOF-SIMS*. Anal. Chem. **69**, 2225-31 (1997).

149.   Altelaar, A. F. M., van Minnen, J., Jimenez, C. R., Heeren, R. M. A. & Piersma, S. R. *Direct molecular Imaging of Lymnaea stagnalis nervous tissue at subcellular spatial resolution by mass spectrometry*. Anal. Chem. **77**, 735-741 (2005).

150.   Luxembourg, S. L., McDonnell, L. A., Duursma, M. C., Guo, X. H. & Heeren, R. M. A. *Effect of local matrix crystal variations in matrix-assisted ionization techniques for mass spectrometry*. Anal. Chem. **75**, 2333-2341 (2003).

151.   Wittmaack, K., Szymczak, W., Hoheisel, G. & Tuszynski, W. *Time-of-flight secondary ion mass spectrometry of matrix-diluted oligo- and polypeptides bombarded with slow and fast projectiles: Positive and negative matrix and analyte ion yields, background signals, and sample aging*. J. Am. Soc. Mass Spectr. **11**, 553-563 (2000).

152.   Nygren, H., Malmberg, P., Kriegeskotte, C. & Arlinghaus, H. F. *Bioimaging TOF-SIMS: localization of cholesterol in rat kidney sections*. Febs Letters **566**, 291-293 (2004).

153.   Delcorte, A., Bour, J., Aubriet, F., Muller, J. F. & Bertrand, P. *Sample metallization for performance improvement in desorption/ionization of kilodalton molecules: Quantitative evaluation, imaging secondary ion MS, and laser ablation*. Anal. Chem. **75**, 6875-6885 (2003).

154.   Keune, K. & Boon, J. J. *Enhancement of the static SIMS secondary ion yields of lipid moieties by ultrathin gold coating of aged oil paint surfaces*. Surf. Interface Anal. **36**, 1620-1628 (2004).

155.   Nguyen, T. C. et al. *A theoretical investigation of the yield-to-damage enhancement with polyatomic projectiles in organic SIMS*. J. Phys. Chem. B **104**, 8221-8228 (2000).

156.   Sjovall, P., Lausmaa, J. & Johansson, B. *Mass spectrometric imaging of lipids in brain tissue*. Anal. Chem. **76**, 4271-4278 (2004).

157.   Touboul, D. et al. *Tissue molecular ion imaging by gold cluster ion bombardment*. Anal. Chem. **76**, 1550-1559 (2004).

158. Todd, P. J., McMahon, J. M. & McCandlish, C. A. *Secondary ion images of the developing rat brain*. J. Am. Soc. Mass Spectr. **15**, 1116-1122 (2004).

159. Townes, J. A. et al. *Mechanism for increased yield with SF5+ projectiles in organic SIMS: The substrate effect*. J. Phys. Chem. A **103**, 4587-4589 (1999).

160. Takats, Z., Wiseman, J. M., Gologan, B. & Cooks, R. G. *Mass Spectrometry Sampling Under Ambient Conditions with Desorption Electrospray Ionization*. Science **306**, 471-473 (2004).

161. Cooks, R. G., Ouyang, Z., Takats, Z. & Wiseman, J. M. *Ambient Mass Spectrometry*. Science **311**, 1566-1570 (2006).

162. Chen, H. W., Talaty, N. N., Takats, Z. & Cooks, R. G. *Desorption electrospray ionization mass spectrometry for high-throughput analysis of pharmaceutical samples in the ambient environment*. Anal. Chem. **77**, 6915-6927 (2005).

163. Kauppila, T. J. et al. *New surfaces for desorption electrospray ionization mass spectrometry: porous silicon and ultra-thin layer chromatography plates*. Rapid Commun. Mass Spectrom. **20**, 2143-2150 (2006).

164. Cotte-Rodriguez, I., Takats, Z., Talaty, N., Chen, H. W. & Cooks, R. G. *Desorption electrospray ionization of explosives on surfaces: Sensitivity and selectivity enhancement by reactive desorption electrospray ionization*. Anal. Chem. **77**, 6755-6764 (2005).

165. Van Berkel, G. J., Ford, M. J. & Deibel, M. A. *Thin-layer chromatography and mass spectrometry coupled using desorption electrospray ionization*. Anal. Chem. **77**, 1207-1215 (2005).

166. Van Berkel, G. J. & Kertesz, V. *Automated sampling and imaging of analytes separated on thin-layer chromatography plates using desorption electrospray ionization mass spectrometry*. Anal. Chem. **78**, 4938-4944 (2006).

167. Takats, Z., Wiseman, J. M. & Cooks, R. G. *Ambient mass spectrometry using desorption electrospray ionization (DESI): instrumentation, mechanisms and applications in forensics, chemistry, and biology*. J. Mass Spectrom. **40**, 1261-1275 (2005).

168. Wiseman, J. M., Ifa, D. R., Song, Q. & Cooks, R. G. *Tissue Imaging at Atmospheric Pressure Using Desorption Electrospray Ionization (DESI) Mass Spectrometry*. Angew. Chem. **9999**, NA (2006).

169. Klerk, L. A., Broersen, A., Fletcher, I. W., van Liere, R. & Heeren, R. M. A. *Extended data analysis strategies for high resolution imaging MS: New methods to deal with extremely large image hyperspectral datasets*. Int. J. Mass Spectrom. **260**, 222-236 (2007).

170. Meglen, R. R. *Examining Large Databases - a Chemometric Approach Using Principal Component Analysis*. Mar. Chem. **39**, 217-237 (1992).

171. Mann, M., Hendrickson, R. C. & Pandey, A. *Analysis of proteins and proteomes by mass spectrometry*. Annu. Rev. Biochem. **70**, 437-473 (2001).

172. Schwartz, S. A., Reyzer, M. L. & Caprioli, R. M. *Direct tissue analysis using matrix-assisted laser desorption/ionization mass spectrometry: practical aspects of sample preparation*. J. Mass Spectrom. **38**, 699-708 (2003).

173. Norris, J. L., Porter, N. A. & Caprioli, R. M. *Combination Detergent/MALDI Matrix: Functional Cleavable Detergents for Mass Spectrometry*. Anal. Chem. **77**, 5036-5040 (2005).

174. Axelsson, J. et al. *Improved reproducibility and increased signal intensity in matrix-assisted laser desorption/ionization as a result of electrospray sample preparation*. Rapid Commun. Mass Spectrom. **11**, 209-213 (1997).

175. Garden, R. W. & Sweedler, J. V. *Heterogeneity within MALDI samples as revealed by mass spectrometric imaging*. Anal. Chem. **72**, 30-36 (2000).

176. Wang, Z. P., Russon, L., Li, L., Roser, D. C. & Long, S. R. *Investigation of spectral reproducibility in direct analysis of bacteria proteins by matrix-assisted laser desorption/ionization time-of-flight mass spectroscopy*. Rapid Commun. Mass Spectrom. **12**, 456-464 (1998).

177. Svensson, M., Skold, K., Svenningsson, P. & Andren, P. E. *Peptidomics-Based Discovery of Novel Neuropeptides*. J. Proteome Res. **2**, 213-219 (2003).

178. Broersen, A. & van Liere, R. *Feature Based Registration of Hyperspectral Data-Cubes*. Eurographics/ IEEE-VGTC Symposium on Visualization, 1-8, Lisbon, Portugal, (2006).

179. Broersen, A., van Liere, R. & Heeren, R. M. A. *Comparing three PCA-based methods for the 3d visualization of imaging spectroscopy data.* IASTED International Conference on Visualization, Imaging, & Image Processing, 540-545, Benidorm, Spain, (2005).

180. Mize, T. H. et al. *A modular data and control system to improve sensitivity, selectivity, speed of analysis, ease of use, and transient duration in an external source FTICR-MS*. Int. J. Mass Spectrom. **235**, 243-253 (2004).

181. Clerens, S., Ceuppens, R. & Arckens, L. *CreateTarget and Analyze This! new software assisting imaging mass spectrometry on Bruker Reflex IV and Ultraflex II instruments*. Rapid Commun. Mass Spectrom. **20**, 3061-3066 (2006).

182. Huster, D., Muller, P., Arnold, K. & Herrmann, A. *Dynamics of membrane penetration of the fluorescent 7-nitrobenz-2-oxa-1,3-diazol-*

4-yl (NBD) group attached to an acyl chain of phosphatidylcholine. Biophys J. **80**, 822-831 (2001).

183.   Kuerschner, L. et al. *Polyene-lipids: A new tool to image lipids*. Nature Methods **2**, 39-45 (2005).

184.   Maier, O., Oberle, V. & Hoekstra, D. *Fluorescent lipid probes: some properties and applications (a review)*. Chem. Phys. Lipids **116**, 3-18 (2002).

185.   Ishitsuka, R., Yamaji-Hasegawa, A., Makino, A., Hirabayashi, Y. & Kobayashi, T. *A lipid-specific toxin reveals heterogeneity of sphingomyelin-containing membranes*. Biophys J. **86**, 296-307 (2004).

186.   Kruse, R. & Sweedler, J. V. *Spatial profiling invertebrate ganglia using MALDI MS*. J. Am. Soc. Mass Spectr. **14**, 752-759 (2003).

187.   Adriaensen, L., Vangaever, F., Lenaerts, J. & Gijbels, R. *Matrix-enhanced secondary ion mass spectrometry: the influence of MALDI matrices on molecular ion yields of thin organic films*. Rapid Commun. Mass Spectrom. **19**, 1017-1024 (2005).

188.   Gilmore, I. S. & Seah, M. P. *Ion detection efficiency in SIMS: dependencies on energy, mass and composition for microchannel plates used in mass spectrometry*. Int. J. Mass Spectrom. **202**, 217-229 (2000).

189.   Benninghoven, A., Rüdenauer, F. G. & Werner, H. W. *Secondary ion mass spectrometry : basic concepts, instrumental aspects, applications, and trends* J. Wiley, New York, xxxv, 1227, 1987.

190.   Hensel, R. R., King, R. C. & Owens, K. G. *Electrospray sample preparation for improved quantitation in matrix-assisted laser desorption/ionization time-of-flight mass spectrometry*. Rapid Commun. Mass Spectrom. **11**, 1785-1793 (1997).

191.   Hanton, S. D., Cornelio Clark, P. A. & Owens, K. G. *Investigations of matrix-assisted laser desorption/ionization samplepreparation by time-of-flight secondary ion mass spectrometry*. J. Am. Soc. Mass Spectr. **10**, 104-111 (1999).

192.   Stoeckli, M. et al. *MALDI MSI of Compounds and Metabolites in Whole-body Tissue Sections*. 53rd ASMS Conference, San Antonio, (2005).

193.   Sjovall, P., Lausmaa, J., Nygren, H., Carlsson, L. & Malmberg, P. *Imaging of membrane lipids in single cells by imprint-imaging time-of-flight secondary ion mass spectrometry*. Anal. Chem. **75**, 3429-3434 (2003).

194.   Andrieu, N., Salvayre, R. & Levade, T. *Comparative study of the metabolic pools of sphingomyelin and phosphatidylcholine sensitive to tumor necrosis factor*. Eur. J. Biochem. **236**, 738-745 (1996).

195. Birbes, H., El Bawab, S., Hannun, Y. A. & Obeid, L. M. *Selective hydrolysis of a mitochondrial pool of sphingomyelin induces apoptosis*. Faseb J. **15**, 2669-2679 (2001).

196. Grassme, H. et al. *Host defense against Pseudomonas aeruginosa requires ceramide-rich membrane rafts*. Nature Med. **9**, 322-330 (2003).

197. Liu, P. S. & Anderson, R. G. W. *Compartmentalized Production of Ceramide at the Cell-Surface*. J. Biol. Chem. **270**, 27179-27185 (1995).

198. Tessier-Lavigne, M. & Goodman, C. S. *The Molecular Biology of Axon Guidance*. Science **274**, 1123-1133 (1996).

199. Dickson, B. J. *Molecular Mechanisms of Axon Guidance*. Science **298**, 1959-1964 (2002).

200. Kalil, K. & Dent, E. W. *Touch and go: guidance cues signal to the growth cone cytoskeleton*. Curr. Opin. Neurobiol. **15**, 521-526 (2005).

201. Wotjak, C. T. et al. *Release of Vasopressin within the Rat Paraventricular Nucleus in Response to Emotional Stress: A Novel Mechanism of Regulating Adrenocorticotropic Hormone Secretion?* J. Neurosci. **16**, 7725-7732 (1996).

202. Ludwig, M. *Dendritic release of vasopressin and oxytocin*. J. Neuroendocrinol. **10**, 881-895 (1998).

203. Hernando, F., Schoots, O., Lolait, S. J. & Burbach, J. P. H. *Immunohistochemical localization of the vasopressin V1b receptor in the rat brain and pituitary gland: Anatomical support for its involvement in the central effects of vasopressin*. Endocrinology **142**, 1659-1668 (2001).

204. Horobin, R. W. *Biological staining: mechanisms and theory*. Biotechnic & Histochemistry **77**, 3-13 (2002).

205. Andersson-Engels, S., Klinteberg af, C., Svanberg, K. & Svanberg, S. *In vivo fluorescence imaging for tissue diagnostics*. Phys. Med. Biol. **42**, 815-824 (1997).

206. Meyer, T. & Teruel, M. N. *Fluorescence imaging of signaling networks*. Trends Cell Biol. **13**, 101-106 (2003).

207. Stoeckli, M., Farmer, T. B. & Caprioli, R. M. *Automated mass spectrometry imaging with a matrix-assisted laser desorption ionization time-of-flight instrument*. J. Am. Soc. Mass Spectr. **10**, 67-71 (1999).

208. Puglielli, L., Tanzi, R. E. & Kovacs, D. M. *Alzheimer's disease: the cholesterol connection*. Nature Neurosci. **6**, 345-351 (2003).

209. Sostarecz, A. G. et al. *Influence of molecular environment on the analysis of phospholipids by time-of-flight secondary ion mass spectrometry*. Langmuir **20**, 4926-4932 (2004).

210. Chaurand, P. & Caprioli, R. M. *Direct profiling and imaging of peptides and proteins from mammalian cells and tissue sections by mass spectrometry*. Electrophoresis **23**, 3125-3135 (2002).

211. Yanagisawa, K. et al. *Proteomic patterns of tumour subsets in non-small-cell lung cancer*. Lancet **362**, 433-439 (2003).

212. Schwartz, S. A., Weil, R. J., Johnson, M. D., Toms, S. A. & Caprioli, R. M. *Protein profiling in brain tumors using mass spectrometry: Feasibility of a new technique for the analysis of protein expression*. Clin. Cancer Res. **10**, 981-987 (2004).

213. Geraerts, W. P., Smit, A. B., Li, K. W., Vreugdenhil, E. & van Heerikhuizen, H. in *Current aspects of the neurosciences* (ed. Osborne, N. N.) 255-305 (McMillan Press, London, 1991).

214. Schmidt, E. D. & Roubos, E. W. *Morphological basis for nonsynaptic communication within the central nervous system by exocytotic release of secretory material from the egg-laying stimulating neuroendocrine caudodorsal cells of Lymnaea stagnalis*. Neuroscience **20**, 247-257 (1987).

215. Smit, A., Jimenez, C., Dirks, R., Croll, R. & Geraerts, W. *Characterization of a cDNA clone encoding multiple copies of the neuropeptide APGWamide in the mollusk Lymnaea stagnalis*. J. Neurosci. **12**, 1709-1715 (1992).

216. Hook, V., Azaryan, A., Hwang, S. & Tezapsidis, N. *Proteases and the emerging role of protease inhibitors in prohormone processing*. FASEB J. **8**, 1269-1278 (1994).

217. Joosse, J. *Dorsal bodies and dorsal neurosecretory cells of the cerebral ganglia of Lymnaea stagnalis*. Archief voor Nederlandse Zoologie **16**, 1-103 (1964).

218. Simons, K. & Ikonen, E. *Cell biology - How cells handle cholesterol*. Science **290**, 1721-1726 (2000).

219. Liscum, L. & Munn, N. J. *Intracellular cholesterol transport*. Bba-Mol. Cell Biol. L. **1438**, 19-37 (1999).

220. Rukmini, R., Rawat, S. S., Biswas, S. C. & Chattopadhyay, A. *Cholesterol organization in membranes at low concentrations: Effects of curvature stress and membrane thickness*. Biophys J. **81**, 2122-2134 (2001).

221. Hsu, F. F. & Turk, J. *Structural determination of sphingomyelin by tandem mass spectrometry with electrospray ionization*. J. Am. Soc. Mass Spectr. **11**, 437-449 (2000).

222. Hsu, F. F. & Turk, J. *Electrospray ionization/tandem quadrupole mass spectrometric studies on phosphatidylcholines: The fragmentation processes*. J. Am. Soc. Mass Spectr. **14**, 352-363 (2003).

223. McMahon, J. M., Short, R. T., McCandlish, C. A., Brenna, J. T. & Todd, P. J. *Identification and mapping of phosphocholine in animal tissue by static secondary ion mass spectrometry and tandem mass spectrometry*. Rapid Commun. Mass Spectrom. **10**, 335-340 (1996).
224. Schriver, K. E., Chaurand, P. & Caprioli, R. M. 51st ASMS Conference, Montreal, (2003).
225. Ooi, G. T., Tawadros, N. & Escalona, R. M. *Pituitary cell lines and their endocrine applications*. Mol. Cell. Endocrinol. **228**, 1-21 (2004).
226. Young, J. I. et al. *Authentic cell-specific and developmentally regulated expression of pro-opiomelanocortin genomic fragments in hypothalamic and hindbrain neurons of transgenic mice*. J. Neurosci. **18**, 6631-6640 (1998).
227. Rudman, D., Hollins, B. M., Kutner, M. H., Moffitt, S. D. & Lynn, M. J. *Three types of alpha-melanocyte-stimulating hormone: bioactivities and half-lives*. Am. J. Physiol. Endocrinol. Metab. **245**, E47-54 (1983).
228. Arends, R. J. et al. *alpha-MSH acetylation in the pituitary gland of the sea bream (Sparus aurata L.) in response to different backgrounds, confinement and air exposure*. J. Endocrinol. **166**, 427-435 (2000).

Summary

One of the major challenges for scientists in the 21st century is to understand how different biomolecular species like RNA, DNA, hormones, lipids, carbohydrates, and proteins, work together to make living cells and organisms. This understanding will be crucial to improving health and the general quality of life. In order to do so, measurement tools are needed that are able to capture the dynamic and complex interplay between the different species. This interplay results in the appearance, interaction and disappearance of a manifold of molecular species on time scales ranging from seconds to hours to days. Capturing both spatial and temporal information of these ongoing processes will help in the quest to understanding their function in living cells and organisms.

Ideally, a single experiment would provide the chemical, spatial and temporal information of all species present in a living biological system. Furthermore, it would do so with high specificity and high lateral resolution. Currently, there is no single technique meeting all of these requirements. With optical microscopy one is able to examine molecular species in living systems with extremely high spatial resolution (down to 40 nm) and high sensitivity but the chemical specificity is obtained by different labeling strategies. Mass spectrometry on the other hand gives unique chemical specificity of the molecular species at a surface but the technique is limited in spatial resolution and to non-living systems.

In conventional tissue imaging approaches the localization of biomolecules is determined by the use of an antibody binding to an antigen, where the antibody is labeled with either a colorant or a fluorophore. The localization of the label is than imaged by optical microscopy. This need for labeling restricts the technique to imaging of specific, known, species. Furthermore, the presence of a label on the molecules of interest might affect the behavior and localization of these molecules. Another disadvantage of labeling is the difficulty in depicting small changes in the molecules of interest, like posttranslational modifications, which can be of crucial importance (e.g. the activation of neuropeptides). The required labels are not specific enough to distinguish between original and modified species. For these reasons there is a large interest in developing imaging

146

techniques with high chemical specificity. Imaging mass spectrometry (IMS) allows the investigation of both the identity and the localization of the molecular content directly from tissue sections, single cells and many other surfaces. As mentioned above the spatial resolution in conventional IMS is considerably less than in optical microscopy. Therefore, there is a need for both technical and methodological improvements to move the spatial resolution obtained in IMS in the direction of that of optical microscopy. To do so several new methods to IMS in combination with novel IMS instrumentation are described in this thesis, directed at obtaining high spatial resolution (cellular length scales) molecular images.

Chapter 1 introduces the biological systems under investigation and the specific questions asked. In this thesis different methods to study the molecular distributions in nervous tissue and single cells using IMS are described. The different model systems studied are the central nervous system of *Lymnaea stagnalis* (a freshwater snail), rat brain, rat, mouse and human pituitary and cultured neuroblastoma cells.

Lymnaea stagnalis has a central nervous system containing only ~20.000 neurons many of which are peptidergic and are of large size (50-150 μm). In rat brain tissue the interest lies primarily in the hypothalamic area, which is a region of the brain that controls an immense number of bodily functions. It is located in the middle of the base of the brain under the thalamus and links the nervous system to the endocrine system via the pituitary gland. The pituitary is a small organ at the base of the brain, part of the endocrine signaling system, which secretes hormones into the circulatory system. The action of the pituitary is regulated by signals coming from the hypothalamus.

In **chapter 2** the different ionization techniques used in IMS (secondary ion mass spectrometry (SIMS) and matrix-assisted laser desorption/ionization (MALDI)), the instrumentation and the different sample preparation techniques are discussed. In SIMS the sample surface is bombarded with high-energy primary ions. The impact of a high-energy primary ion on the solid surface results in desorption (or sputtering) of surface material. The primary ion beam is rastered over the sample surface, recording a mass spectrum at every point and the resulting image is constructed after the analysis. Since in SIMS the primary ion beam can be focused to very small dimensions, very high spatial resolution

ion images can be obtained, ~100 nm using a gallium primary ion beam. However, the sputtering process in SIMS induces a severe amount of damage to the molecular species present at the surface, such that (almost) no labile organic molecules can be observed intact. To prevent the extensive fragmentation in SIMS, different surface coating techniques can be used such as the deposition of a MALDI matrix (matrix-enhanced (ME) SIMS) or a metal (metal-assisted (MetA) SIMS). These surface coatings are directed at minimizing the internal energy deposition into the molecules, thus preventing extensive fragmentation.

MALDI-MS is known as a very soft ionization technique, well established in the analysis of macromolecular species like peptides, proteins, oligonucleotides and carbohydrates. In MALDI-MS, the analyte molecules are dissolved in a solution containing a suitable matrix. Evaporation of the solvent results in incorporation of the analyte molecules into the crystallizing matrix. The matrix crystals isolate the individual analyte molecules, exclude excess salt and mediate the incident laser energy by absorption. Next the sample is irradiated with typically a nitrogen laser operating at 337 nm or a frequency tripled Nd:YAG laser at 355 nm. In MALDI imaging experiments the dimensions of the ionization beam are much bigger than in SIMS. In typical MALDI experiments laser spot sizes are used ranging from 50 to 200 μm, severely hampering the obtainable spatial resolution. To overcome this shortcoming, MALDI imaging experiments can be conducted in the microscope mode where real time stigmatic ion images are taken. Here, an ion that leaves the sample at a particular location arrives at its conjugate image point on a 2D position sensitive detector. As a result, the spatial resolution is no longer dependent on the ionization beam but on the resolution of the ion optics and the detector.

Chapter 3 is a protocol describing the steps required to retrieve the molecular information from tissue sections using ME- and MetA-SIMS as well as MALDI-MS. These techniques require specific sample preparation steps directed at optimal signal intensity with minimal redistribution or modification of the sample analytes. In order to extract the relevant information from the huge datasets produced by IMS, new bioinformatics approaches have been developed.

Chapter 4 describes surface metallization by plasma coating to enhance desorption/ionization of membrane components such as lipids and sterols in

148

SIMS of tissues and cells. Using MetA-SIMS we obtained high-resolution images of the distribution of cholesterol and other membrane components on the surface of neuroblastoma cells. With this technique subcellular details could be distinguished (resolving power 1.5 μm). Alternatively, in ME-SIMS, 2,5-dihydroxybenzoic acid electrosprayed on neuroblastoma cells allowed intact molecular-ion imaging of phosphatidylcholine and sphingomyelin at the cellular level. In MALDI-IMS gold deposition on top of matrix-coated rat brain tissue sections strongly enhanced image quality and signal intensity. High-quality total ion count images were acquired and the neuropeptide vasopressin was localized in the rat brain tissue section at the hypothalamic area around the third ventricle.

Chapter 5 describes both MetA-SIMS and ME-SIMS experiments on *Lymnaea stagnalis* nervous tissue. It is shown that the tissue microenvironment has a great influence on the ionization efficiencies of different pseudomolecular ions of cholesterol, $[M-H]^+$, $[M-OH]^+$ and $[2M+Au]^+$ in MetA-SIMS experiments. The spatial distributions of these ions illustrate the influence of the biological matrix on the formation of specific pseudomolecular ions derived from the same molecular species.

Direct molecular imaging of nervous tissue at micrometer spatial resolution (<3 µm) is shown using ME-SIMS. Cryosections of the cerebral ganglia of *Lymnaea stagnalis* were placed on indium tin oxide coated conductive glass slides and covered with a thin layer of 2,5-dihydroxybenzoic acid, by electrospray deposition. High-resolution molecular ion maps of cholesterol and the neuropeptide APGWamide were constructed. APGWamide was predominantly localized in the cluster of neurons that regulate male copulation behavior of *Lymnaea*.

In **Chapter 6** neuropeptide distributions in rat, mouse and human pituitary tissue sections are obtained with MALDI-IMS. For the rat and human pituitary tissue sections the distributions of several neuropeptides are shown in the microprobe mode, overlain on the stigmatic total ion image. In the case of the mouse pituitary tissue section a stigmatic selected ion image was obtained. The distribution of the diacetylated neuropeptide α-MSH is shown in mouse pituitary with a pixel size of 500 nm and a resolving power of 4 µm, yielding superior spatial detail compared to images obtained in microprobe imaging experiments.

Summary

Since pituitary organs are small (10^2-10^3 µm) the spatial resolution of IMS is a key issue in molecular imaging of these tissue sections. Furthermore, we show that with imaging mass spectrometry a distinction can be made between different mammalian tissue sections based on differences in the amino acid sequence of neuropeptides with the same function.

Samenvatting

Een van de grootste uitdagingen voor wetenschappers in de 21ste eeuw is om te begrijpen hoe verschillende biomoleculaire componenten, zoals RNA, DNA, hormonen, lipiden, suikers en eiwitten, met elkaar samenwerken om levende cellen en organismen te maken. Deze kennis is cruciaal voor het verbeteren van onze gezondheid en kwaliteit van leven. Om dit voor elkaar te krijgen zijn meettechnieken nodig die het dynamische samenspel tussen deze verschillende componenten kunnen vastleggen. Dit samenspel resulteert in de vorming, interactie en het verdwijnen van een veelvoud aan moleculaire componenten op een tijdschaal variërend van seconden tot uren en dagen. Het vastleggen van zowel de spatiele als de temporale informatie van deze processen zal helpen in de zoektocht naar het begrijpen van hun functie in levende cellen en organismen.

In het optimale geval zou een enkel experiment zowel de chemische, spatiele als temporale informatie vastleggen van al de componenten aanwezig in een levend biologisch systeem. Bovendien zou deze techniek dit doen met hoge specificiteit en spatiele resolutie. Op dit moment is er niet een zo'n techniek die aan al deze voorwaarden voldoet. Met optische microscopie kan men moleculaire componenten in levende systemen onderzoeken met extreem hoge spatiele resolutie (tot 40 nm) en gevoeligheid maar de chemische specificiteit wordt verkregen door verschillende labeling strategieën. Aan de andere kan levert massa spectrometrie unieke chemische specificiteit voor de moleculaire componenten op een oppervlak maar deze techniek is gelimiteerd in de haalbare spatiele resolutie en tot niet-levende systemen.

In conventionele moleculaire plaatsbepalingen in weefsel wordt de moleculaire lokalisatie bepaald door de binding tussen een antibody en een antigen, waarbij het antibody gelabeld is met een fluorescerende of een kleurende groep. De lokalisatie van het label wordt vervolgens in beeld gebracht met behulp van optische microscopie. De noodzaak van het gebruik van een label beperkt de techniek tot specifieke, bekende, componenten. Bovendien kan de aanwezigheid van zo'n label aan het te onderzoeken molecuul het natuurlijke gedrag en de oorspronkelijke oriëntatie beïnvloeden. Een ander nadeel van het gebruik van

151

een label is de moeilijkheid in het bepalen van kleine veranderingen in de moleculen onder studie. Deze zogenaamde posttranslatie veranderingen kunnen cruciaal zijn in de activering van een molecuul (b.v. neuropeptiden). De benodigde labels zijn niet specifiek genoeg om een onderscheidt tussen het originele en het veranderde molecuul te maken. Om deze redenen is er grote belangstelling voor de ontwikkeling van plaatsbepaling technieken met hoge chemische specificiteit. Plaatsopgeloste massa spectrometrie faciliteert zowel het onderzoek naar de identiteit alsmede de lokalisatie van de moleculaire componenten, direct van weefsel, enkele cellen en vele andere oppervlakken. Zoals eerder genoemd is de spatiele resolutie in conventionele plaatsopgeloste massa spectrometrie veel minder hoog dan in optische microscopie. Hierdoor is er een noodzaak voor zowel technische als methodologische verbeteringen om de spatiele resolutie in de richting van die van optische microscopie te brengen. Om dit voor elkaar te krijgen worden er verschillende nieuwe methoden voor plaatsopgeloste massa spectrometrie in combinatie met nieuwe instrumentatie beschreven in dit proefschrift, gericht op het opnemen van hoge resolutie (cellulaire lengte schalen) plaatsopgeloste moleculaire verdelingen.

Hoofdstuk 1 introduceert de onderzochte biologische systemen en de specifieke vragen die gesteld zijn. In dit proefschrift worden verschillende methoden beschreven om de moleculaire verdeling in zenuwweefsel en enkele cellen te bestuderen met behulp van plaatsopgeloste massa spectrometrie. De verschillende modelsystemen zijn het centrale zenuwstelsel van *Lymnaea stagnalis* (een zoetwaterslak), rattenbrein, rat, muis en menselijk hypofyse en gekweekte neuroblastoma cellen.

Lymnaea stagnalis heeft een centraal zenuwstelsel wat bestaat uit slechts ~20.000 neuronen, waarvan er velen peptiden bevatten en groot van stuk zijn (50-150 μm). In rattenbrein weefsel ligt de interesse met name in het gebied van de hypothalamus, wat immens veel lichamelijke functies controleert. Dit gebied bevindt zich in het midden aan de basis van de hersenen onder de thalamus en verbindt het zenuwstelsel met het endocriene systeem via de hypofyse. De hypofyse is een klein orgaan die aan de basis van de hersenen ligt, is onderdeel van het endocriene signaal systeem en regelt de hormonale huishouding. De activiteit van de hypofyse wordt gereguleerd door signalen afkomstig van de hypothalamus.

In **hoofdstuk 2** worden de verschillende ionisatie technieken (secondaire ionen massa spectrometrie (SIMS) en matrix geassisteerde laser desorptie/ionisatie (MALDI)), de gebruikte instrumentatie en de verschillende vormen van monster voorbereiding beschreven die gebruikt worden in plaatsopgeloste massa spectrometrie. In SIMS wordt het monsteroppervlak bestookt met een hoog energetische bundel van primaire ionen. De inslag van zo'n hoog energetisch ion op het vaste oppervlak resulteert in de desorptie (of het sputteren) van oppervlakte materiaal. De primaire ionen bundel wordt over het oppervlak gerasterd en op ieder punt wordt een massa spectrum opgenomen. Van deze massa spectra wordt na de meting het bijbehorende beeld van het oppervlak geconstrueerd. Sinds in SIMS de primaire ionen bundel tot zeer kleine dimensies kan worden gefocusseerd is het mogelijk om ionen beelden met zeer hoge resolutie te verkrijgen, ~100 nm voor een gallium ionen bundel. Een nadeel van dit proces is dat een aanzienlijke hoeveelheid schade wordt veroorzaakt aan de moleculaire componenten aanwezig in het oppervlak, zo erg dat haast geen labiele organische moleculen intact kunnen worden waargenomen. Om deze fragmentatie tegen te gaan worden er verschillende oppervlakte modificatie technieken uitgevoerd zoals het toevoegen van een MALDI matrix (ME-SIMS) of een metaal (MetA-SIMS). Deze oppervlakte modificaties zijn gericht op het minimaliseren van de interne energie depositie in het molecuul om zodoende fragmentatie te voorkomen.

MALDI massa spectrometrie staat bekend als een zeer zachte vorm van ionisatie en is een algemeen gevestigde techniek in de analyse van macromoleculaire componenten zoals peptiden, eiwitten, oligonucleotiden, en suikers. In MALDI worden de te bepalen componenten opgelost in een oplossing die een geschikte matrix bevat. Het verdampen van deze oplossing resulteert in vorming van matrix kristallen waarin de te bepalen stoffen worden geïncorporeerd. De matrix kristallen isoleren de individuele stoffen, sluiten de overtollige zouten uit en absorberen het inkomende laserlicht. Vervolgens worden deze matrix kristallen belicht met een stikstof laser opererend op 337 nm of een frequentie verdrievoudigde Nd:YAG laser op 355 nm. In MALDI plaatsopgeloste massa spectrometrie zijn de dimensies van de ionisatie bundel vele malen groter dan die in SIMS. In standaard MALDI experimenten wordt een laser bundel van 50 tot 200 μm gebruikt, wat de haalbare spatiele resolutie erg limiteert. Om deze

tekortkoming te overkomen kunnen plaatsopgeloste massa spectrometrie experimenten worden uitgevoerd in de microscoop modus, waarbij stigmatische ionen beelden direct worden opgenomen. Hier wordt een ion dat het oppervlak op een bepaalde locatie verlaat, gedetecteerd op zijn geconjugeerde positie op een 2D plaatsgevoelige detector. Het resultaat van dit principe is dat de spatiele resolutie niet langer afhankelijk is van de resolutie van de ionenbundel maar enkel van de resolutie van de ionen optica en de detector.

Hoofdstuk 3 is een protocol waarin de verschillende stappen staan beschreven die genomen moeten worden om moleculaire informatie uit weefsel secties te verkrijgen bij analyse met ME- en MetA-SIMS en MALDI plaatsopgeloste massa spectrometrie. Deze technieken vereisen specifieke monstervoorbewerking gericht op optimale signaal intensiteit met minimale verplaatsing of modificaties van de componenten in het monster. Om vervolgens de relevant informatie uit de enorme datasets die gecreëerd worden te extraheren zijn nieuwe informatica toepassingen ontwikkeld.

Hoofdstuk 4 beschrijft oppervlakte metallisatie, door middel van plasma coaten, in SIMS analyse van weefsel en cellen, met als doel het verhogen van de desorptie/ionisatie van membraan componenten zoals lipiden en sterolen. Gebruikmakend van MetA-SIMS hebben we hoge resolutie beelden van de verdeling van cholesterol en andere membraan componenten op het oppervlak van neuroblastoma cellen opgenomen. Met deze techniek konden subcellulaire details worden waargenomen (oplossend vermogen 1.5 μm). Als alternatief hebben we met behulp van electrospray 2,5-dihydroxybenzoëzuur gedeponeerd op neuroblastoma cel oppervlakken. ME-SIMS experimenten konden hier de plaats bepalen van de intacte moleculaire ionen van phosphatidylcholine en sphingomyelin op cellulair niveau. In MALDI versterkte de depositie van een laag goud op met matrix bedekt rattenbrein weefsel zowel de beeldkwaliteit als de signaalintensiteit. Een beeld met zeer hoge kwaliteit van al de ionen werd opgenomen en de lokalisatie van het neuropeptide vasopressine werd in kaart gebracht in het hypothalamus gebied van het weefsel rond het derde ventrikel.

Hoofdstuk 5 beschrijft zowel MetA-SIMS als ME-SIMS experimenten op *Lymnaea stagnalis* zenuwweefsel. Hier wordt aangetoond dat de micro-omgeving binnen het weefsel van grote invloed is op de ionisatie efficiëntie van verschillende pseudo-moleculaire ionen van cholesterol, $[M-H]^+$, $[M-OH]^+$ en

[2M+Au]$^+$, in MetA-SIMS experimenten. De spatiele distributie van deze ionen illustreert de invloed van de biologische matrix bij het formeren van specifieke pseudo-moleculaire ionen afkomstig van een enkel moleculair component.

Directe moleculaire plaatsbepaling in zenuwweefsel op micrometer lengteschaal spatiele resolutie (<3 μm) is uitgevoerd met behulp van ME-SIMS. Weefsel secties van de cerebrale ganglion van *Lymnaea stagnalis* zijn op indium tin oxide gecoat glas geplaatst en bedekt met een dunne laag 2,5-dihydroxybenzoëzuur, met behulp van electrospray depositie. Hoge resolutie moleculaire ion kaarten van cholesterol en het neuropeptide APGWamide zijn geconstrueerd. APGWamide was voornamelijk gelokaliseerd in de neuronencluster welke verantwoordelijk is voor de regulering van het voortplantingsgedrag van *Lymnaea*.

In **hoofdstuk 6** zijn neuropeptiden distributies verkregen in rat, muis en menselijk hypofyse weefsel met plaatsopgeloste massa spectrometrie. In rat en menselijk hypofyse weefsel zijn de distributies van verschillende neuropeptiden in beeld gebracht in de microprobe modus en getoond boven op het stigmatische beeld van al de ionen. In het geval van de muis hypofyse is een stigmatisch geselecteerd ion beeld opgenomen. De verdeling van het dubbel geacetyleerde neuropeptide α-MSH is weergegeven in muis hypofyse met een pixel grootte van 500 nm en een oplossend vermogen van 4 μm. Dit geeft superieur spatieel detail in vergelijking tot microprobe plaatsbepalingen. Aangezien hypofyse weefsel zeer klein is (10^2-10^3 μm) is de spatiele resolutie van zeer groot belang in de moleculaire analyse. Verder laten we zien dat met behulp van plaats opgeloste massa spectrometrie een onderscheidt gemaakt kan worden tussen verschillende weefsel van verschillende zoogdieren op basis van verschillen in de aminozuursequentie van neuropeptiden met dezelfde biologische functie.

Nawoord

En dan eindelijk het dankwoord en ik moet zeggen het voelt heel goed om dit nu te kunnen schrijven. Dit proefschrift is mede tot stand gekomen dankzij de hulp van vele personen en op deze plaats wil ik hen die in meer of mindere mate een bijdrage hebben geleverd hartelijk bedanken.

In het bijzonder wil ik mijn begeleiders Sander en Ron bedanken bij wie ik altijd zo kon binnen lopen met vragen of ideeën. Sander, ik was de eerste en enige student in jouw groep en had dus nooit te klagen over de hoeveelheid begeleiding. Jij liet mij vrij in de keuzes voor mijn onderzoek en dit heb ik altijd zeer gewaardeerd. Jouw kritische blik en de altijd gevraagde extra bewijsvoering hebben zeker bijgedragen aan de totstandkoming van dit proefschrift. Ron jouw groot enthousiasme, scherpe interpretatie en niet aflatende stroom nieuwe ideeën hebben mij enorm gestimuleerd. Zeker in het laatste deel van de promotie, na de verhuizing van Sander, heeft mij dit zeer geholpen.

Voor het uitvoeren van al de experimenten beschreven in dit proefschrift ben ik veel dank verschuldigd aan de personen die altijd bereid waren cellen te kweken of weefsels te snijden en die mij geholpen hebben met de biologische interpretatie van de data. Bij deze wil ik dan ook Wolter Mooi, en Angelique Verlaan van het VUmc, Jan van Minnen, Zineb el Filali en Connie Jimenez van de VU, Peter Verhaert van de TU Delft, Roger Adan, Bo de Lange en Linda Verhagen van het UMC en Kees Jalink, Bas Ponsioen en Michiel Langeslag van het NKI hartelijk danken.

Aan mijn collega's in het imaging project, Stefan en Liam ben ik zeer veel dank verschuldigd voor het ontwikkelen alsmede het in top conditie houden van de instrumentatie. Zonder hen had ik waarschijnlijk nooit de resultaten geboekt zoals die nu in dit proefschrift staan beschreven, dank.

Ivo, waar zouden al de enen en nullen die ik heb gemeten toe hebben geleidt als jij er niet was geweest om al die mooie software tools te schrijven. Ik heb het samenwerken met jou als heel prettig ervaren. Je stond altijd open voor nieuwe ideeën en voor extra tooltjes of buttons die aan de geschreven software toegevoegd moesten worden. Je was ook altijd bereid even een snelle houtje-

touwtje versie te ontwikkelen als ik bedacht dat er weer eens haast geboden was.

Verder wil ik iedereen van AMOLF in de technische, logistieke en algehele ondersteuning bedanken. Als eerste is daar Frans Giskens, Frans bedankt voor al de hulp bij zowel de kleinere klusjes als met het ontwikkelen van de SprayStation2. Van jouw netheid en precisie kan ik nog steeds een hoop leren. Mark en Jerre bedankt voor al de assistentie door de jaren heen. Dirk-Jan Spaanderman en Iliya Cerjak, voor de mooie ontwerpen en de assistentie bij het (weer eens op het laatste moment) printen van de posters. De werkplaats voor het vervaardigen van menig onderdeel en Wim Barsingerhorn voor het snijden van de ITO glazen. Marco Konijnenburg voor de software ondersteuning en, samen met Lars, voor de assistentie met al de data transfer en massstore communicatie perikelen. Duncan voor de hulp bij de ontwikkeling van de SprayStation2 en Hans Alberda voor de ontwikkeling van labview software voor de eerste SprayStation.

Daarnaast wil ik Lennaert Klerk en Alexander Broersen bedanken voor de assistentie met de PCA analyse, Denitza Lambreva voor de AFM metingen en Mirjam Damen voor de assistentie bij het meten op de MALDI ToF-ToF.

En dan nog een hele hoop mensen gewoon voor de gezelligheid, met name al mijn directe collega's van de massa spectrometrie groep. Ioana jouw wil ik speciaal bedanken omdat je er, vooral in de laatste fase van de promotie, veel voor me was. Natuurlijk Rimco, mijn kamergenoot voor het grootste gedeelte van mijn verblijf op AMOLF, het was me een waar genoegen! En verder: Todd, Katrien, Yuri, Frans, Jerre, Martin, Marc, Gert, Erika, Andreas, Ester, Romulus, Liam, Anne, Lennaert, Frank, Xinghua, Piet, Georgiana, Jaap van der Weerd, Beatrice, Annelies, Jaap Boon, Jerre, Lidwien, Bas, Olga, Aleksey, Başak, Els en Luke voor de gezelligheid tijdens de thee/koffie pauzes, lunch, borrels en kroeg/disco bezoeken.

Mijn familie en vrienden en met name Marloes wil ik bedanken voor de steun tijdens en interesse in mijn onderzoek.

<div align="right">Maarten Altelaar 07 februari 2007</div>

Curriculum Vitae

Maarten Altelaar werd geboren op 21 maart 1976 te Alkmaar. Tijdens zijn studie chemie aan de Hogeschool Alkmaar begon hij in 1998 aan de studie scheikunde aan de Vrije Universiteit Amsterdam. Tijdens deze studie werd een afstudeerstage naar enzym versterkte biochemische detectie alsmede een stage in Tarragona, Spanje naar de bepaling van polycyclische aromatische koolwaterstoffen in zeewater en sediment verricht. In juli 2002 werd het doctoraal examen behaald. In mei 2002 begon hij als onderzoeker in opleiding bij het FOM instituut voor atoom en molecuul fysica (AMOLF) onder begeleiding van Dr. Sander R. Piersma en Prof. dr. Ron M.A. Heeren. Het onderwerp van het promotieonderzoek was het in kaart brengen van biomoleculaire verdelingen in cellen en weefsel secties, en heeft geresulteerd in dit proefschrift. De onderzoeksresultaten zijn onder meer gepresenteerd tijdens lezingen op de jaarlijkse bijeenkomst van de American Society for Mass Spectrometry in Nashville (2004) en San Antonio (2005), op de 15th International Conference on Secondary Ion Mass Spectrometry (SIMS XV) in Manchester (2005) en op de

This thesis is based on the following publications

A. F. Maarten Altelaar, Stefan L. Luxembourg, Liam A. McDonnell, Sander R. Piersma and Ron M.A. Heeren, *Imaging Mass Spectrometry at Cellular Length Scale Spatial Resolution.* Nature Protocols, Accepted (**Chapter 3**)

A. F. Maarten Altelaar, Ivo Klinkert, Kees Jalink, Robert P. J. de Lange, Roger A. H. Adan, Ron M. A. Heeren, and Sander R. Piersma, *Gold-Enhanced Biomolecular Surface Imaging of Cells and Tissue by SIMS and MALDI Mass Spectrometry.* Analytical Chemistry, 2006, 78(3), 734-742. (**Chapter 4**)

A. F. Maarten Altelaar, Jan van Minnen, Connie R. Jiménez, Ron M. A. Heeren, and Sander R. Piersma, *Direct molecular Imaging of Lymnaea stagnalis nervous tissue at subcellular spatial resolution by mass spectrometry.* Analytical Chemistry, (accelerated article), 2005, 77(3), 735-741. (**Chapter 5**)

A.F. Maarten Altelaar, Jan van Minnen, Ron M.A. Heeren, Sander R. Piersma, *The influence of the cholesterol microenvironment in tissue sections on molecular ionization efficiencies and distributions in ToF-SIMS.* Applied Surface Science, 2006, 252(19), 6702-6705. (**Chapter 5**)

A. F. Maarten Altelaar, Ioana M. Taban, Liam A. McDonnell, Peter D. E. M. Verhaert, Robert P. J. de Lange, Roger A. H. Adan, Wolter j. Mooi, Ron M. A. Heeren, and Sander R. Piersma, *High-Resolution MALDI Imaging Mass Spectrometry allows Localization of Peptide Distributions at Cellular Length Scales in Pituitary Tissue Sections.* International Journal of Mass Spectrometry, 2007, 260(2-3), 203-211. (**Chapter 6**)

Other Publications

Ioana M Taban; A.F. Maarten Altelaar; Jens Fuchser; Yuri E. M van der Burgt; Liam A. McDonnell; Goekhan Baykut; Ron M. A. Heeren, *Imaging of peptides in the rat brain using MALDI-FTICR mass spectrometry.* Journal of the American Society for Mass Spectrometry, 18(1), 2007, 145-151.

Stefan Luxembourg, Maarten Altelaar, Liam McDonnell en Ron Heeren, *Massamicroscopie: moleculaire foto's van eiwitverdelingen.* Nederlands Tijdschrift voor Natuurkunde, 2006, 72-6, 188-192.

R.M.A. Heeren, L.A. McDonnell, E. Amstalden, S.L. Luxembourg, A.F.M. Altelaar, S.R. Piersma, *Why don't biologists use SIMS?: A critical evaluation of imaging MS.* Applied Surface Science, 2006, 252(19), 6827-6835.

Liam A. McDonnell, Sander R. Piersma, A. F. Maarten Altelaar, Todd H. Mize, Stefan L. Luxembourg, Peter D. E. M. Verhaert, Jan van Minnen, Ron M. A. Heeren, *Subcellular imaging mass spectrometry of brain tissue.* Journal of Mass Spectrometry, 2005, 40(2), 160-168.

Gimeno, R.A., Altelaar A.F.M., Marce, R.M. and Borrull, F., *Determination of polycyclic aromatic hydrocarbons and polycyclic aromatic sulfur heterocycles by high-performance liquid chromatography with fluorescence and atmospheric pressure chemical ionization mass spectrometry detection in seawater and sediment samples.* Journal of Chromatography A, 2002, 958(1-2): p. 141-148.

Reza M. Seifar, Maarten A. F. Altelaar, Reyer J. Dijkstra, Freek Ariese, Udo A. Th. Brinkman, and Cees Gooijer, *Surface-enhanced resonance Raman spectroscopy as an identification tool in column liquid chromatography.* Analytical Chemistry, 2000, 72(22): p. 5718-5724.